Flexible Photonics with High Contrast Metastructures

Li Zhu

Electrical Engineering and Computer Sciences
University of California at Berkeley

May 1, 2016

Acknowledgement

Flexible Photonics with High Contrast Metastructures

by

Li Zhu

A dissertation submitted in partial satisfaction of the

requirements for the degree of

Doctor of Philosophy

in

Engineering – Electrical Engineering and Computer Sciences

and the Designated Emphasis

in

Nanoscale Science and Engineering

in the

Graduate Division

of the

University of California, Berkeley

Committee in charge:

Professor Constance J. Chang-Hasnain, Chair
Professor Ming C. Wu
Professor Xiang Zhang

Fall 2015

Flexible Photonics with High Contrast Metastructures

Abstract

Flexible Photonics with High Contrast Metastructures

by

Li Zhu

Doctor of Philosophy in Engineering – Electrical Engineering and Computer Sciences

and the Designated Emphasis in Nanoscale Science and Engineering

University of California, Berkeley

Professor Constance J. Chang-Hasnain, Chair

Light manipulation on a flexible, conformable, wearable surface with functions of light emission, detection and processing is the next frontier for many applications, including ubiquitous environment-awareness sensors for bridge, buildings, airplanes and robots; wearable health monitoring devices for public health; active camouflage; wearable displays and visual arts for commercial products; systems on a foil. However, the rigidness of the conventional photonic devices and systems limits their use in the flexible photonics application.

Despite the efforts that facilitate the flexible devices based on the organic materials, the performance of the devices are still compromised comparing with the devices made of the semiconductors. The transfer printing method provides an alternative paradigm in implementing the flexible photonic devices, by transferring the devices made of semiconductors on to the flexible substrates. However, many new challenges are arisen to incorporate the conventional photonic devices in the flexible platform, including thermal management, optical interconnect, etc.

The high contrast metastructure (HCM) is an emerging element for photonics, with its unique capability to achieve the light wave engineering in the sub-wavelength scale. It has abundant properties and design versatility. The HCM can be designed to be an ultra-thin broadband high reflectivity mirror, replacing the conventional DBR reflector with a superior performance. It can also be configured as a mirrorless resonator to achieve high quality factor resonance with convenient free space coupling.

This dissertation is devoted to explore the physics of the HCM in the near-wavelength regime, especially for its unique property in diffraction order enhancement and coupling. We present the new optical phenomena in the dual order diffraction regime and utilize this anomalous diffraction for making the first artificial chameleon skin. We also leverage on the ultra-thin thickness of the HCM reflector to significantly improve the thermal conductance for a heterogeneously integrated vertical cavity surface emitting laser (VCSEL). Through this effort, we demonstrate the first flexible VCSEL operating at the silicon transparent wavelength. Based on the HCM and external photonic structure coupling, we also demonstrate a variety devices for the efficient photonic integration on the flexible platform.

1

To Cecilia, my beloved wife,

whose devotion to our family

made it possible for me to complete this work,

and to our beautiful daughters, Ariel and Allie,

who keep me positive through challenges.

Table of Contents

List of Figures

Acknowledgements

Foremost, I would like to express my sincere gratitude to my advisor, Professor Connie Chang-Hasnain, for her guidance and mentorship through my Ph.D study. Her motivation, enthusiasm, dedication and knowledge not only help me to find solutions to the challenges in the research work, but also guide me to build the philosophy and methodology to start the career. I am very grateful for the opportunities she has brought to me.

I also thank Professor Ming Wu, Professor Eli Yablonovitch and Prof. Xiang Zhang for their guidance in my graduation work, and the review on this dissertation and serving on my qualifying exam committee. Your inputs helped strengthen my research and helped me to see the insight on the work from a different perspective.

None of this would be possible without working with a group of remarkable researchers. I thank Vadim Karagodsky for his mentorship started even before I joined Berkeley. I also thank Dr. Chris Chase, Dr. Roger Chen, Dr. Thai Tran, Dr. Wai Son Ko, Dr. Billy Ng for their wisdom and spirit shared with me in research and life. I am particularly grateful to Dr. James Ferrara, Dr. Weijian Yang and Dr. Yi Rao. The work would not be possible without their contribution. I sincerely cherish the time we enjoyed the accomplishments and fought through the difficult times. I also thank Dr. Fanglu Lu, Tianbo Sun and Kun Li for accompanying me through my Ph.D career. I also appreciate the collaboration with Dr. Michael Qiao, Adair Gerke, Indrasen Bhattacharya, Jonas Kapraun and Peter Phan. I am really grateful to have the collaboration with Prof. Ming Wu's group and Prof. Gerald Marriott's group. I would like to thank Sangyoon Han, Phillip Sandborn, Dr Niels Quack and Dr. Tae Joon Seok for the collaboration in EPHI project. I also thank Dr. Shu Kan for the collaboration in the bio-imaging project. I am grateful to Therese George for her numerous help during my study in Berkeley. Finally, I thank all the optoelectronics student for the wonderful research environment and sharing the same passion in the research.

I thank the Berkeley Marvell nanolab staffs for their support in the device fabrication.

I am also thankful to the financial supports from DARPA EPHI project, NSSEFF, CIAN and NSF.

Chapter 1

Introduction

1.1 Introduction to Flexible Photonics

Photonics technology provides the generation, control and detection of the light waves and photons. It is one of the major driving horse for the innovations of today's science and technology, as well as the growth of the world economy [1]. The global photonics market volume is predicted to reach 615 billion us dollars by year 2020, with the growth trend shown in Figure 1.1. In the past decades, a variety of well-known photonics devices, such as lasers, solar cells, displays and optical sensors, enable the technological revolutions for communication, energy harvesting, commercial electronics, manufacturing and imaging. An explicit breakdown of the market segment is shown in Figure 1.2.

Taking advantage of the micro and nano-fabrication technology, the photonic devices, including diode laser, amplifier, photodetector, modulator, waveguide, etc., are miniaturized into micro scale, where people can build powerful and omni-functional photonic systems into the small chips. The photonic integrated circuits (PICs) are crucial in optical communication, providing tremendous increment of communication bandwidth comparing with the electrical cables [2]. It is the backbone to support the astronomical data generation in today's internet, with keeping the promise of reducing the cost and energy consumption. Working with the microfluidics technologies, PICs generate great potential in biological applications by providing high sensitivity compact micro-photonic sensors [3]. A recent breakthrough further points the way to use the PICs for photonic quantum computing, that can revolutionize the paradigm of computing [4].
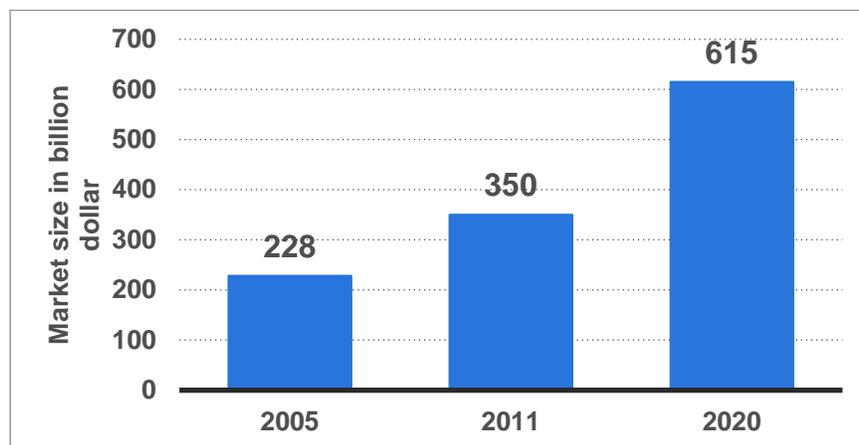
Figure 1.1 The global photonics market volume in year 2005, 2011 and the projection in 2020 [5].
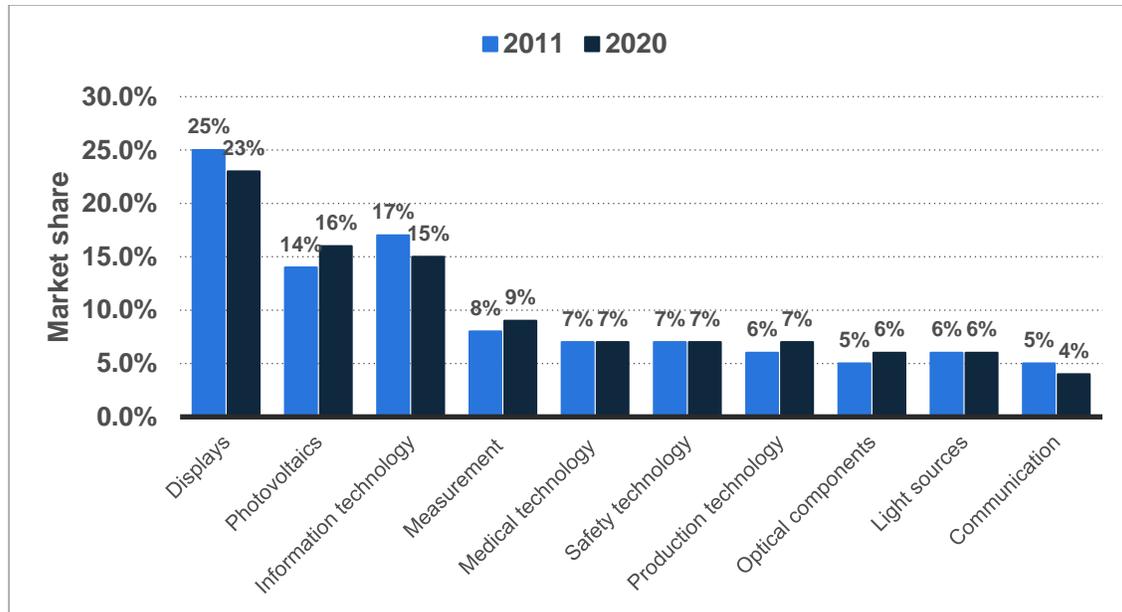
Figure 1.2 Breakdown of the global photonics market in the year of 2011 and 2020 [6].

Light manipulation on a flexible, conformable, wearable surface with functions of light emission, detection and processing is the next frontier for many applications, including ubiquitous environment-awareness sensors for bridge, buildings, airplanes and robots; wearable health monitoring devices for public health; active camouflage; wearable displays and visual arts for commercial products; systems on a foil. However, the rigidness of the conventional photonic devices and systems limits their use in the flexible photonics application.

In the past decade, the research on the flexible photonic and electronic devices is emerging. The flexible thin film transistors [7] and the organic light emitting diodes [8] have been commercialized, empowering the flexible organic light emitting diode (OLED) displays [9]. Organic solar cells [10] have been drastically improved [11-13] towards the market entry, providing low cost and clean power generation on any arbitrary surface. Despite of those efforts that facilitate the flexible devices based on the soft materials, the performance of the devices are still compromised comparing with the devices made of the high quality semiconductors.

In addition to reinventing the photonic devices with organic materials, an alternative paradigm in implementing the flexible photonic devices is to physically transfer the devices made of high quality semiconductors on to the flexible substrates [14]. This transfer printing method has demonstrated the flexible photonic devices that emit, absorb and transport light, ranging from solar cells to LEDs and photo detectors, to have comparable performance to the ones on the rigid substrates [15].

1.2 Challenges towards Being Flexible

To further explore the functional flexible photonic systems, there are still more challenges to be conquered. Lasers are the heart for the photonic system. Recently, the GaAs-based vertical cavity surface emitting laser (VCSEL) at 850 nm wavelength is demonstrated on polymer substrate [16, 17]. Nevertheless, in order to take advantage of silicon photonics technology, which is proven to have promising performance on the flexible substrates by the transfer printing method [18], a flexible laser at silicon transparent wavelength is desired. The VCSELs at telecommunication wavelength inevitably require InP-based material system. Such a material system gives smaller refractive indices variation Δn for the Bragg reflector, leading to thicker DBR mirrors and worse thermal conductivity [19]. In addition, the InP-based material is lack of current confinement method which is relatively easy to achieve in GaAs-based materials system; and the p-type InP usually has higher free carrier absorption and high resistivity. All those problems need to be addressed to provide the laser on the flexible substrates.

Comparing with the electrical circuits, the photonic integrated circuits are more sensitive to the temperature, especially when the engineering in the wavelength domain is involved. The operation of the currently photonic circuits typically requires constant temperature controlling. On the other hand, the flexible substrates are usually bad thermal conductors. To give an intuitive picture, a commonly used polymer called polydimethylsiloxane (PMDS) has thermal conductivity ~1000 times lower than semiconductors. Moreover, the nature of the flexible photonic application needs the device to work on the surfaces like human skin, wall, glass, etc. The ambient environment provides additional heating instead of cooling. All of those factors make the thermal optimization extremely critical for the success of the flexible photonic devices.

The light connection in the conformable photonic system is a new subject. Unlike electrical circuits which only require physical connection of the conductive wires, the light coupling between the system elements requires the mode matching, which involves the distance, orientation and alignment of the components. For rigid systems, those factors are fixed and reliable connection can be achieved. However, the layout of the flexible system becomes a variable under the conformable prerequisite. Therefore, the light coupling mechanism with large tolerance needs to be developed.

Additionally, the flexible or wearable applications require new functionalities beyond the capabilities of the replicated photonics components from the rigid substrates. For instance, the device provides simple stress indication, such as visible color or brightness change, is desired to reveal the level of the deformation. For the macro-scale flexible photonic devices aiming to be wrapped on any arbitrary surface, aesthetics is an important consideration for the device design which is overlooked by the conventional device design. As an illustration, any surface under illumination can be converted for power generation. However, all of the existing solar cells are in dark grey color which is not friendly in landscape design. Thus, the solar cells have the color configurability while maintaining high efficiency is extremely important for omnipresent photovoltaics.

1.3 Opportunities from Near-Wavelength Engineering

Recently, the high contrast metastructure (HCM) has emerged as a new platform with many designable, extraordinary optical properties [20]. HCM is a periodic structure made of one single-layer, high refractive-index material fully surrounded by a low index media. The conventional periodic structure is modeled as diffraction gratings, being a fundamental building blocks in optics. They are well understood in two regimes: the diffraction regime, where the period is much greater than the wavelength, and the deep-subwavelength region, where the period is much less than the wavelength.

However, there exists a third regime between those two well-known regions: the near-wavelength regime, in which the period is very close to the wavelength of interest. A single-layer ultra-thin HCM can serve as broadband high reflectivity mirror, demonstrating reflectivity >98.5% over a wavelength span of $\frac{\Delta\lambda}{\lambda} > 35\%$ [21]. This mirror is subsequently incorporated as the mirror in the VCSELs emitting at 850 nm, 980 nm, 1330 nm and 1550 nm wavelength regimes, replacing the conventional distributed Bragg reflector (DBR) mirror with superior performance and 20 to 50 times thinner thickness [22-27]. By incorporating the microelectromechanical structures (MEMS), the HCM mirror is actuated to tune cavity resonance for the tunable lasers and tunable phase arrays [23, 28-30].

Besides being an excellent mirror, HCMs can be designed to form a mirrorless cavity with a quality factor (Q factor) as high as 10^7 [31]. It is demonstrated as a laser with adding the gain into the cavity structure [32]. It also provides easy space light coupling due to its large area size, which is promising for low cost sensing [33]. In addition, the sub-wavelength feature size provides the approach for wave-front shaping of the light beam. It leads to the planar phase engineering such as planar lens [34, 35] and vortex beam phase plate [36], without suffering from the high loss through the metallic nano-antenna approach [37],.

The aforementioned explorations in the theoretical analysis and experimental implementations have proved the great potential of the HCM structure to replace the conventional optics elements with superior performance or novel functionalities. Given the fact that the thickness of the HCMs is typically a fraction of the wavelength of interest, semiconductors become extremely flexible despite of their rigid nature. Realizing the HCM based photonic devices with sub-wavelength geometrics on the flexible substrate can make the PICs readily for the flexible applications.

1.4 Dissertation Overview

This dissertation focuses on exploring the new optical phenomena from the HCM and applying them for the flexible photonics applications. The fundamental physics of the HCM is covered in Chapter 2. The basic analytical formation based on the matrix Fabry-perot approach is first introduced, as well as the unique properties of the HCM, such as ultra-broadband high reflection and high Q-factor resonance. The theory is further extended from the subwavelength regime to the dual diffraction order regime, where only two diffraction orders (0th and -1st) are allowed. We show the HCM can be designed to enhance any of the order while annihilating the rest of them. Such a

unique property leads to the anomalous reflection and refraction at the metastructure surface, where the output light follows an anomalous angle in contrast to the Snell's law. We also investigate how the finite aperture size makes the HCM property deviate from the analytical results based on the infinite size HCM assumption. In addition, we also discover the strong coupling between the HCM resonance and the waveguide resonance by placing a thin high index layer very close to the HCM. Such an effect creates strong field enhancement in the external layer, which makes the HCM an excellent waveguide coupler as well as a novel field concentrator. Chapter 3 reports the work on using the HCM on the flexible substrate to realize a color-tunable material whose color can be controlled with the deformation. This is the first demonstration of the artificial chameleon skin. The applications of such a novel material on display and camouflage applications are also explored. Chapter 4 shows the first flexible VCSEL operating at the silicon transparent wavelength. It is based on the heterogeneous integration of InP epitaxial layers on a silicon HCM with flip chip bonding technique. Thermal management is performed to improve the heat conductance of the VCSEL to achieve room temperature continuous wave operation. Chapter 5 reports a set of devices based on the HCM for photonic integration, such as vertical optical coupler, optical multiplexer, integrated optical switch. Those components can work together with the flexible VCSEL to build a photonic integrated system in the flexible substrate. Chapter 6 summaries the dissertation and discuss the outlook and future work for the further development of the HCM for flexible photonics.

Chapter 2

Physics of High Contrast Metastructure

2.1 Matrix Fabry-Perot Approach

As briefly introduced in Chapter 1, a high contrast metastructures (HCM) consists a single layer of periodic structure whose period is close to the wavelength of interest. It is made of materials persisting high refractive indices and being embedded in a low index medium. An HCM with one-dimensional periodicity is illustrated in Figure 2.1. It consists high index bars (n_{bar}) periodically spaced in the x-direction. The length of the bar in the y-direction is considered to be infinite. The optical properties of the HCM is dictated by three geometric parameters, including period (Λ), thickness (t_g) and duty cycle (η), which is defined as the ratio of the bar width (s) over the period. For planar phase engineering or polarization independent optics applications, the additional periodicity can be added to the y-direction to achieve a two-dimensional metastructure, as shown in Figure 2.2.
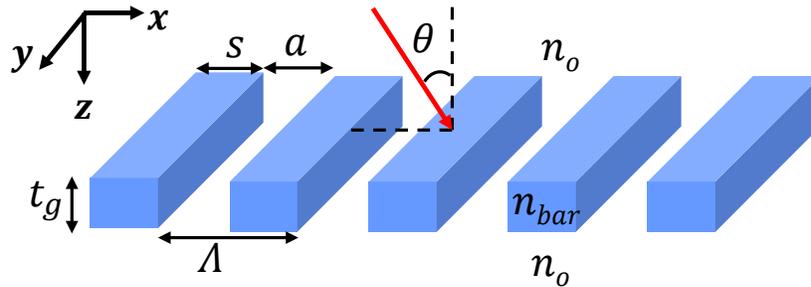
Figure 2.1 Schematic of one-dimensional HCM. The structure geometry denotations are defined as: Λ, period; s, high index bar width; a, low index gap width; t_g, HCM thickness; θ, incidence angle respect to surface normal direction. The duty cycle is defined as $\eta = \frac{a}{s}$.
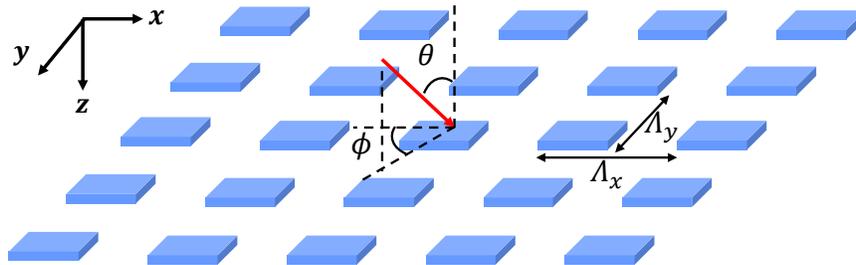
Figure 2.2 Schematic of two-dimensional HCM. It has periodicity in both x and y direction. It can be designed to shape the wave front with the dependence on both

x and y coordinates. For the polarization independent applications, $\Lambda_x=\Lambda_y$ and $\eta_x = \eta_y$

To illustrate the inherent physics of the HCM, we use the one-dimensional structure (shown in Figure 2.1) as an example. The incidence light is the x-z plane which is perpendicular to the bars in the y-direction. The plane wave incidence can have two polarizations: transverse electric (TE) polarization and transverse magnetic (TM) polarization. In TE polarization, the electric field ($\vec{E}$) and magnetic field ($\vec{H}$) can be expressed as $\vec{E} = (0, E_y, 0)$ and $\vec{H} = (H_x, 0, H_z)$ respectively. In TM polarization, $\vec{E}$ and $\vec{H}$ can be written as $\vec{E} = (E_x, 0, E_y)$ and $\vec{H} = (0, H_y, 0)$. Because TE and TM polarization are orthogonal to each other, optical field can be solved independently and any arbitrary polarization can be treated as the linear superposition of TE and TM polarizations.
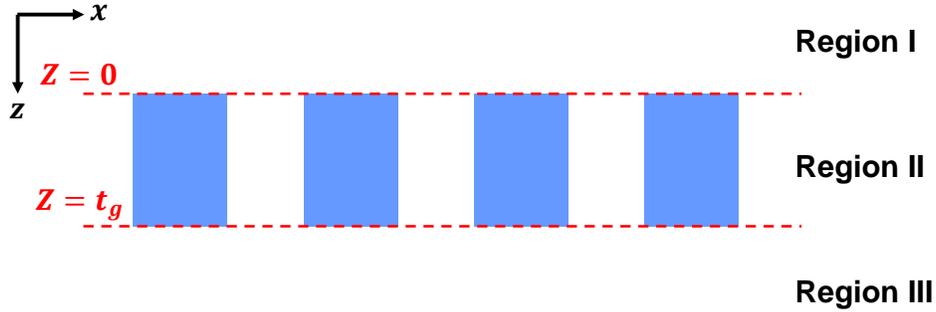
Figure 2.3 The cross section of the 1D HCM. The input plane is $z = 0$ and the exit plane is $z = t_g$. The space is divided into three regions with the HCM layer in region II and low index space outside of the HCM in region I and region III.

We analyze such structure based on the matrix Fabry-Perot analysis of the array waveguides [38-40]. The bars can be considered as a periodic array of waveguides with the light being guided in the z-direction. We first assume the number of the periods in x-direction is infinite. Thus, the periodic boundary conditions can be applied to solve the eigen-modes of the array waveguide. Figure 2.3 is shown to help defining the spatial region for the physics analysis. Upon plane wave incidence, the light propagating inside the HCM (in region II) can be decomposed as the superposition of the eigen-modes of the array waveguide. Figure 2.4 illustrates the optical mode profiles for a set of TE polarized eigen-modes. With an oblique incidence, both cosinusoidal (symmetric) and sinusoidal (anti-symmetric) eigen-mode can be excited. The symmetric modes have even order numbers, such as 0th, 2nd, etc while the anti-semmetric modes have odd order numbers, such as 1st, 3rd, etc.

Because the period of the HCM is very close to the wavelength of interest, only a small number of modes can be excited. In fact, the number of the propagation eigen-modes can be used as a metric to determine the diffraction operation regime. Under deep-subwavelength region, only 0th order is allowed. In the near-wavelength region, typically only 2~3 modes are allowed. And there exists a large number of propagation modes when the grating is in the conventional diffraction region where the period is much larger than the wavelength.
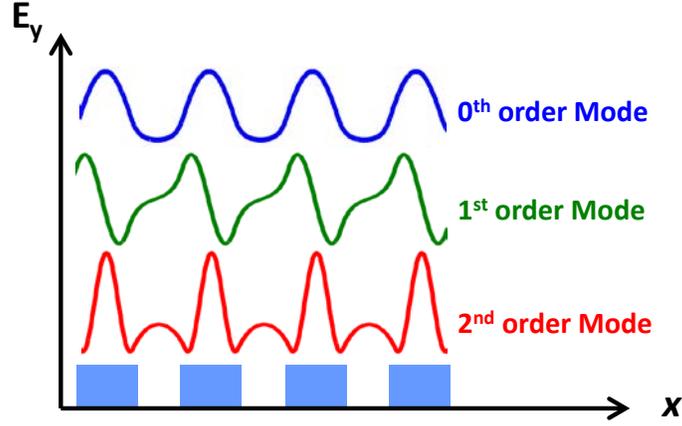
Figure 2.4 The illustration of the mode profile for the array waveguide solved under the periodic boundary condition.

While the light is propagating in region II, the eigen modes do not couple to each other because of the orthogonality. Thus, the matrix formation of the propagation can is diagonal, written as:

$$\varphi_{m,n} = \begin{cases} e^{-j\beta_m z} & m = n \\ 0 & m \neq n \end{cases} \qquad 2.1$$

Firstly, we define the reflection $\boldsymbol{\rho}$, which reveals how the optical profile is modified by the reflection at the interface. In addition, we need to define the vector for the coefficients of the different eigen-modes propagating in the $+z$ and $-z$ direction, as:

$$\boldsymbol{a} = (a_0, a_1, a_2, a_3, \dots)^T, \boldsymbol{b} = (b_0, b_1, b_2, b_3, \dots)^T \qquad 2.2$$

The relationship between $\boldsymbol{a}$ and $\boldsymbol{b}$ is described by :

$$\boldsymbol{b} = \rho\boldsymbol{a} \qquad 2.3$$

At the interface (both input and exit plane), because of the abrupt refractive index change, there existing the coupling between the eigen-modes in the reflection process at the interface, in order to match the boundary condition, leading to non-diagonal matrix $\boldsymbol{\rho}$. Such a phenomenon can be explained by the couple mode theory as following. The light propagation in region I and region III can be expressed as the Fourier series with the basis $\boldsymbol{U} = \left\{ e^{-jm\frac{2\pi}{\Lambda}x} \right\}$, where m is the integer as $1, 2, 3, \dots$. Each array waveguide eigen-mode can be expanded into the same basis $\boldsymbol{U}$. The boundary condition needs to be matched at each dimension of the basis. It is considered as the expansion of each array waveguide eigen-mode in $\boldsymbol{U}$, that have a reflection and transmission coupling coefficient with every element in the coefficient could be non-zero. For instance, if we look at the electric field, given eigen-mode l and k have the expansion under $\boldsymbol{U}$ with the coefficient vector $\boldsymbol{E_l}$ and $\boldsymbol{E_k}$. Because the mode l and k are orthogonal, $\boldsymbol{E_l} \cdot \boldsymbol{E_k} = 0$. The reflection coefficients for mode l and k are $\boldsymbol{r_l}$ and $\boldsymbol{r_k}$. The abrupt index change at the interface makes the eigen-mode scatter

19

into many plane wave elements in U. Essentially, mode l can couple into many dimensions in U and the optical power in U can be coupled back into other eigen-mode k. Such a process therefore leads to the non-diagonal elements in ρ.

The boundary condition can be matched in the following process. Define the overlap integral coefficient between the eigen-modes and the plane wave basis U as E and H, for electric and magnetic fields, respectively. The transmission coefficient at the interface is:

$$\tau = H(a - b) = E(a + b) \qquad\qquad 2.4$$

Using the definition of ρ in equation 2.3, equation 2.4 can be rewritten as following with defining I as the unity matrix:

$$\tau = H(I - \rho)a = E(I + \rho)a \qquad\qquad 2.5$$

Thus, the reflection coefficient can be derived as a function of H and E:

$$\rho = (I + H^{-1}E)^{-1}(1 - H^{-1}E) \qquad\qquad 2.6$$

For each single trip propagation in region II, the phase accumulation φ can be calculated as $z = t_g$ in equation 2.1. Thus, at the input plane, the boundary condition becomes:

$$(I - R)^{-1}H(1 - \varphi\rho\varphi) = (I + R)^{-1}E(I + \varphi\rho\varphi) \qquad\qquad 2.7$$

This equation can be re arranged as:

$$E(I + \varphi\rho\varphi)(I - \varphi\rho\varphi)^{-1}H^{-1} = (I + R)(I - R)^{-1} \qquad\qquad 2.8$$

Similar to the conventional fabry-perot calculation with scalars, we can define the impedence as $Z_{in} = E(I + \varphi\rho\varphi)(I - \varphi\rho\varphi)^{-1}H^{-1}$. Thus, the reflection is calculated as:

$$R = (Z_{in} + I)^{-1}(Z_{in} - I) \qquad\qquad 2.9$$

Similarly, the transmission can be calculated as:

$$T = 2E(I + \rho)\varphi\left[(Z_{in}^{-1} + I)E(I + \varphi\rho\varphi)\right]^{-1} \qquad\qquad 2.10$$

2.2 Unique Optical Phenomena from HCM

Based on the matrix formulation discussed in section 2.1 , the analytical solution for calculating the reflection and transmission of the HCMs can be derived. We developed a mechanism to reveal the reflectivity and transmission with varying the HCM parameters. As shown in Figure 2.5(a), we calculate the reflectivity of the HCM by changing the wavelength as well as the HCM thickness

with TE polarized light surface normal incidence. For the simplest scenario, we assume the HCM is made of non-dispersive material with a fixed refractive index $n_{bar} = 3.48$, which is the index of silicon at $1.55\ \mu m$ wavelength. Therefore, the reflection spectra of the HCM are scalable with the period Λ by fixing the duty cycle, which means the HCM should keep the same optical property with fixed $\frac{t_g}{\Lambda}, \frac{\lambda}{\Lambda}$ and η, even though the absolute value of t_g and λ can be varied by scaling Λ.
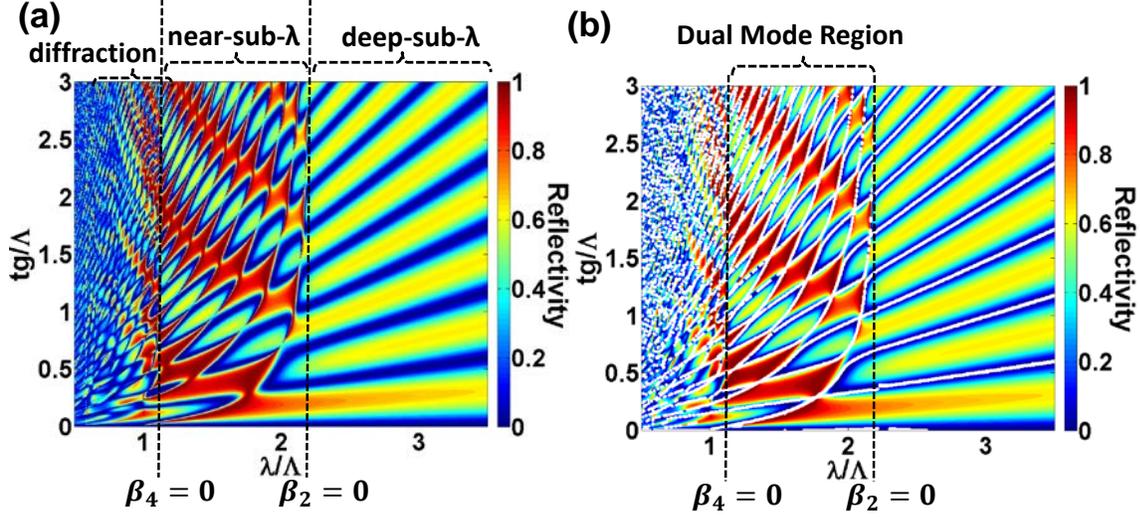
Figure 2.5 (a) The reflectivity contour plot of the HCM as a function of the wavelength and the HCM thickness. (b) The same contour plot as (a) with the overlay of the FP resonance condition of each individual eigen-modes, highlighted by the white line. The HCM parameters are $\eta = 0.6$. The refractive index is $n_{bar} = 3.48$ and $n_o = 1$. The incidence has TE polarization.

The contour plot in Figure 2.5(a) reveals abundant information regarding to the HCM properties. First of all, the contour plots show a checkboard pattern with three distinctive regions with different wavelength. In the regime marked as deep-sub-λ, the reflectivity has periodic peaks at a fixed wavelength, which is very similar to the reflection spectrum of a thin film. This is known as the deep subwavelength regime that mentioned in section 2.1 . It can be modeled by the average index model and only the 0th order array waveguide mode exists in the HCM. In the diffraction regime, because the large number of the eigen-modes exist in the HCM, the interference of the modes gives complex grid patterns.

The most interesting regime for HCM is the near subwavelength regime, which the pattern is created as the crossing of two sets of lines. To further understand this regime, we plot the lines where the eigen-modes satisfy the FP resonance conditions ($\Psi_n = m\pi, m = 0, 1, 2, ...$) and overlay the lines with the contour plot in Figure 2.5(b). It shows a dual mode regime cross a very broad wavelength range, which only allows the propagation of two eigen-modes. That means the characteristics of the HCM are mainly determined by the interference of two eigen-modes. Given the surface normal incidence, only symmetrical modes are excited. The propagation modes in the dual mode regime are 0th and 2nd mode. The higher order modes have imaginary propagation constant and strongly bounded at the interface. They still need to be included for matching the

boundary conditions in order to have a complete set for the mode profile expansion. However, the high order modes can be neglected for evaluating the light propagation, as a good approximation to simplify the calculation.

Inside the dual mode regime, the resonance lines of 0th and 2nd order may have crossing. With the zoom-in of the crossing regime, we observe two type of the crossings. One is called anti-crossing, where the lines repel each other. Such an anti-crossing phenomenon is also observed in other physics areas, including coupled quantum-dot cavities [41, 42] and photonic crystal [43]. It indicates the strong coupling between two modes. In the case for HCM, we find the anti-crossing happens when the phase difference between 0th and 2nd mode satisfies $|\Delta\Psi| = \Psi_2 - \Psi_1 = 2m\pi$. Under this condition, the resonance of the two modes are in-phase, which can support each other. The optical field accumulates and the field intensity can be greatly enhanced by millions of times, as shown in Figure 2.6(a). It makes the HCM as an excellent resonator.
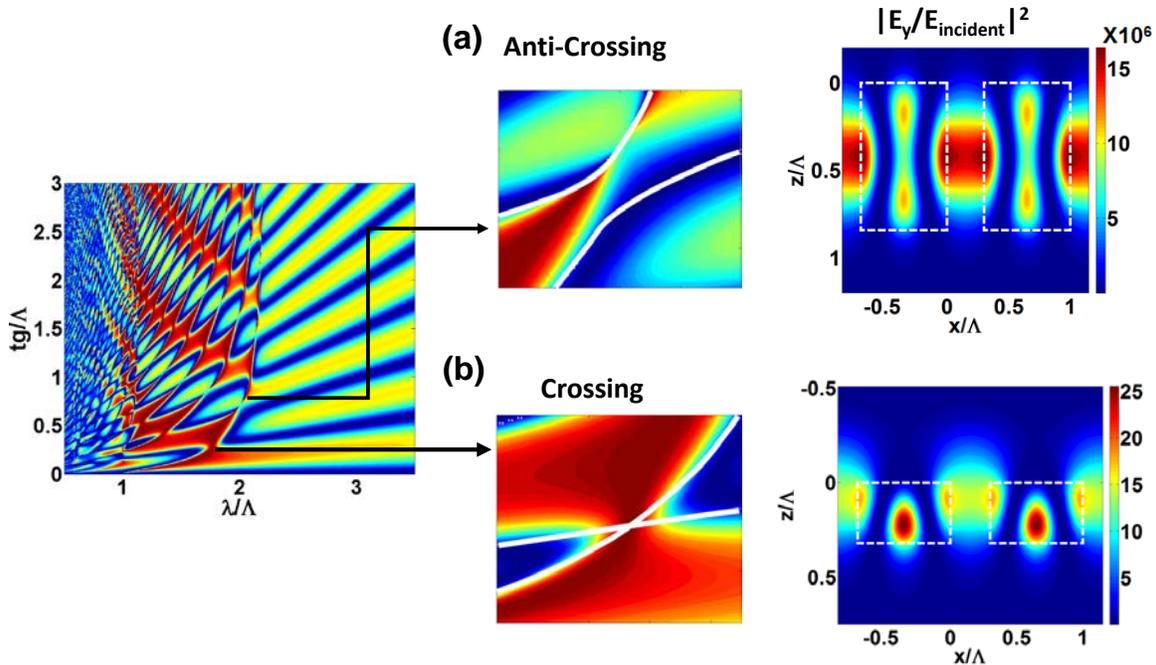
Figure 2.6 The zoom-in of the reflection contour plot (left) and the optical field profile (right) for (a) anti-cross and (b) crossing

On the other hand, if the resonance is out of phase, which leads to $|\Delta\Psi| = \Psi_2 - \Psi_1 = (2m + 1)\pi$, the modes create destructive interference. The field enhancement factor is low. It creates the regular crossing, shown in Figure 2.6(b). Very broadband and high reflectivity region can be found around the crossing.

Many interesting applications have been investigated based on the crossing (broadband high reflectivity) and anti-crossing (high-Q resonance) phenomena. As illustrated in the introduction chapter, the reflection type HCM has been used as the mirror for the vertical cavity surface emitting lasers [22, 23, 28]. It is also used as the reflection wall for the hollow core waveguide [44]. The

resonance type HCM are experimentally demonstrated [45] and used as the low cost biosensors [33].

2.3 Diffraction Order Cancelling

Despite the studies in the diffraction regime and the deep sub-wavelength regime from more than a hundred years ago and the study on the sub-wavlength regime in the past decades, there is still a regime that has been seldom studied and used, where only a few, typically two diffraction orders are allowed. Here we name it dual order diffraction regime.
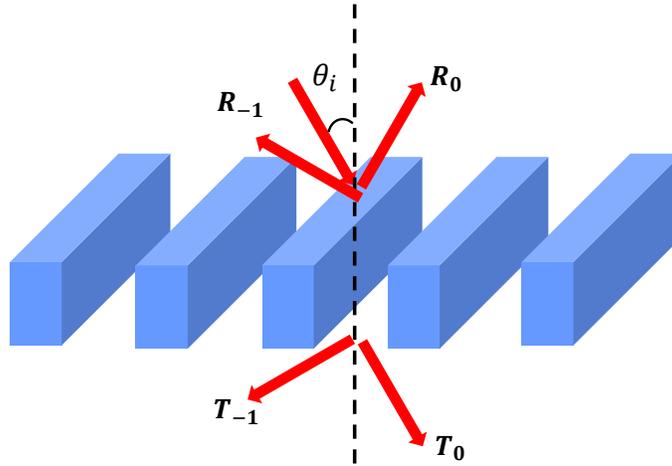
Figure 2.7 The schematic of the HCM in the dual order diffraction regime.

Let's start with the most fundamental grating equation:

$$\Lambda(\sin\theta_m + \sin\theta_i) = -m\lambda, m = \cdots, -2, -1, 0, 1, 2, \cdots \qquad 2.11$$

With oblique incidence, the diffraction angle of mth order is determined by the grating equation in 2.11. When the period is very close to the wavelength, either larger or smaller than λ, there exists a regime that only allows two diffraction orders, who are shown as the 0th order and -1st order in Figure 2.7. Here, we define all angles to the left of the normal axis to be positive and angles to the right of the normal axis to be negative. Therefore, we can model the HCM as a four-port device, with R_0, R_{-1}, T_0 and T_{-1} ports.

We perform the same matrix calculation that described in section 2.1 . The plane wave incidence from region I can be expressed as $C = (\dots\ 0\ 0\ 1\ 0\ 0\ \dots)^T$. We can solve the reflection and transmission from equation 2.9 and 2.13.

Similar to the subwavelength regime, where the HCM can be designed to cancel the transmission to achieve ultra-high reflection or cancel the reflection to achieve ultra-high transmission. In fact, it is possible to configure the interference of the eigen-modes in the HCM to enhance any arbitrary order while annihilating the rest of the orders. The examples for such designs are shown in Figure

2.8. We assume the incidence light has TM polarization. Figure 2.8(a)(b) show R_{-1} and R_0 spectrum with duty cycle $\eta = 0.4$ and 30° incidence angle. The wavelength and thickness in the plots are normalized by the period. The region highlighted in Figure 2.8(a) shows more than 90% power being enhanced into the -1st order. It is very unique comparing with the conventional gratings. This property is also found for the transmission type. Figure 2.8(c)(d) shows the T_{-1} and T_0 spectrum for HCG with duty cycle $\eta = 0.1$ and 35° incidence angle. The enhanced region is also highlighted in Figure 2.8(c).
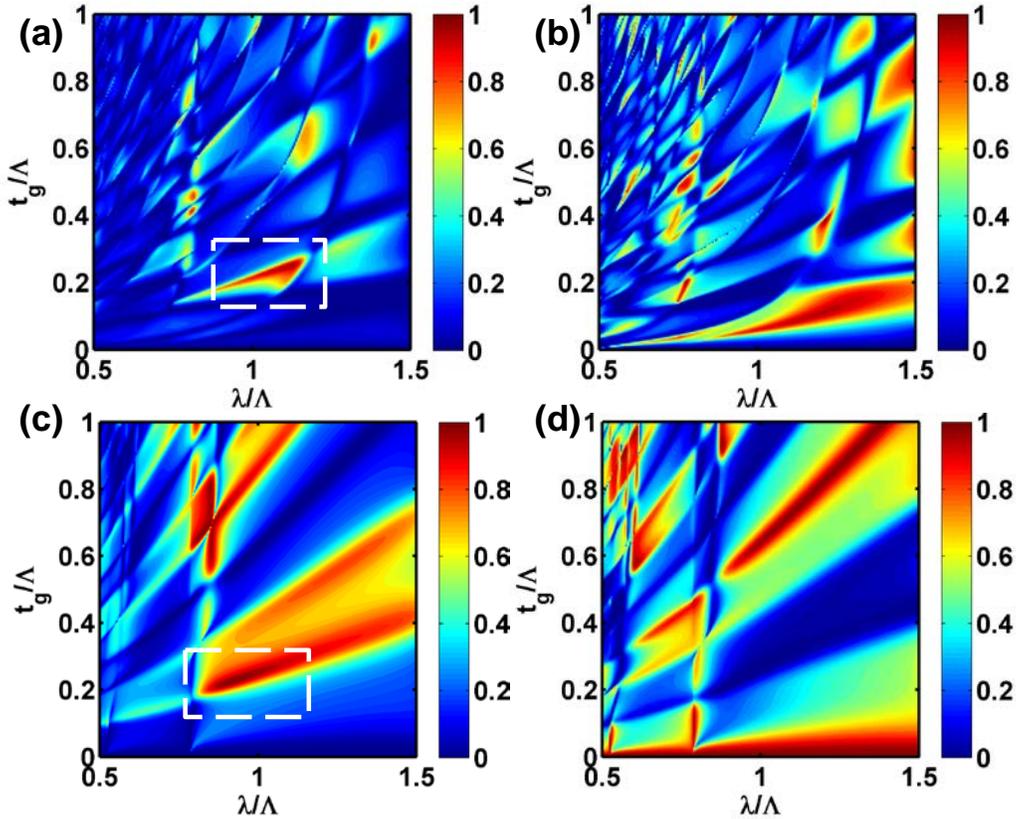
Figure 2.8 (a) R_{-1} and (b) R_0 for TE-HCG with 0.4 duty cycle and 30° incidence. (c) T_{-1} and (d) T_0 for TE-HCG with 0.1 duty cycle and 35° incidence. The -1st order enhanced regions are highlighted by the white dash line boxes.

When R_{-1} is enhanced up to 100% , the HCM surface diffracts all the incidence power to θ_{-1}. It is very different from the reflection angle predicted by the Snell's law. Essentially, the HCM creates an anomalous reflection in contrast to the Snell's law. Similarly, when T_{-1} is enhanced to 100%, the HCM creates an anomalous refraction with cancelling all the reflections. Such a phenomenon is illustrated in Figure 2.9. For anomalous reflection, the HCM design is $t_g = 340nm$, $\Lambda = 1364nm$, $\eta = 0.41$. At 35° incidence angle, TM polarized light at 1550 nm wavelength can be fully diffracted into the -1st order. For the anomalous transmission design, the HCM with $t_g = 380nm$, $\Lambda = 1664\ nm$, $\eta = 0.1$ can have all the incidence light diffracted into the -1st order. The bottom figures in Figure 2.9 are the electric field profile calculated by the finite-difference time-domain (FDTD) method [46]. The field profile proves that almost all of the

diffraction light has been concentrated in to the -1st order for both reflection and transmission design, which makes the output light beam at the same side of the incidence light as respect to the surface normal axis.
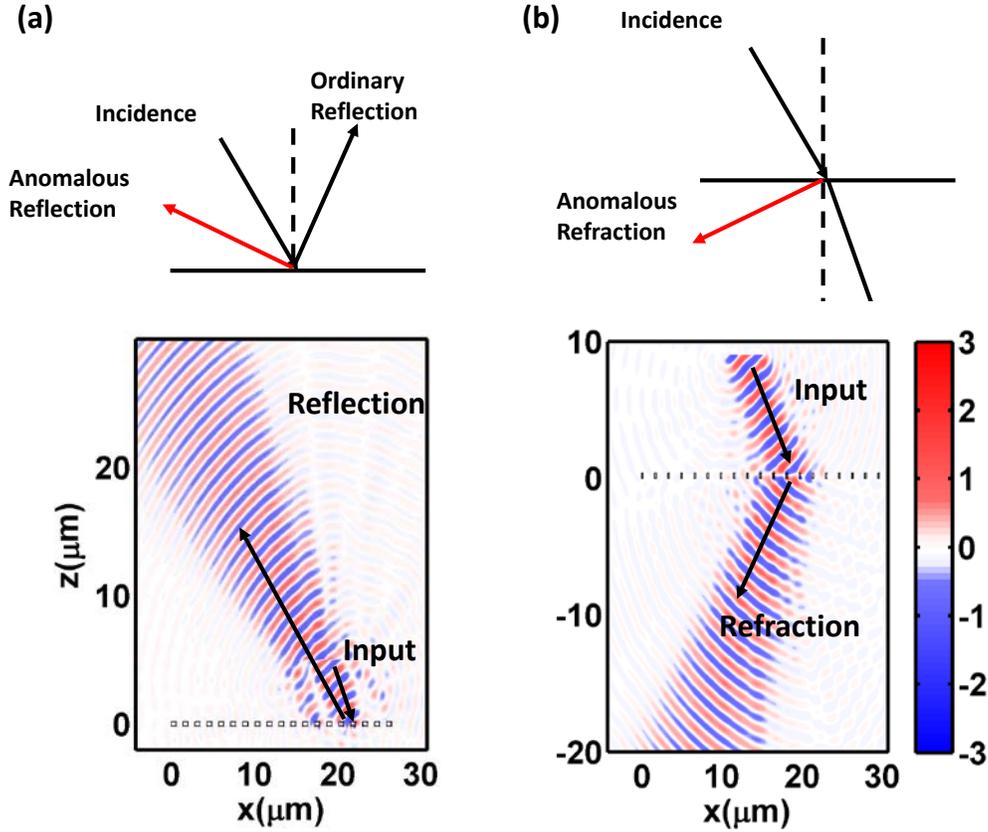
Figure 2.9 The schematic and electrical field of (a) the reflection anomaly with the incidence angle is 35° and the reflection angle is 31.7^{o} (b) of the refraction anomaly with the incidence angle is 30° and the refraction angle is 26.5^{o}.

The anomalous reflection (or refraction) from a metastructure has been discovered with two dimensional metal antennas [37, 47]. Each metal antenna element can be designed to provide a spatially varied phase plate with sub-wavelength resolution to for beam shaping. By designing the linear phase front, it is able to create an interface to have the reflection or refraction in contradiction to the Snell's law, as schematically illustrated in Figure 2.10. The phase distribution $\phi(x)$ can be written as:

$$\phi(x) = -\frac{2\pi}{\lambda}(\sin\theta_i + \sin\theta_r)x \qquad 2.12$$

However, the phase distribution has strong phase dependence on the wavelength. Unfortunately, the phase of the metal antennas has a very different spectra response. It creates huge challenge to match the phase distribution of the metal antenna array to the phase function with varied wavelength. In addition, the phase distribution in equation 2.13 also depends on the incidence

angle θ_i. Therefore, the metal antenna approach can only be optimized for a very small wavelength bandwidth and incidence angle range.
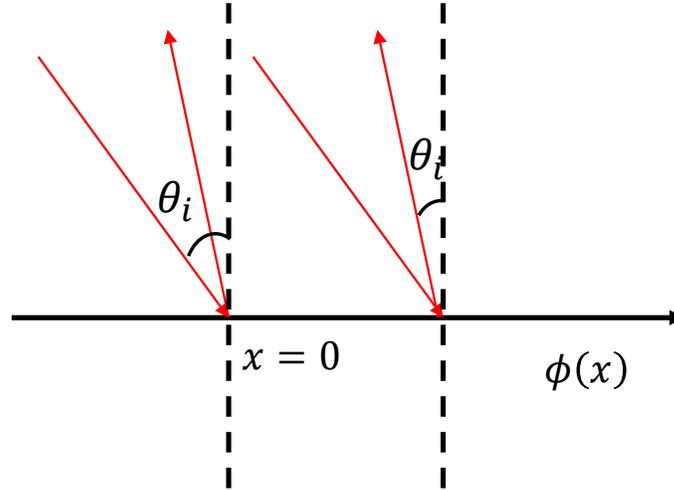
Figure 2.10 The schematic of the anomalous reflection created by a phase modulated surface. The phase distribution follows equation 2.13.

On the other hand, as shown in Figure 2.8, the anomalous reflection and refraction from the high contrast metastructures can be very broadband. We use the HCM design in Figure 2.9 to evaluate the angular and spectra tolerance. For the reflection type, we first fix the incidence angle at 35º and calculate the diffraction spectrum for R_{-1}, shown in Figure 2.11(a). The calculation result indicates a bandwidth of 110nm to keep $R_{-1} > 0.9$. Such an approach has a superior performance for the power efficiency due to minimum material loss with additional benefit for its broad bandwidth. The incidence angle dependence is also evaluated in Figure 2.11(b), which we fix the wavelength at 1.55 µm and change the incidence angle θ_i. The result shows a very flat response within a 22º angle range (25º to 47º) to keep R_{-1} greater than 0.9. Similarly, the tolerance for the transmission type of HCM design is calculated in Figure 2.12. The $T_{-1} > 0.9$ region covers 170nm wavelength range and the incidence angle can vary from 10º to 50º at 1.55µm wavelength while keeping T_{-1} greater than 0.9.
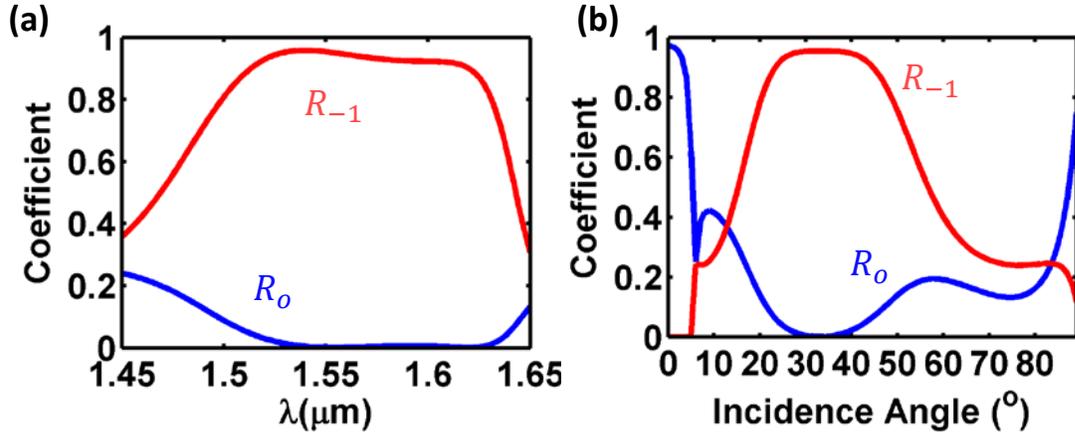
Figure 2.11(a) The spectrum of the reflection anomaly with 35° incidence angle. (b) The angular dependence of the reflectivity at 1.55µm wavelength.
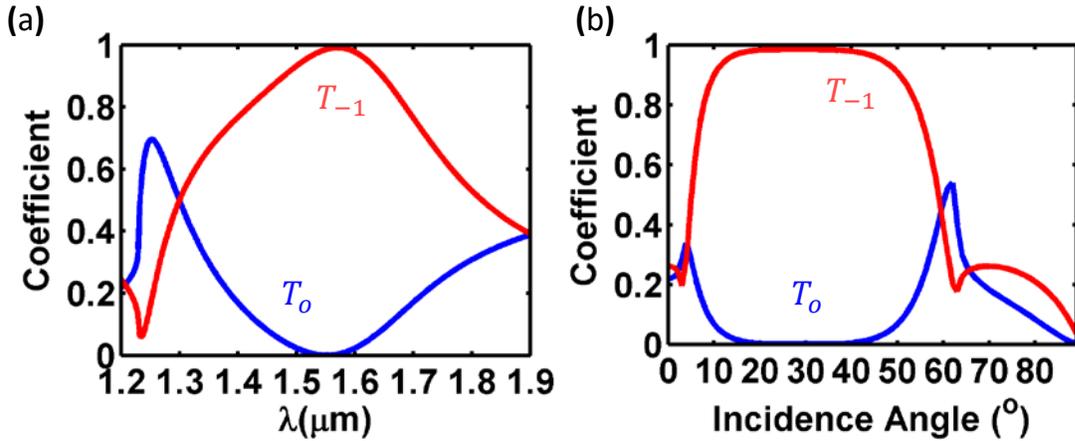
Figure 2.12 (a) The spectrum of the transmission anomaly with 30° incidence angle. (b) The angular dependence of the transmission at 1.55µm wavelength.

This broadband anomalous diffraction phenomenon is very useful for spectroscopy or color splitting applications. For the conventional gratings, the power distribution is determined by:

$$I(\theta) = I_0 \left(\frac{sin\beta}{\beta}\right)^2 \left(\frac{\sin N\alpha}{\sin \alpha}\right)^2, \ \beta = \frac{kb}{2}sin\theta \ and \ \alpha = \frac{k\Lambda}{2}\sin \theta \qquad 2.13$$

Here λ is the period and b is the width of the opening slit. The maximum power for this grating is allocated in the central maximum where $\theta = 0$. However, it does not give spectral resolution in 0th order. The spectral resolution is better in the higher orders, but the intensity is lower. The method being used for the spectrometers are to use the blazed gratings [48]. It has a triangular tooth shape grating surface to achieve the maximum grating efficiency in a particular diffraction order. However, the blaze condition is valid only when the equation $2\Lambda \sin \theta_B = m\lambda$ being satisfied. Therefore, similar to the metal antenna approach, the blazed grating is only optimized

27

for a certain wavelength and generally is a narrow band effect. In addition, for the nano-photonics applications, the triangular tooth shape is difficult to etch. Therefore, the HCM is very promising to replace the conventional wavelength splitting elements with high efficiency over broad bandwidth.

2.4 Finite Size HCM

2.4.1 Finite Size HCM Resonator

Start from section 2.1 , we used the assumption that the 1D HCM has infinite length in y-direction and infinite number of periods in x-direction, as shown in Figure 2.1. However, it is not true for the real devices, especially when the application requires the HCM to have comparable size as the light beam size. Therefore, it is important to study how characteristics of the finite size HCM deviate from the prediction based on the infinite size HCM model.

We first look at the HCM for the high quality factor (Q-factor) resonators. The Q-factor can be calculated using the FDTD simulation. A HCM resonator is designed as as $\Lambda = 716.3nm$, $t_g = 1494.1nm$ and $\eta = 0.7$ to achieve a high Q value with infinite number of grating bars [40]. It is designed to resonate at 1.55 μm wavelength for TE polarization. The corresponding t_g-λ contour plot is shown in Figure 2.13. It is the anti-cross when $\Psi_0 = 6\pi$ and $\Psi_2 = 2\pi$. As predicted in section 2.2 , because $\Delta\Psi$ ($\Delta\Psi = |\Psi_2 - \Psi_0| = 4\pi$) is an even number of π, high-Q resonance should happen at this anti-crossing.
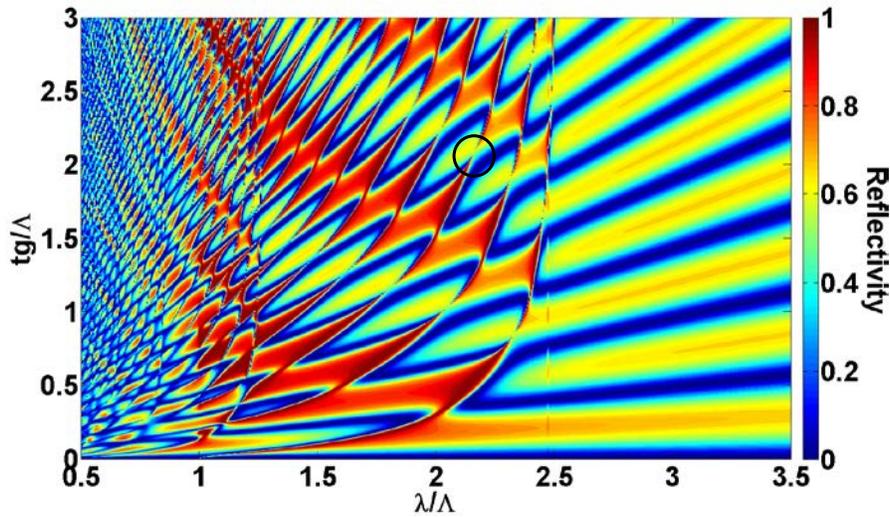
Figure 2.13 The reflectivity contour plot of the HCM as a function of the wavelength and the HCM thickness. The duty cycle is 0.7. The incidence light has TE polarization from surface normal direction. The anti-crossing point chosen for the resonator is highlighted by the black circle.

The spectrum at this anti-crossing can be calculated with the analytical formulation. As shown in Figure 2.14, the spectrum has a Fano resonance shape [49]. The fitting based on the Fano resonance

gives the quality factor around $1{,}63 \times 10^7$. The optical field profile at resonance is also plotted in Figure 2.14(b).
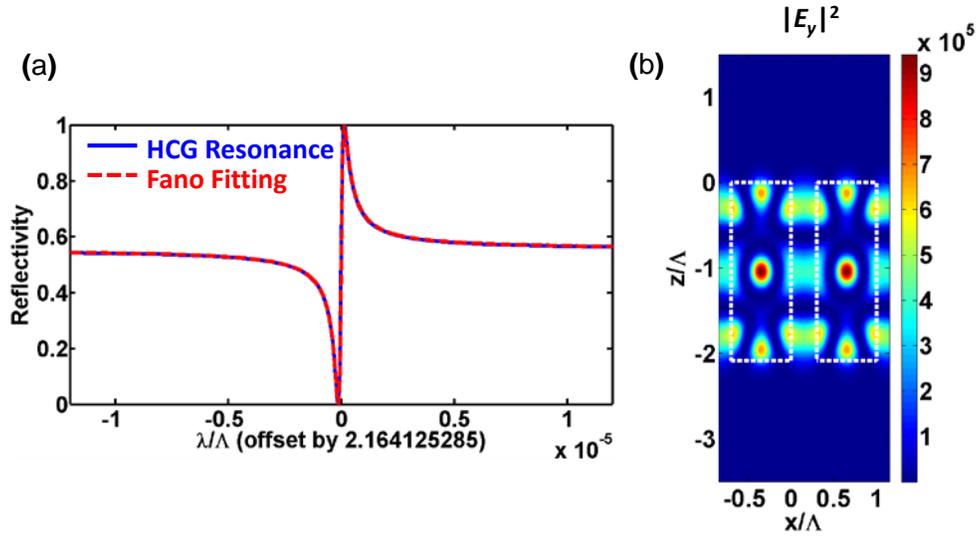
Figure 2.14 (a) The reflection spectrum of the HCM resonator. It is fitted by the Fano-Resonance function to deduce the quality factor. (b) The optical profile of the HCM under resonance.

In the FDTD simulation setup, the TE dipole sources are randomly placed to excite the light wave. Such excitation can stimulate different modes of HCG, as explained in section 2.1 . However, given different modes have distinctive quality factor in the resonator, only one particular mode with the highest Q is expected to exist after a certain time evolution. By performing this simulation, the field intensity evolution with time is obtained. Firstly, we put the periodic boundary condition in FDTD simulation to get the quality factor of the infinite period HCG resonator; the field intensity evolution is plotted in Figure 2.15. After the dipole excitation (30 fs long) is launched, light is coupled into different modes of the resonator. In the initial 8000 fs, multiple modes exist and the overall decay speed is fast. With all low Q modes vanishing, only the mode with highest Q exists and is decaying exponentially with a long lifetime. The photon lifetime of the target high Q mode is fitted and the quality factor is calculated to be 6.54×10^6. Because the derived quality factor of a high-Q resonator from the FDTD simulation is extremely sensitive to the mesh grid size, which is limited to a few angstroms in the FDTD setup, the Q value from the FDTD did not achieve perfect agreement with result from the analytical solution. However, it can be still considered as a good verification because the Q values from the two different methods are in the same order of magnitude.
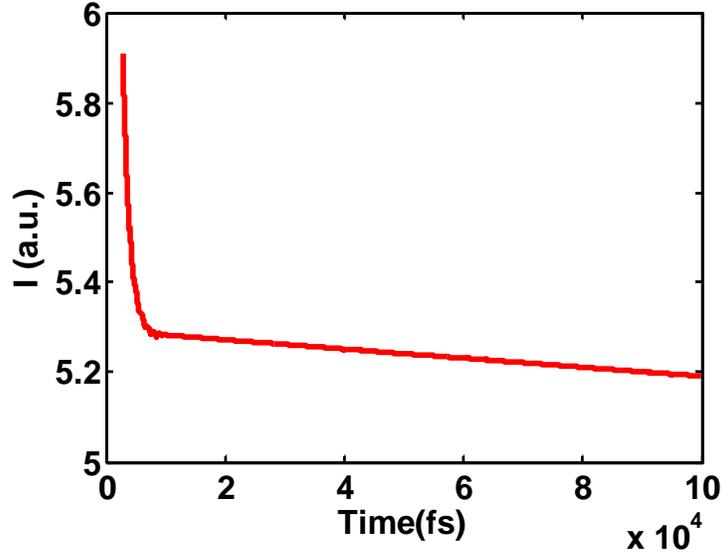
Figure 2.15 The field evolution with time of the infinite period HCG resonator. By fitting the photon lifetime of the slowly decaying portion, the quality factor could be obtained.

Following the aforementioned procedure, the quality factors with different resonator bar number N are simulated, as shown in Figure 2.16. Starting from one bars, the quality factor keeps increasing exponentially, from $Q = 44$ with 1 bar to $Q = 417$ with 5 bars. With adding more HCM bars, the quality factor still grows exponentially but with a lower growth factor. When the resonator has 20 grating periods, making HCG resonator possess a 15 μm aperture, Q value is around 10,000.
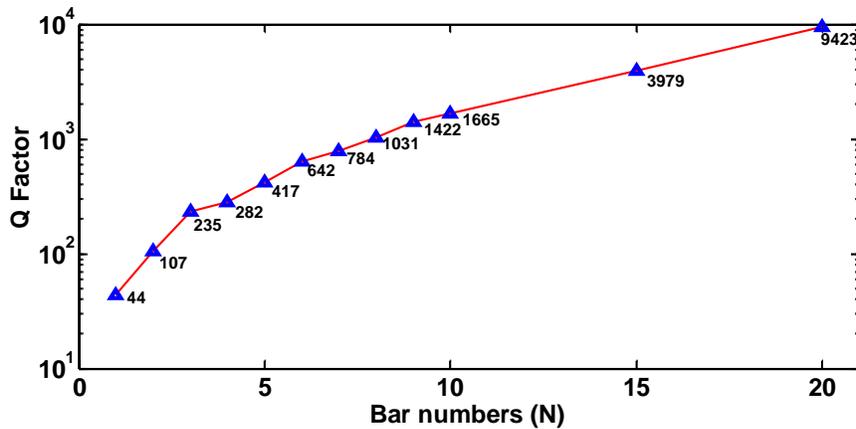
Figure 2.16 The relationship between HCG bar numbers and resonator quality factor from 2D FDTD simulations.

In Figure 2.17, the resonance field profiles from $N = 1$ to $N = 10$ are plotted. Comparing this finite period resonator field profile with the infinite case, the resonance mode has similar pattern

30

and the light in the finite period resonator is confined in the center grating bars. Given the light intensity peak is located at the center of the grating bar, by putting the gain material in the bar center, it is possible to utilize HCG itself as a resonace cavity and make a surface emitting laser. Such configuration is not limited by the resonator aperture and is able to scale to large area to make high power surface emitting semiconductor lasers.
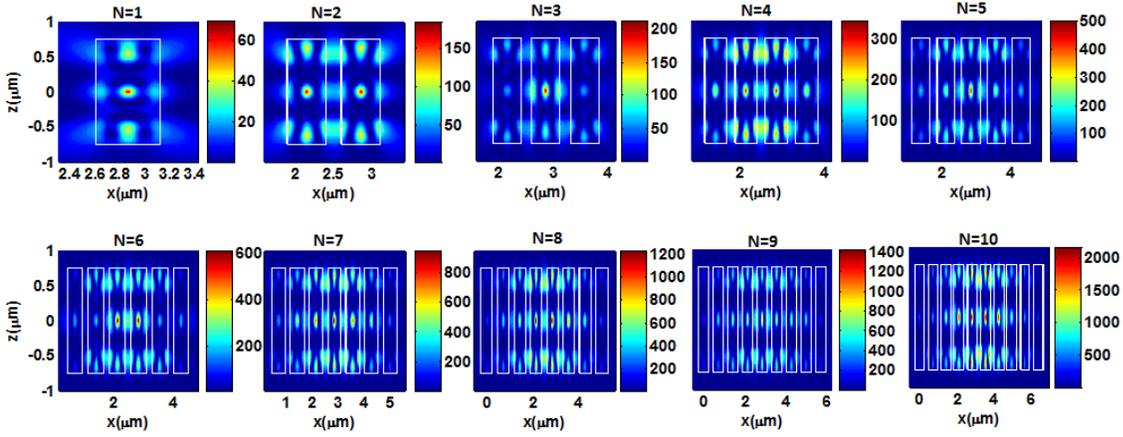
Figure 2.17 The field profile of the HCG resonator with 1 to 10 periods.
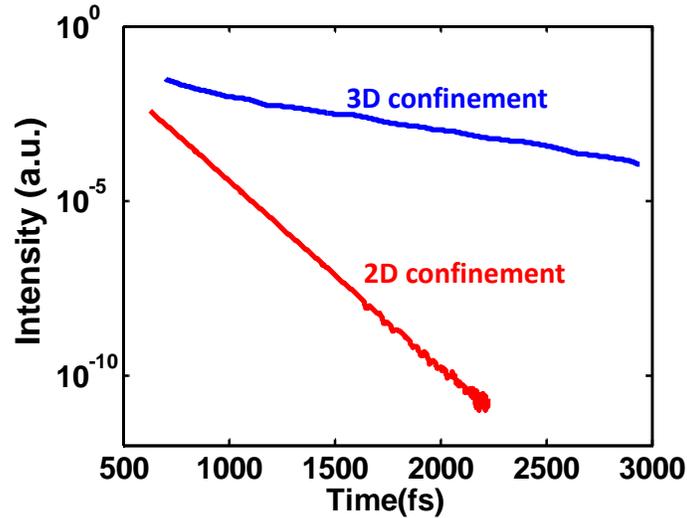
Figure 2.18 Comparison of the field evolution for 2D and 3D confinement of HCG resonator with two periods.

For small apertures HCG resonators, such as two periods HCG with aperture size ~1.2 μm, the confinement effect in y direction needs to be considered. Given Q value for this resonator is relatively low ($Q=104$), additional confinement can provide better quality factor. By performing three dimensional FDTD simulation, the quality factor for such HCG resonator with ~0.58 λ^3 volume is 405. The comparison of the time evolution for the resonator with and without y direction confinement is plotted in Figure 2.18. Further minimization of the HCG dimension is possible with

31

smaller HCG thickness. This high Q resonator with subwavelength dimension in all three dimensions enables many applications in nanostructured resonate cavity, including: compact light source, compact second harmonic generator with III-V HCG, optical antenna, etc.

It is important to note that not all HCM resonator has the same performance as the number of the bars is reducing. It strongly depends on the cavity mode profile. Figure 2.19 shows the cavity mode profile of two different HCM resonators, which has been discussed previously. The resonance in Figure 2.19(a) happens when $\Psi_2 = 0$, $\Psi_0 = 2\pi$. It is the lowest order resonance. The intensity peak locates at the low index gap. When the size of the HCM is reduced, the scattering at the boundary tends to be strong because the field is confined by the structure periodicity, which is broken at the boundary. The quality factor under this condition will be dramatically reduced from the infinite HCM case. On the other hand, for the high order resonance, the intensity peak is confined inside the high index region, as shown in Figure 2.19(b), the field at the boundary of the finite size HCG is much weaker comparing with the low order resonance. The quality factor can be maintained as the number of the bars is reducing.

$$\Psi_2 = 0, \Psi_0 = 2\pi \qquad \Psi_2 = 2\pi, \Psi_0 = 6\pi$$
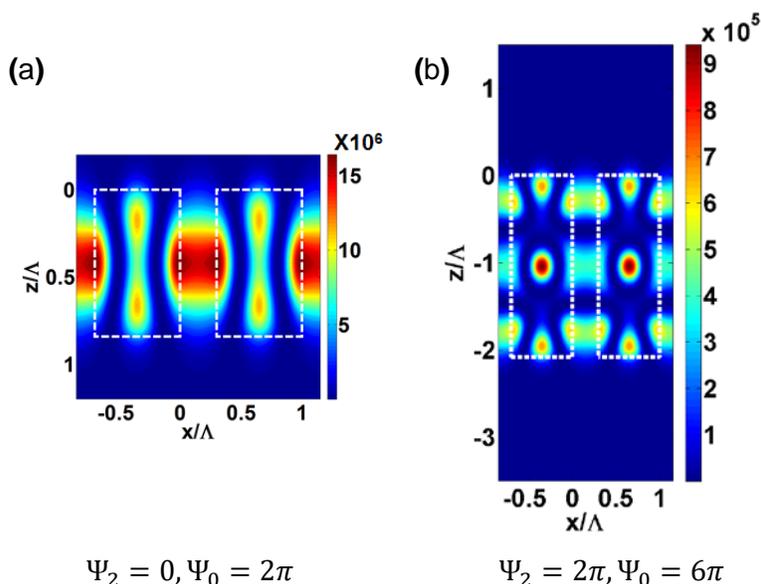
Figure 2.19 HCM resonance cavity mode profile for the anti-crossing at the different location of the tg-λ plot.

2.4.2 Finite Size HCM Reflector

The size effect of the HCM reflector is important to study because the implementation of this reflector usually requires small HCM size. For instance, when the HCM mirror is used as the top reflector of a VCSEL, a smaller size HCM is usually desired for the following reasons. First of all, the HCM structure needs to be released to ensure the high index contrast to the surrounding medium, meaning the layer under the HCM needs to be etched away so the HCM is suspended with being supported by the mechanical beams. The large size HCM creates more difficulties in the release process because it is much easier to collapse. In addition, the built-in stress of the released structure can warp the large size HCM reflector more easily. Moreover, smaller size HCM

is preferred for the wavelength tuning with the MEMS actuation because of the smaller mass. It has been experimentally demonstrated that four HCM bars are enough to ensure the VCSEL to achieve lasing [25].

On the other hand, we observe the beam waist size of the incidence light plays an important role in determining the reflectivity. The contour plot for an InP HCM reflector with TE-polarized plane wave incidence at 1550 nm is shown in Figure 2.20. The HCM dimension is $\Lambda = 1070\ nm$, $\eta = 0.345$. In Figure 2.20(a), the contour plot is calculated by the analytical solutions. It shows a very broad high reflectivity bandwidth with $t_g = 195\ nm$, with the reflection spectrum shown in Figure 2.21(a). However, in the reflection contour map with the same HCM design simulated by FDTD method with Gaussian beam incidence, there exist a reflection dip pass through the high reflection region (Figure 2.20(b)), leading to significant reflectivity drop.
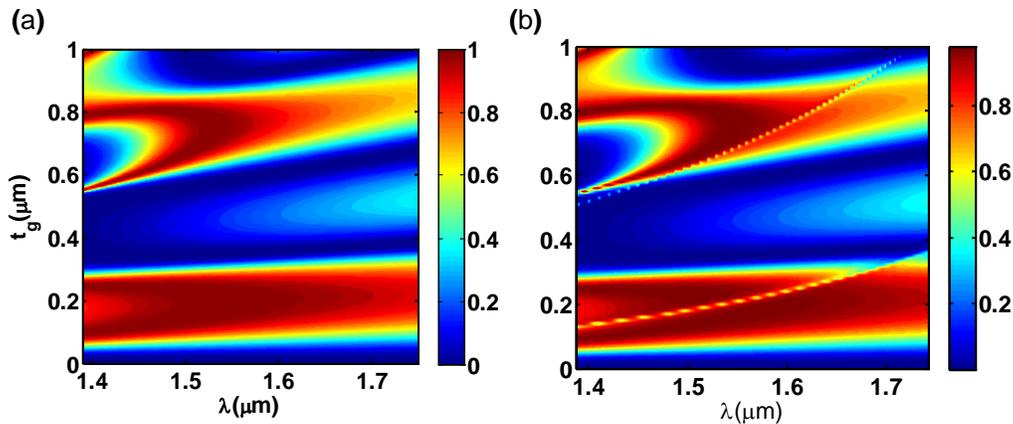
Figure 2.20 (a) Contour map for the InP HCM reflector at 1550 nm wavelength, calculated by the analytical solution (b) Contour map simulated with FDTD solution with a finite waist size.

The difference between the analytical solution and the FDTD simulation is the size of the incidence light. In analytical solution, the incidence light is assumed to be plane wave at surface normal direction. On the other hand, the FDTD simulation uses a Gaussian beam with 8 µm beam waist size, which is typical for the single mode VCSEL output. Therefore, the Gaussian beam has a 3.5° divergence angle. Under oblique angle incidence, in addition to the symmetric modes (even modes), the anti-symmetric modes (odd modes) can also be excited. The resonance of the odd modes creates extra grid patterns to inside the original checkboard pattern in the dual mode region. For the InP HCM design, the resonance curve of the 1st order array waveguide mode pass through the high reflection region, creating this reflectivity drop, as shown in Figure 2.21(b).

(a)

(b)
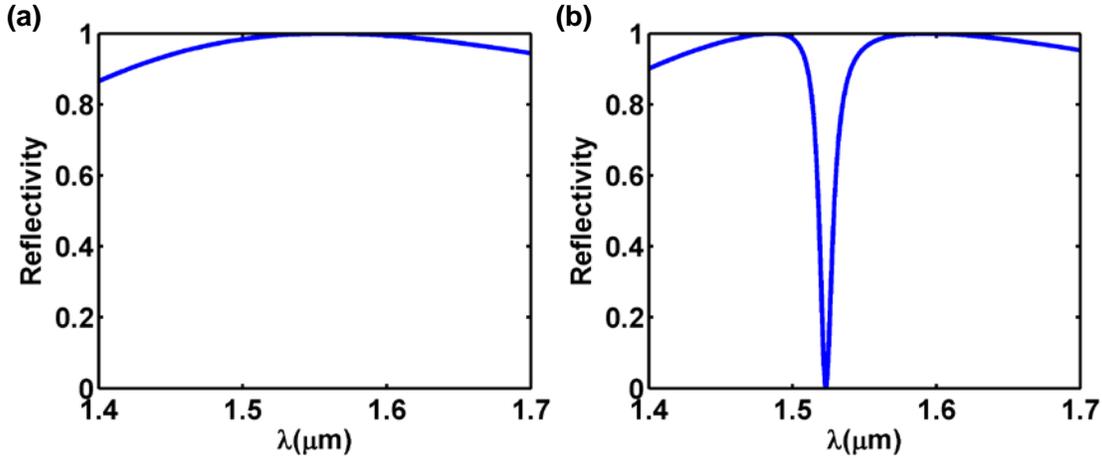
Figure 2.21(a) Reflectivity spectrum for the InP HCM reflector with plane wave incidence. (b) Reflectivity spectrum for the InP HCM reflector with Gaussian beam incidence, whose divergence angle is 3.5°.

Therefore, it is important to include the incidence wave divergence angle into the consideration for the HCM reflector design to avoid the 1st order resonance. For example, the InP HCM reflector can be designed at high reflectivity region around $t_g = 800\ nm$. The 1st order resonance happens at the edge of the high reflection bandwidth, which solves the issue for the original reflector design.

2.5 Summary

In this chapter, the analytical formulation of the high contrast metastructure based on the matrix Fabry-perot approach is presented. Comparing with the well-understood RCWA method that uses plane wave as the basis, the analytical formulation uses the array waveguide eigen-modes as the basis for wave expansion. This approach reveals the physics essence behind the sharp lines in the t_g-λ contour map, explaining the unique properties of the HCM results from the resonance of the array waveguide eigen-modes. In addition, because the wave expansion with the array waveguide modes converges much faster than the plane wave expansion in the HCM region, the calculation complexity is greatly reduced. In the dual mode region, incorporating only two eigen modes can already give very accurate approximation [1], meaning the matrix size is reduced to 2 by 2. Comparatively, the RCWA method at least requires 10 orders, translating into a 21 by 21 matrix.

Unlike the extensive study on the dual mode subwavelength regime, we discover a unique diffraction order cancelling phenomenon in the dual diffraction regime. In this regime, the HCM period is very close to the wavelength of interest and the incidence light is from an oblique angle. This configuration only allows two diffraction orders, known as 0th and -1st order. By the interference inside the HCM region can be designed to enhance any of the orders while annihilating the rest of them. For the HCM made of transparent high index material, the diffraction efficiency in the -1st order can be enhanced to unity, with very broadband wavelength and the incidence angle tolerance. This broadband anomalous diffraction phenomena is very promising for beam steering, color tuning applications.

34

In addition, as the size of the HCM has to be finite, the characteristics can deviate from the theoretical prediction based on the infinite HCM assumption. For the HCM resonator, the quality factor growths with the number of the HCM bars exponentially for the high order resonance whose intensity peak is inside the high index medium. The Q-factor can reach 400 with only 5 bars. For the HCM reflector, the reflectivity can surface from the divergence of the incidence light. While the HCM is designed for ultrahigh reflectivity for surface normal direction, the off-normal light with small oblique angle can have resonance cross the high reflection bandwidth, leading to significant reflectivity reduction. By recognizing this effect, HCM reflector with large angular tolerance can be designed by avoid the oblique angle resonance.

Chapter 3

Flexible High Contrast Metastructures

3.1 HCM Anomalous Diffraction Tuning

The ability to actively control the perceived color of objects is highly desirable for a variety of applications, such as camouflage, sensing, and displays. Such a phenomenon can be readily found in nature - the chameleon is an excellent example. However, the capability to change color at-will has yet to be reproduced by humans. The conventional optical coating relies on accumulative interference across multiple layers to provide high reflection or transmission of specific wavelengths and, thereby, display a corresponding coloration [50]. Such a structure cannot be used for complex color pattern due to the difficulty in controlling the thickness with fine resolution [51].

Diffractive optics offers another way to split colors. While the 0th order diffraction simply follows Snell's law for reflection and refraction, and does not split colors, high-order diffractions have varied propagation directions depending on wavelength. By creating a periodic structure in an elastomeric membrane, control over color perception can be achieved by varying the structural periodicity via membrane deformation. Color tuning has been achieved with the deformation of the elastomeric gratings [52-57]. However, the previously reported structures are made of low index materials and have a very large proportion of optical power concentrated in the 0th order beam. The typical diffraction efficiency at the desired order is less than 10%. The metal coating on the polymer grating helps to improve the efficiency up to 57% for the near infrared wavelength [52]. However, it is still much lower than unity. In addition, the metal coating is also not optimal for all colors. In order to have efficiency color tuning over a wide color range, the broad band diffraction enhancement in an order other than the central maximum is desired.

As described in Chapter 2, the HCM has a unique anomalous diffraction phenomenon. In the dual diffraction order regime, only two diffraction orders are allowed, known as 0th order and -1st order. The interference of the HCM eigen-modes can be designed to enhance any of the diffraction order either for reflection or transmission, while annihilating the rest of the diffraction orders. Once the -1st reflection is enhanced to have $R_{-1}{\sim}100\%$, the anomalous reflection is observed. Similarly, designing $T_{-1}{\sim}100\%$ can create the anomalous transmission.

In addition, the anomalous diffraction is a very broad band effect with large incidence tolerance. As the color of the diffractive optics is determined by its period, the HCM is promising for the color tuning with controlling its structural periodicity. As shown in Figure 3.1, the diffraction efficiency as a function of the gap width is plotted for both R_{-1} and T_{-1} enhancement. Both of the HCM designs are designed for TE-polarization. However, it is important to note that the same effect can be designed for TM-polarization as well.

The contour plots show broadband enhancement in -1st diffraction order with a very wide range for gap width tuning. For R_{-1}, the diffraction efficiency can be kept above 90% at 1550 nm

wavelength, with the gap width of the HCM changing from 720 nm to 1050 nm. The period of the HCM is varied by 25% which is corresponding to a significant diffraction angle change, from 40° to 22°. For T_{-1}, the bar width can vary from 1290 nm to 1710 nm to keep $T_{-1} > 90\%$, giving the angular sweep of the diffraction beam from 35° to 19°.
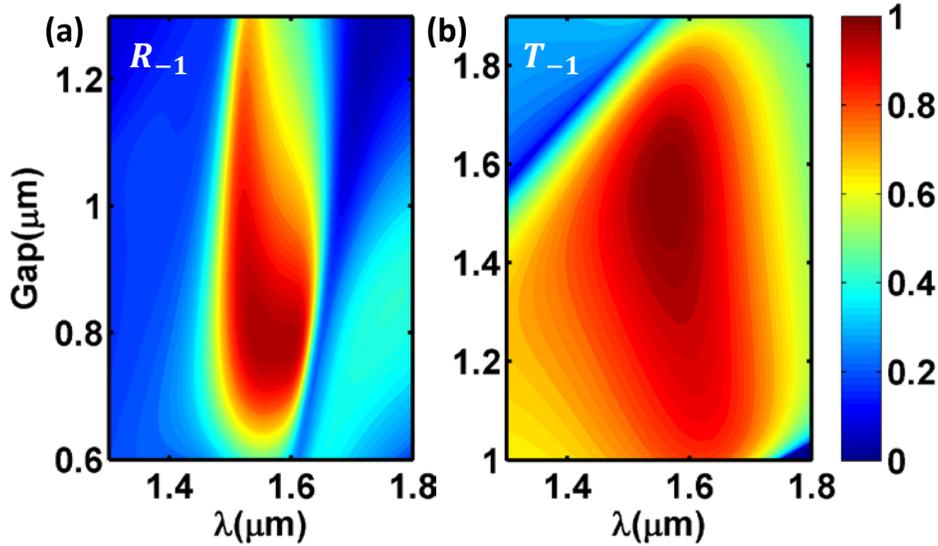
Figure 3.1 (a) R_{-1} spectrum for anomalous reflection with varied low index gap, the grating has bar width $s = 564nm$, thickness $t_g = 340nm$ with 35° incidence angle (b) T_{-1} spectrum for anomalous reflection with varied low index gap, the grating has bar width $s = 164nm$, thickness $t_g = 380nm$ with 30° incidence angle.

This broadband effect is very promising for diffraction tuning applications. For instance, it can be used for beam steering applications [29].). Starting from the minimum allowed period, the metastructure can be stretched by 70% to maintain the anomalous phenomena. Figure 3.2(a) illustrates the reflection and transmission angle change by stretching the metastructure with a given incidence angle and wavelength. By stretching the metastructure, the period gets larger and the reflection and transmission light will rotate towards the normal axis. Such wide variation range can change the angle over 40°. The corresponding amplitude and angles are plotted in Figure 3.2(b).

Accordingly, the wavelength at a fixed perception angle is also controlled by the HCM period in the -1st diffraction order, shown as $\lambda = \Lambda(\sin \theta_i + \sin \theta_o)$. Such property also implies that the color at a fixed observation angle will be changed drastically by deformation with a broadband light source illumination.
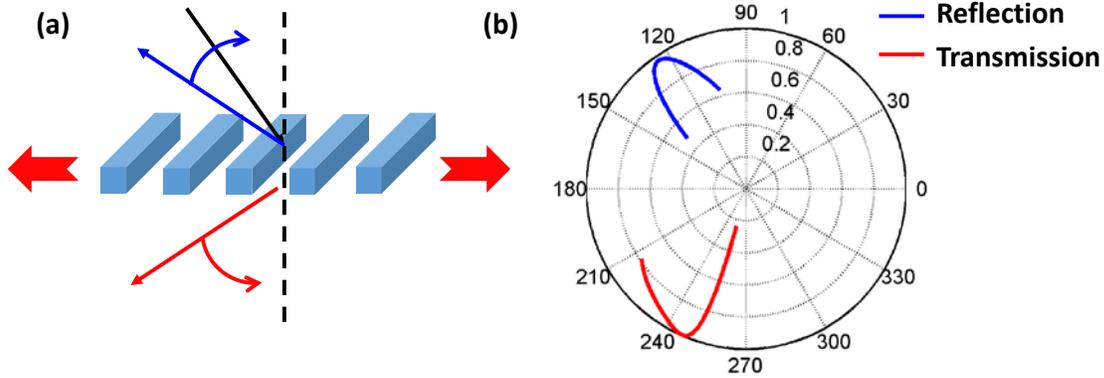
Figure 3.2 (a) Schematic of the reflection and transmission angle rotation with the deformation of the metastructure. (b) The spatial angle and amplitude shift with deformation. The incidence wavelength is 1.55 µm. The incidence angle for reflection design is 35° while it is 30° for the transmission design. The angle axis of the polar plot is modified to fit the angle definition in the calculation.

3.2 HCM Design for Artificial Chameleon Skin

3.2.1 HCM Design for Visible Wavelength

The previous simulation results in section Chapter 3is focusing on the infrared wavelength for silicon HCM structure, where the material is transparent and almost non-dispersive. However, as we are targeting for making the color tunable material, the material loss and dispersion has to be included in the model. In this dissertation, we use the optical constants from reference [58]. By including the material loss, the maximum diffraction efficiency has to be compromised from unity. However, the HCM thickness is typically a fraction of the wavelength. In addition, we are indeed aiming for a broadband effect, which avoids the optical field building up in the HCM structure. Thus, the impact of the material loss can be minimized.

As a demonstration for the primary color sets, the color palette is designed to have a -1st diffraction order enhancement effect for four colors (green 540 nm, yellow 570 nm, orange 590 nm, and red 630 nm) with the same input and output condition. A variety of simulation techniques can be used to calculate the optical spectrum, such as an analytical formulation [20, 38, 40], rigorous coupled wave analysis (RCWA) method [59], finite difference time domain method (FDTD) [46], etc. In this design process, a numerical calculation with the analytical formulation is used for its fastest speed to find the required geometries. Instead of $n_0 = 1$ in the previous simulations, we assume the surrounding low index medium has refractive index $n_{low} = 1.41$, which is typical for polymers.

For a given input and output angle, the geometry of the HCMs is solved to have the strongest -1st diffraction order enhancement. The variables in the design space includes HCM thickness, gap width, bar width and incidence angle. Those variables are be classified by the nature of the fabrication process. The gap width and bar width are defined by the lithography. Very high accuracy can be achieved and the value has large freedom to choose as far as it meets the resolution limit of the lithography. It can also be calibrated to optimum in the actual process. In addition,

38

different dimensions can be incorporated on the lithography step in the same wafer to provide more design flexibility. However, the thickness of the structure is defined by a non-reversible process. It is typically defined by the device layer of a SOI (silicon-on-insulator) wafer. The device layer thickness is determined by the vendor. The thermal oxidation can be performed to thin down the thickness to the target value. However, it cannot be easily varied across the wafer unless the selective area oxidization process is used, which increase the processing complexity and therefore is not favored.

Figure 3.3 shows the simulated R_{-1} value by varying the bar and gap width. In those contour plots, the wavelength is fixed for that targeting color. In the design process, the incidence angle and HCM thickness are swept to create a complete set of such contour plots and the map with the maximum R_{-1} enhancement and geometry tolerance is selected. For each designed color, the dimension can be found to have R_{-1} approaching 90%.
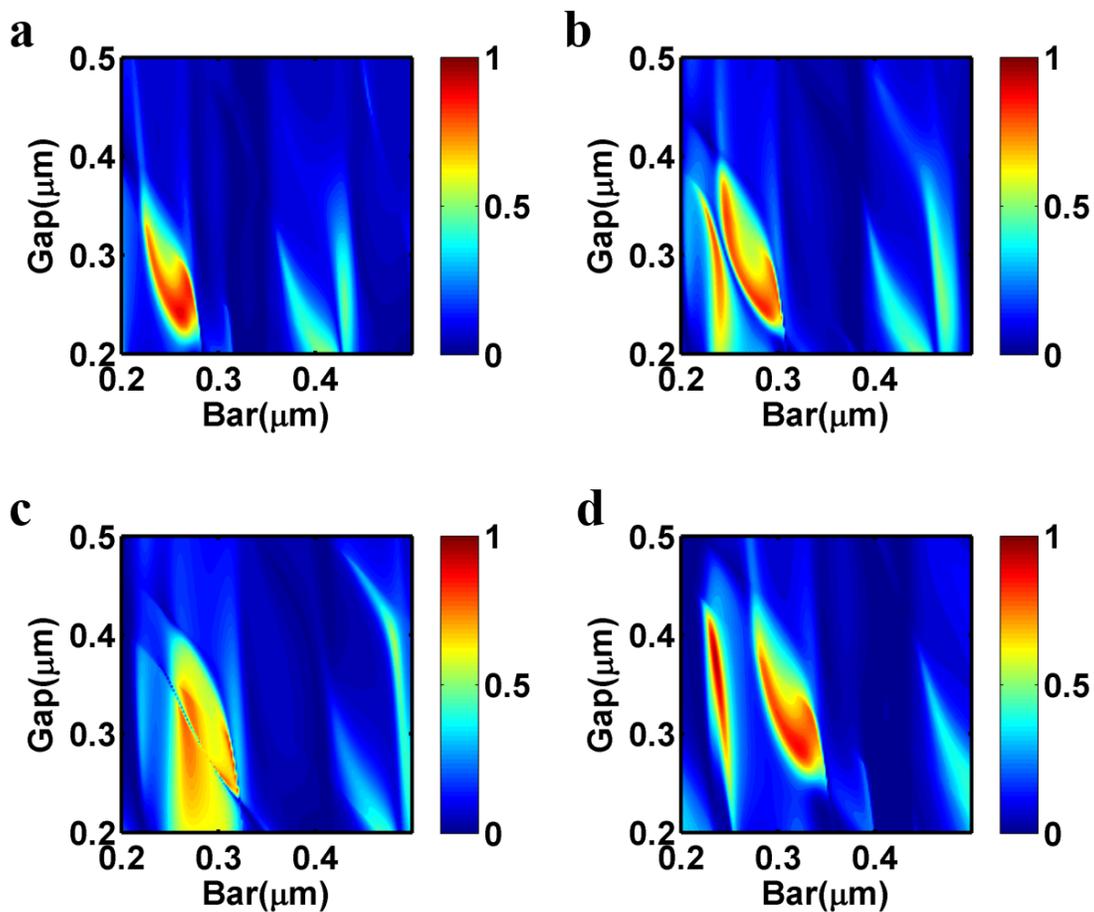
Figure 3.3 The simulated R_{-1} with varied bar and gap width for (a) green (b) yellow (c) orange (d) red designs.

Comparing with the HCM geometries for 1550 nm wavelength, the design tolerance for visible wavelength is smaller, because of the following reasons. First of all, the wavelength at the visible spectra range is about 2 to 3 times smaller than 1550 nm. It naturally scales down the tolerance by

the same factor. In addition, because of the material loss which is denoted by the imaginary part of the permittivity, the real part of the permittivity has strong dispersion from Kramers-Kronig relation [60]. As described in Chapter 2, the anomalous diffraction phenomenon depends on the interference of the eigen-modes in the HCM to create the constructive interference for the anomalous order and the destructive interference for the rest of the orders. The additional dispersion makes it very difficult to satisfy the interference for a broad wavelength range. Despite of those factors, the design map shown in Figure 3.3 gives the geometry tolerance for 10s nm, which is achievable by the UV stepper.

The design for the four color palette is listed in Table 3.1. In order to achieve the anomalous diffraction in the same sample, we choose the designs to share the same incidence angle.

Design	A	B	C	D
Intended Color	Green	Yellow	Orange	Red
Peak R_{-1} Wavelength (nm)	540	570	590	630
Period (nm)	500	532	558	622
Duty Cycle	0.5	0.5	0.5	0.5
Thickness (nm)	180	180	180	220

Table 3.1 The design parameters for the four color palette.

The optical properties of the HCMs from gap width variation are also calculated, as shown in Figure 3.4. High diffraction efficiency in R_{-1} can be achieved in the range around 10% of the period. The received wavelength with the corresponding gap size under the designed angle is marked as the white line in the contour figure. For all of the color designs, R_{-1} has broad enhancement bandwidth in order to shift the colors. For example, the green color (540 nm) can shift to yellow (570 nm) by stretching the gap width from 250 nm to 278 nm while maintaining high diffraction efficiency.
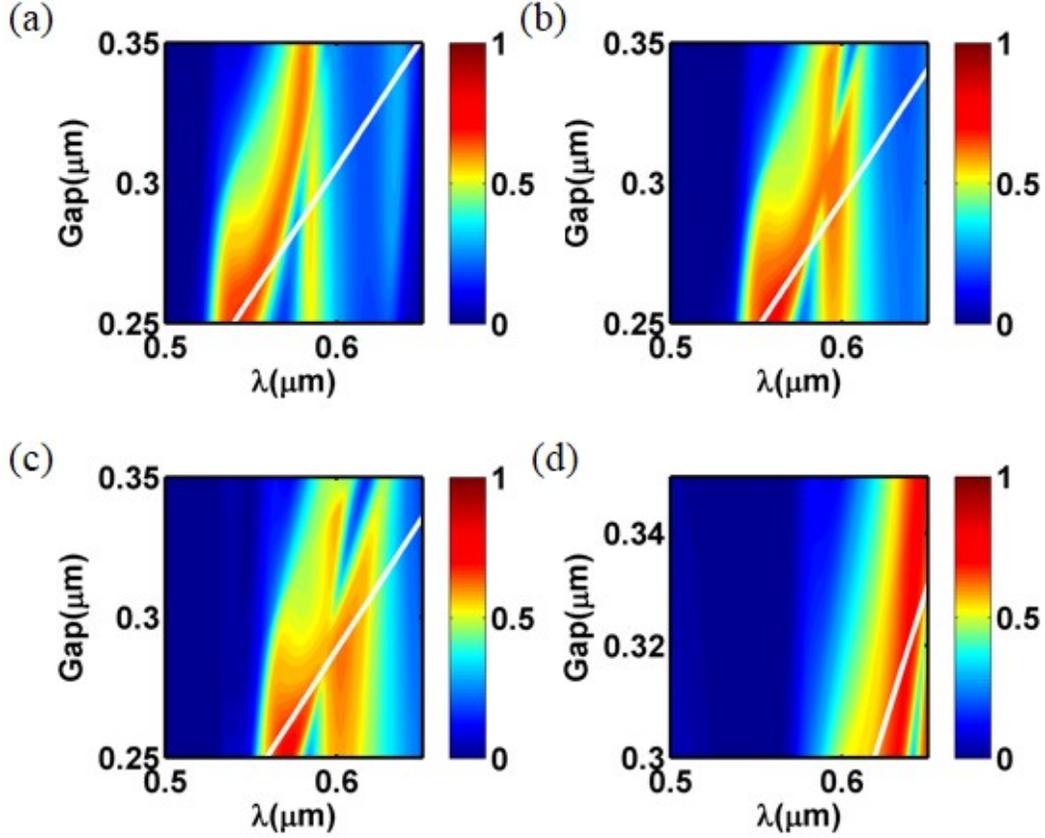
Figure 3.4 The simulated R_{-1} spectra with the deformation of the HCMs in the PDMS membrane for (a) green (b) yellow (c) orange (d) red designs.

3.2.2 HCM Color Rendering under Ambient Illumination

Even though the wavelength of the diffraction light beam from a well-collimated incidence light beam can be easily determined by the grating equation. It is important to understand the color rendering of the HCM under the ambient illumination, which can have any arbitrary spectra and angular component. The mathematical derivation is as following.

We first define a few important variable and functions. The incidence angle is defined as θ and the perception angle is defined as ϕ. The diffraction angle for wavelength λ at m^{th} order is defined as $\alpha(\lambda, m)$. The illumination can be generally defined as $P(\theta)$, which is normalized as:

$$\int_{-\pi/2}^{\pi/2} P(\theta)d\theta = 1$$

3.1

Thus, the perceived light spectrum in the angular range between ϕ to $\phi + d\phi$ is:

$$I(\lambda, \phi)d\phi = \int_{-\pi/2}^{\pi/2} \sum_n P(\theta) R_n(\theta, \lambda)\delta(\alpha(\lambda, m))d\theta \qquad 3.2$$

Here, $\delta(\alpha(\lambda, m))$ is defined as:

$$\delta(\alpha(\lambda, m)) = \begin{cases} 1, & \alpha_n \in [\phi, \phi + d\phi] \\ 0, & others \end{cases} \qquad 3.3$$

In the meanwhile, the diffraction angle α is determined by the grating equation, giving:

$$\sin \alpha(\lambda, m) = \frac{m\lambda}{\Lambda} - \sin \theta \qquad 3.4$$

Therefore, the overall equation for calculating the perceived spectrum is:

$$I(\lambda, \phi)d\phi = (\sum_n \int_{-\pi/2}^{\pi/2} P\left(\sin^{-1}\left(\frac{m\lambda}{\Lambda} - \sin \theta\right)\right) R(\lambda, m)\left(\sin^{-1}\left(\frac{m\lambda}{\Lambda}\right.\right. \qquad 3.5$$
$$\left.\left. - \sin \theta\right), \lambda\right)\left[-\frac{\cos \phi}{\cos \theta}\right] d\theta)d\phi$$

Here, $R(\lambda, m)$ is the diffraction efficiency of the HCM at m^{th} order and wavelength λ. It can be calculated by the analytical solution described in Chapter 2.

By obtaining the spectrum of the perceived light, the color coordinates can be calculated from the color matching functions from CIE 1931 standard. The color matching function and the color space is shown in Figure 3.5.
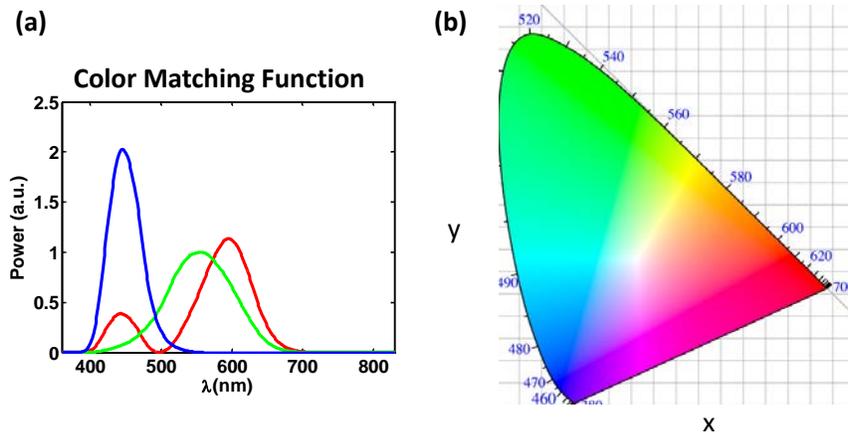
Figure 3.5 (a) Gamut of the CIE RGB primaries and locations of the primaries on the CIE 1931 xy chromatic diagram. (b) The CIE 1931 color matching function.

The color coordinates of the spectrum $I_R(\lambda)$ can be calculated as:

42

$$\begin{cases} X = \int I_R(\lambda)\gamma_r(\lambda)d\lambda \\ Y = \int I_R(\lambda)\gamma_g(\lambda)d\lambda \\ Z = \int I_R(\lambda)\gamma_b(\lambda)d\lambda \end{cases} \qquad 3.6$$

$$\begin{cases} x = \dfrac{X}{X + Y + Z} \\ x = \dfrac{X}{X + Y + Z} \\ z = 1 - x - y \end{cases} \qquad 3.7$$

The entire color design flow chart is summarized in Figure 3.6.

Design HCM Dimension		Complete Diffraction Calculation		Calculate Perception Color under the given illumination
•Sweep the parameter space with the analytical solution		•Simulate the diffraction spectra with a complete incidence angle from 0 to 90º		•Calculate the perceived spectra •Calculate the color with color matching functions
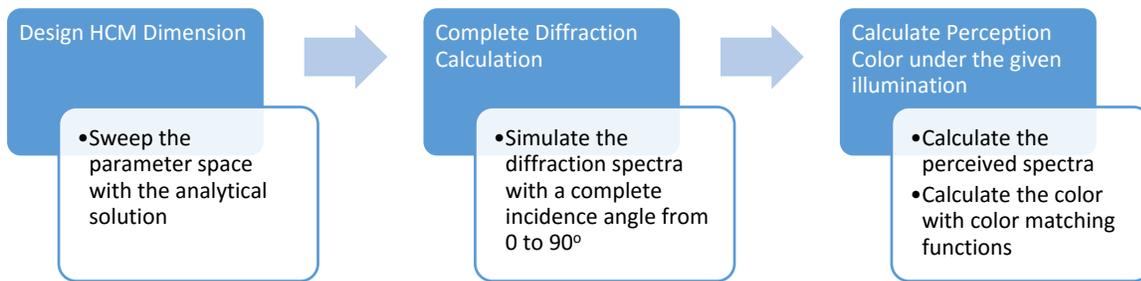
Figure 3.6 Flow chart for the HCM design and color calculation.

3.3 Flexible HCM Fabrication

The HCM designs assume to achieve color tuning based on controlling the width of the low index gap. However, it is not trivial for such control because the HCM is made of solid semiconductors, such as silicon or other IIIV compounds. The microelectromechanical structure seems to be the only option on the rigid substrate. However, the MEMS structure also takes a significant amount of real estate on the chip for the lateral actuation, which also drastically reduce the filling factor. In addition, as the motivation is really to achieve the color control on any arbitrary surface, it is desirable to fabricate the HCM structure in a flexible substrate and enable to color control through the deformation of the substrate. Despite the rigid nature of the semiconductors, they appear to be extremely flexible when the geometries are engineered to be in the sub-micron scale. Therefore, the flexible HCM is a promising approach for achieving the artificial chameleon skin.

In the past decade, the transfer printing method has been developed for achieving the integration of the devices from different substrates onto an alien substrate [14, 15]. This method utilizes a soft stamp as a carrier to remove the elements from a source substrate and deliver to a target surface. In the purpose for flexible HCM, the flexible substrate can serve as the stamp and pick up the HCM structure fabricated on the rigid substrate.
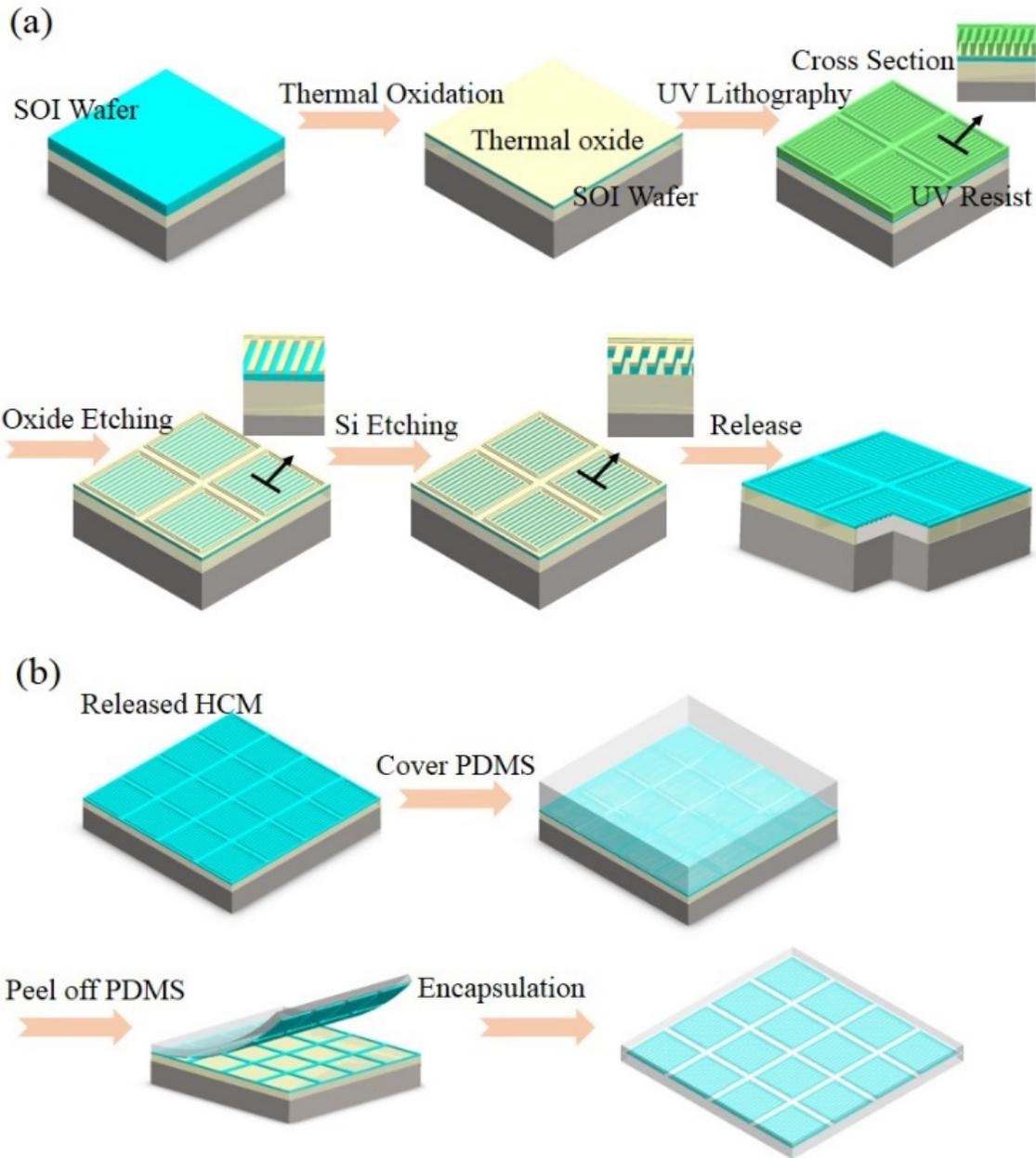
Figure 3.7 The fabrication process for the HCM on the flexible metastructure (a) The nano-fabrication process of the HCM on the SOI substrate (b) The nano-printing transfer process.

The fabrication process for the flexible metastructure consists of two parts. The first part is the fabrication of the HCM on a rigid substrate with nanofabrication techniques, as illustrated in Figure 3.7(a). The process starts from an SOI substrate purchased from SOITEC, with a 220 nm thick silicon device layer and 3 µm thick buried oxide (BOX) SiO_2 layer. In order to achieve precise control of the HCM thickness, thermal oxidation is used to thin down the device layer thickness to the target value. For a 180 nm target thickness, dry oxidation is performed at 1000 °C for 2 hours

and 40 minutes providing a target accuracy within 5 nm. The resulting ~90 nm thick thermal oxide doubles as a dry etching hard mask in the subsequent silicon etching step. The selectivity of SiO_2 is greater than DUV resist for silicon dry etching, and results in a steeper sidewall slope of the HCM.

The DUV lithography is done with an ASML300 DUV stepper. The lithography resolution is 248 nm. The pattern on the DUV resist is then transferred to the SiO2 hard mask by oxide dry etching. The DUV resist is stripped before the silicon etching step. A transformer coupled plasma (TCP) process is used to etch the silicon with the oxide hard mask.

In the last step, the HCM structure is released with HF vapor. In order to facilitate the transfer process with high uniformity, a folded beam structure is used to hold the HCM pixel after the undercut etch, as shown in Figure 3.8. The HCM bars are connected to a 1 µm wide pixel frame and the four folded beams with 250 nm by 250 nm cross-sectional dimension and 96 µm length connect the pixel frame to the streets between the pixels. Because the mechanical strength of the folded beam is much weaker than the pixel frame, the stamp transfer process breaks the beams and maintain the HCM pixels intact.
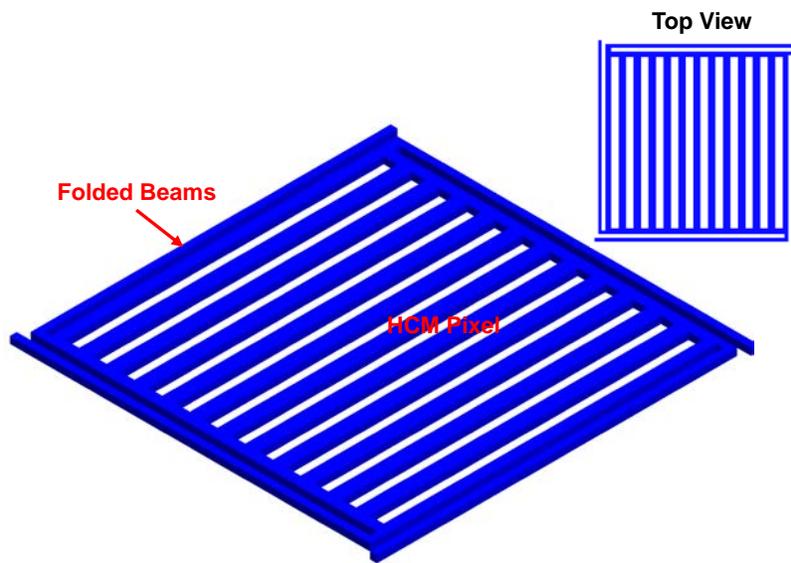
Figure 3.8 The schematic of the HCM pixel with the folded beam structure

An etching rate of ~18 nm/min keeps the HCM suspended with support from folded beams. The release time is controlled to ensure the HCM is released but the large frame is still connected to the substrate with the BOX. The etch rate needs to be low enough to make sure the carrier gas (ethanol), can carry away the moisture, that is generated as the byproduct of the chemical reaction. Avoiding the accumulation of the moisture is important for this undercut etching process. The water accumulated between the HCM and the substrate creates surface tension and pulls the HCM onto the substrate. By the HCM and the substrate touching each other, strong adhesion can be created through the van de Waals force. It can create failure for the transfer process.

The transfer printing process is shown in Figure 3.7(b). The polydimethylsiloxane (PDMS) stamp-based process is used to pick up the HCMs from the SOI substrate. The PDMS stamp is made of SYLGARD 184 silicone elastomer. A 10:1 mixing ratio between the base and the curing agent is used in this process. The base:agent mixing ratio can be adjusted for the specific mechanical property requirement of the PDMS membrane. Generally, larger mixing ratio will give smaller Young's modulus for the cured PDMS [61]. After mixing the base and the curing agent, air bubbles are created. They can be removed by applying a vacuum step to the mixture. The stamp is then solidified by baking the mixture at 75 °C for 1 hour.

The thickness of the PDMS stamp can vary depending on the applications, it can range from 10s nm to as thick as needed. However, to use the PDMS stamp for large area transfer printing process, the thickness is desired to be thicker than 10 µm. The mechanical strength will be too weak otherwise to support the process handling in large area, for instance 1 cm by 1 cm. However, thinner PDMS films, such as 100s nm thick film, are commonly used for the micro-device applications [62].
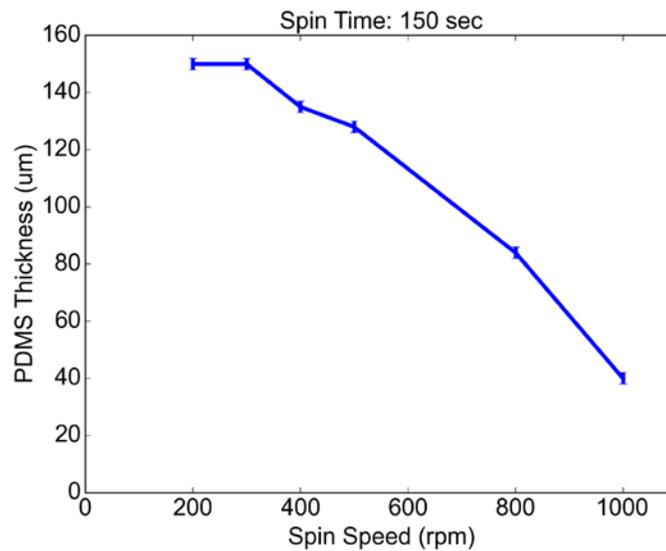
Figure 3.9 PDMS spin coating thickness with varied spin speed. The spin time is fixed at 150 seconds.

The PDMS stamps above 200 µm can be made simply by pour the PDMS mixture into the petri dish, as more than 1 ml PDMS is needed and can be easily measured. The thickness can be controlled by its volume divided by the surface area of the petri dish. On the other hand, the thinner PDMS film requires to use the spin coating process to achieve good uniformity, with the thickness being controlled by the spin speed and time. Typically, the PDMS is spin coated and cured on a silicon wafer. The PDMS has considerable amount of adhesion to the silicon surface after curing and the film below 100 µm thick is very difficult to be peeled off without breaking. Therefore, the silicon wafer needs to be first salinized by trichlorosilane (tridecafluoro-1,1,2,2,-tetrahydrooctyl - 1-trichlorosilane). This step is done by seal the silicon wafer and one droplet of trichlorosilane in a vacuum chamber for at least 1 hour. The PDMS thickness from spin coating is plotted in Figure 3.9.

46

To pick up the HCMs from the SOI substrate, the PDMS stamp uniformly covers the surface of the SOI chip. . In order to achieve high transfer yield (minimizing defective pixels), each individual HCM pixel needs to have good adhesion with the PDMS stamp. Small air bubbles can easily form between the stamp and the SOI chip surface, especially for thin PDMS stamps, making the transfer challenging for large sample sizes. This yield issue is solved by performing a second vacuum step. The SOI chip is fixed on the glass slide with double-sided scotch tape. Next, a PDMS stamp seals the perimeter of the SOI chip with an air film isolating the PDMS stamp from the SOI chip surface. The assembly is then put into a vacuum chamber. The pressure within the air film will be much lower than atmospheric pressure. Finally, by rapidly venting the vacuum chamber, the atmospheric pressure uniformly presses the PDMS stamp to the chip surface providing excellent contact between each individual HCM pixel and the stamp. Because the HCM pixel is connected to the substrate with very weak folded beams, peeling off the stamp from the substrate will easily break the beams without affecting the HCM structures. Finally, the HCMs on the stamp are encapsulated by a thin PDMS layer by repeating the PDMS stamp preparation process.

(a) **(b)**
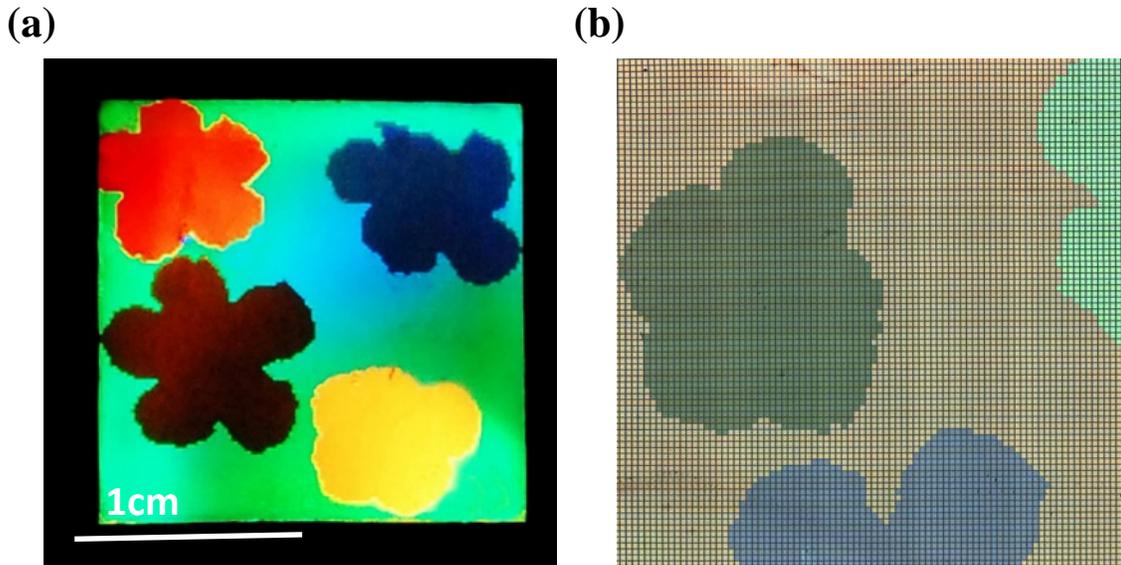
Figure 3.10 (a) Photograph of a flexible HCM sample with flower patterns. (b) Microscopic photograph of the flower pattern sample.

A flower sample is fabricated to have five different colors, including blue, yellow, orange, dark red and green, as shown in Figure 3.10(a). The size of this sample is 16 mm by 16 mm, consisting 25600 HCM pixels. The inspection under the microscope shows no bad pixels within this sample (shown in Figure 3.10(b)), indicating extremely high process uniformity.

(a) **(b)**

100 µm long
250 nm wide

10 µm

2µm
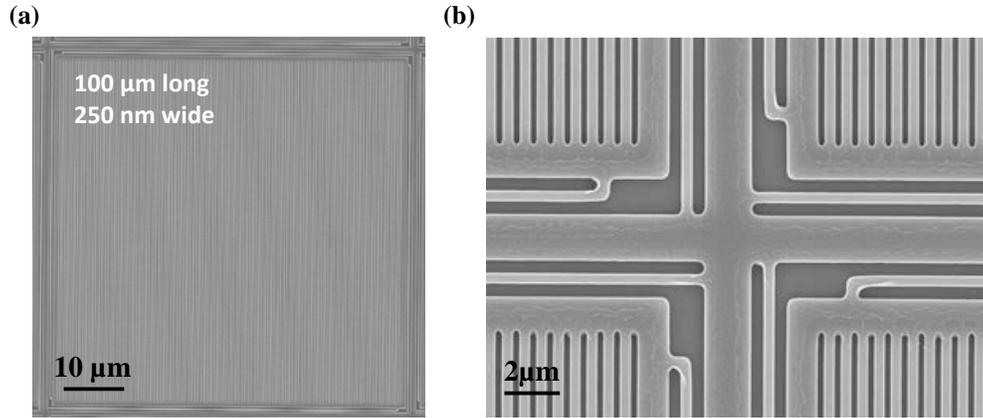
Figure 3.11 SEM image of (a) a pixel of the HCM (b) zoom-in of the folded beams
for HCM on SOI substrate.

The SEM image of one HCM pixel is shown in Figure 3.11(a). The size of the pixel is 100 µm by 100 µm. This value is arbitrarily determined to reduce the process complexity. As discussed in chapter 2, the HCM can hold the same property with reducing its size down to a few times of the wavelength, which is less than 5 µm for the visible light application. However, because the streets between the pixels and the folded beams are required to improve the transfer uniformity, as shown in Figure 3.11(b), the size of the pixel impacts the filling factor for the HCM display. By setting the folded beam width and the spacing to the stepper resolution limit, and the street with to 1.25 µm, the filling factor of the 100 µm size pixel is 95% while it is reduced to 52% with 10 µm pixel size. The cross section of the HCM bars is shown in Figure 3.12(a). The SiO_2 hard mask helps to reduce the sidewall slop down to 4°, which is typically 9° with resist as the etching mask. After the HCM structures are transferred to the PDMS substrate, the bars are still aligned to its original spatial periodicity, as shown in Figure 3.12(b).

(a) **(b)**

100nm

200nm
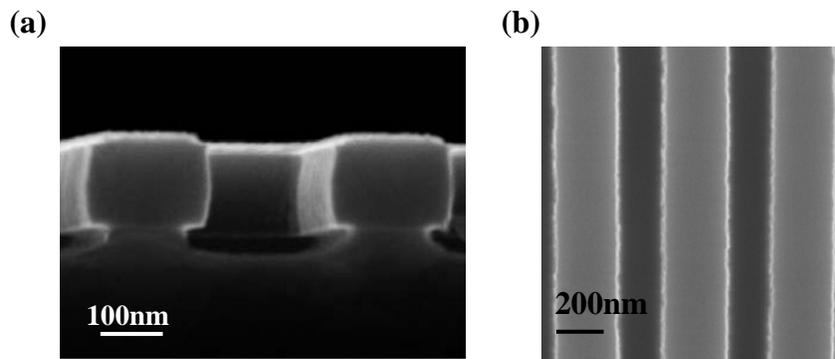
Figure 3.12 (a) Cross-section SEM image of the HCM bars (b) SEM image for the
HCM bars on PDMS substrate

3.4 Flexible HCM Diffraction Characterization

In addition to the vivid color achieved by the sample shown in Figure 3.10(a), the quantitative characterization is also performed to evaluate the diffraction efficiency of the flexible HCM. Because of the lack of broadband tunable laser at the visible wavelength, we measured the absolute value of the diffraction efficiency with a green laser at 532 nm wavelength. The beam steering effect is also measured with the same setup by tracing the diffracted beam under the different flexible HCM deformation. The diffraction spectrum is also measured with a white light illumination by a visible light spectrometer. However, because the measurement setup involves a number of coupling loss that is difficult to be quantified, the measured spectrum is in arbitrary units.

3.4.1 Characterization with Laser Beam

The schematic for the diffraction efficiency characterization setup are shown in Figure 3.13. The fiber coupled laser source illuminates the sample through a collimator. A free space polarizer is used to attain TE polarization. The collimator provides 0.39 mm output waist diameter and 1.75 mrad divergence angle. The diffracted light is measured with a photodetector. The collimator and the detector are fixed on the rotational arms and aligned to have the rotation center at the spot where the sample is illuminated. The reflected power from the gold mirror is measured as the reference where the reflectivity is obtained from the mirror specification. This setup is also used for the beam steering measurement. The sample can be stretched by the clamps and the deformation can be measured with micrometers. The angular response and the beam size are measured by the photodetector with a pin hole.
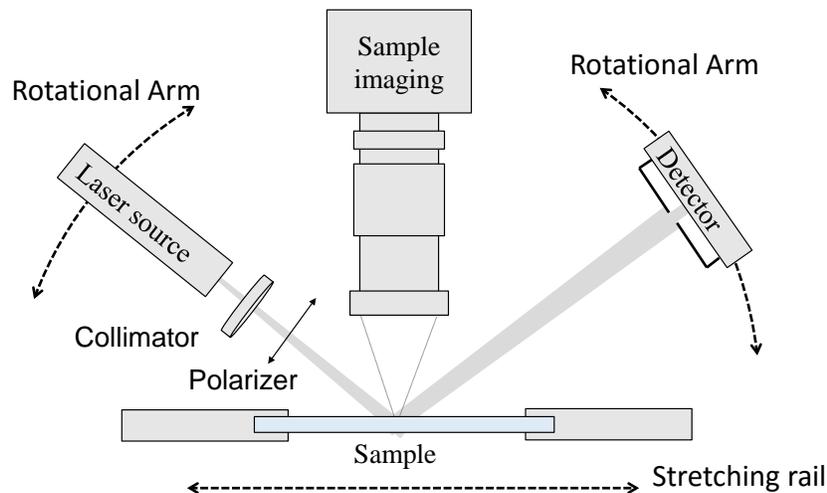
Figure 3.13 The setup schematic for the diffraction efficiency measurement with the laser source. It is also used for the beam steering measurement with green laser light incidence.

The photograph of the measurement setup is shown in Figure 3.14. The sample is clamped on the stage controlled by the micrometer. The deformation of the sample can be controlled with a

resolution down to 5 µm. A CCD camera is mounted on top of the sample with magnifier to observe the deformation of the pixels.
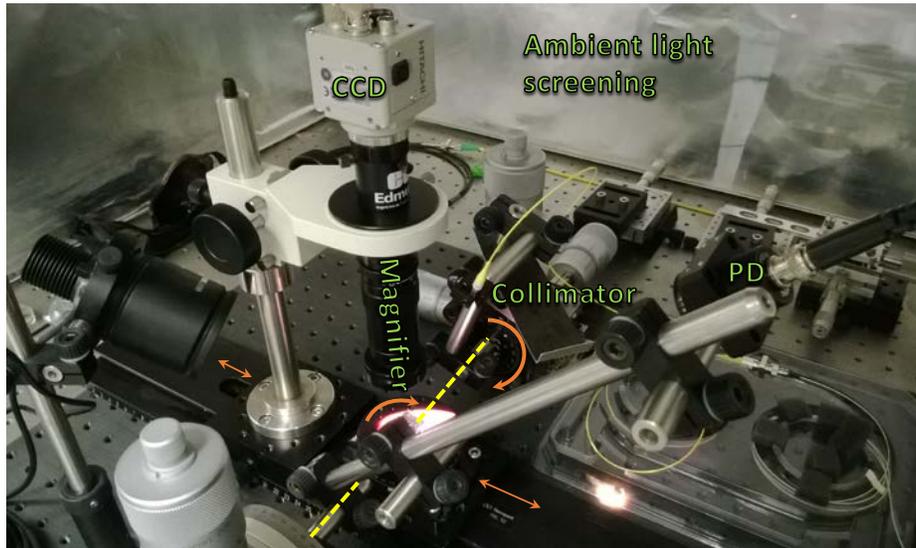
Figure 3.14 The photograph of the characterization setup.

The HCM with design A in Table 3.1 is measured. Figure 3.15 shows R_{-1} and R_0 as a function of the incidence angle. As high as 83% diffraction efficiency in R_{-1} is obtained, 15.4 times stronger than the power in R_0. The simulation prediction for R_{-1} value at 532 nm is 88.3%. The measured value is slightly lower, mainly attributed to the non-vertical and rough sidewall of the HCM. These can be improved with various methods, such as UV resist reflow and through the use of a hard mask with better selectivity, such as Al_2O_3 and Si_3N_4.
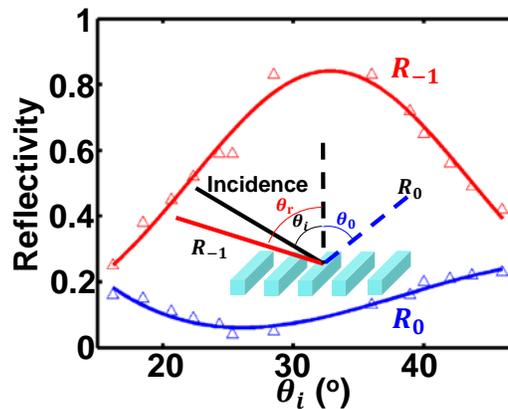
Figure 3.15 The reflectivity dependence on the incidence angle for the green HCM design measured with a 532 nm green laser.

The diffraction angle of the output light beam can be controlled by stretching the flexible HCM membrane. This effect is illustrated in the simulation result in Figure 3.2. In the experimental

50

demonstration, we stretch the HCM membrane with design A for $\epsilon = 5.4\%$ deformation (defined as $\epsilon = \frac{\Delta L}{L}$). A 5.5° irradiation angle is steered with the diffraction efficiency maintaining in the 3dB range. The full width half maximum (FWHM) is unchanged at 0.3°. This effect represents more than 36 resolvable, making the flexible HCM as an excellent candidate for the beam steering applications.
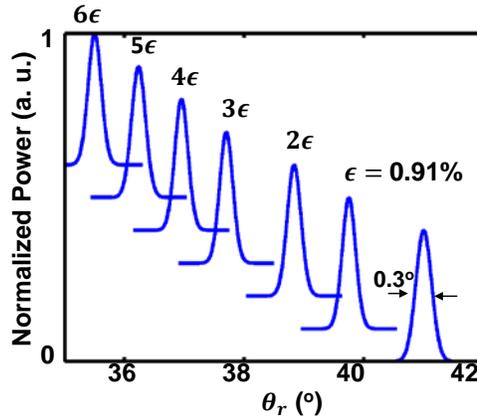
Figure 3.16 The beam steering effect characterization within a 3 dB optical power range. The flexible membrane is illuminated by a green laser. The irradiation angle of R_{-1} is steered with the stretching of the membrane.

3.4.2 Characterization with White Light Illumination
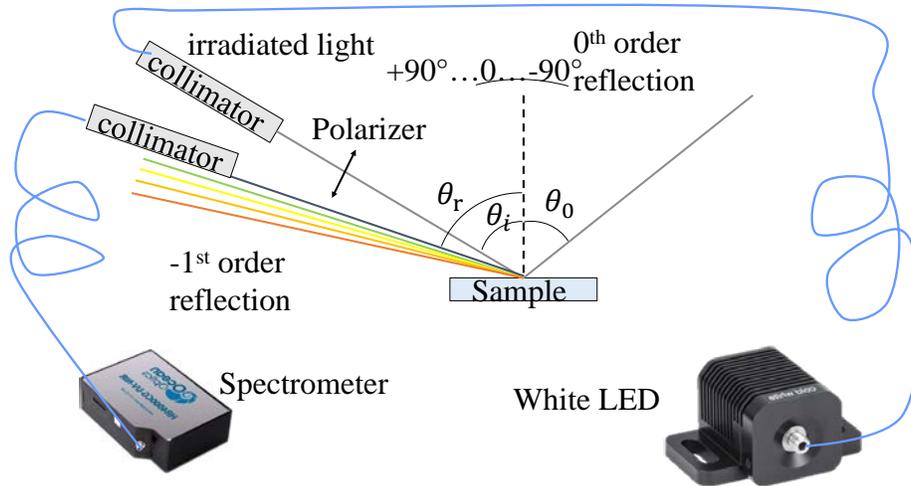
Figure 3.17 The setup schematic for the diffraction spectrum measurement with the white light.

51

For color display applications, it is important to measure the diffraction characteristics over the entire visible spectrum. The diffraction spectra of the HCMs are measured with white light illumination, as shown in Figure 3.17. The white light from the fiber coupled LED source is collimated to form an output beam with 0.8mm diameter and 0.049° divergence angle. The color of the diffracted light is spatially split at the -1st order. In order to measure the angular distribution of the spectra, another collimator is used to couple the diffraction light in the free space to the optical fiber, which is connected to the visible light spectrometer (Ocean Optics HR4000). By performing the integral of the spectrum over the spatial angle for each order, the diffraction spectrum as shown in Figure 3.19 are measured. The dispersion of the measurement system is ruled out by using the gold mirror reflection measurement as reference.
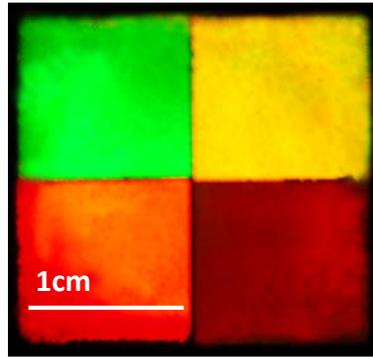
Figure 3.18 The photograph of the four colors (green, yellow, orange, and red) as the color palette under the white light illumination.

The color palette with the HCM designs in Table 3.1 is fabricated. It is a 2 cm by 2 cm sample, consisting 40,000 HCM pixels. Figure 3.19(a) shows the diffraction spectra of both R_0 and R_{-1} for HCM design C, targeting for strong enhancement at orange color (590 nm). The measured spectra shows strong enhancement for R_{-1} and suppression for R_0 at wavelength beyond 540nm. The simulation results of the diffraction spectrum for this HCM design are also plotted as a comparison. An excellent agreement is achieved between the measurement and the theoretical prediction. The same measurements are also performed on the flexible HCM membranes with design A, B and D. The strong enhancement peaks are demonstrated for the green, yellow and red designs as well.

Under white light illumination, the color of the sample can be tuned by stretching. The resulting deformation varies the low index gap size and therefore changes the periodicity of the metastructure. Under a fixed input and output angle, the control of the HCM period leads to the control of the perceived color. The quantitative measurement of the wavelength shift on the design A HCM is shown in Figure 3.20. The diffraction wavelength is 541 nm at the relaxed state ($\epsilon = 0$). By providing $\epsilon = 5\%$ deformation, the perceived wavelength is shifted to 580 nm. It leads the display color to be changed from green to orange, while the optical power still remains within 3 dB. The photograph of the sample under the relaxed and deformed states are shown in Figure 3.20(b).
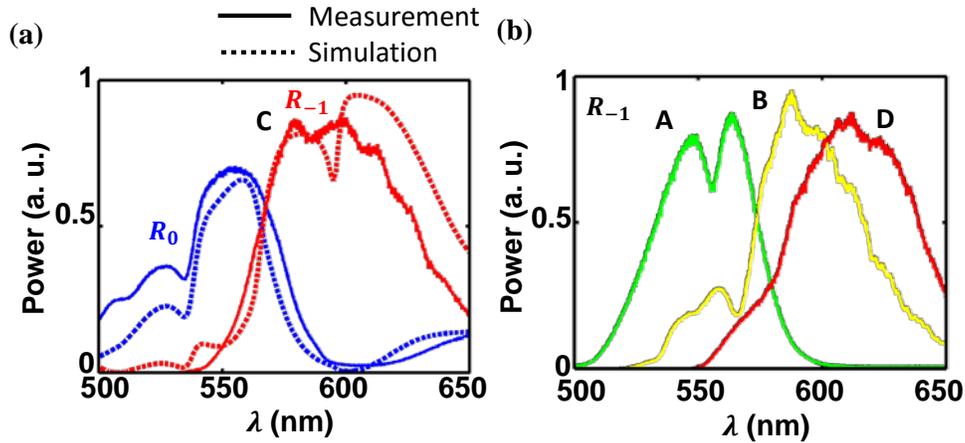
Figure 3.19 The normalized spectra of the measurement (solid lines) and simulation (dashed lines) results for Design C. The red and blue curves represent the -1st order and 0th order, respectively.
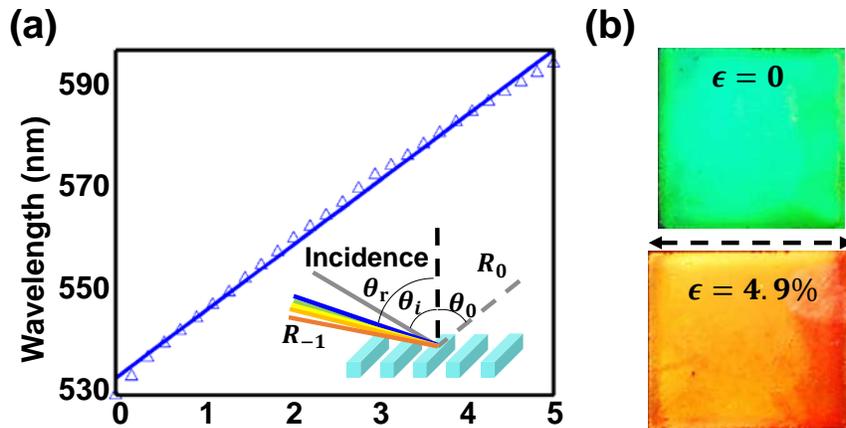
Figure 3.20 (a) The color control effect characterization for the green HCM design in 3 dB peak power range. The spectrum is measured at the fixed incidence and perception angle. By stretching the flexible membrane, the peak shifts to longer wavelengths. (b) The photographs of the sample before (ϵ=0) and after (ϵ=4.9%) stretching.

However, the diffraction efficiency tends to decrease as the low index gap increases, Figure 3.4. The sample contraction in the direction perpendicular to the stretching can also cause the efficiency to drop when $\epsilon > 10\%$ from observation. This effect can be optimized by using a two dimensional grating structure. The color at the relaxed state shows excellent uniformity due to the uniform fabrication cross the large sample. Less than 10nm wavelength variation is observed after stretching, which is mainly due to non-uniform applied force from the current setup and the imperfection from the PDMS polymerization step for sample encapsulation. Figure 3.21 shows the color changes of different designs can be simultaneously achieved. This measured result

53

demonstrates that the displayed color is very sensitive to deformation, making it an excellent candidate for the sensing applications.

$\epsilon = 0$ $\epsilon = 2\%$ $\epsilon = 4\%$

$\epsilon = 6\%$ $\epsilon = 8\%$ $\epsilon = 10\%$
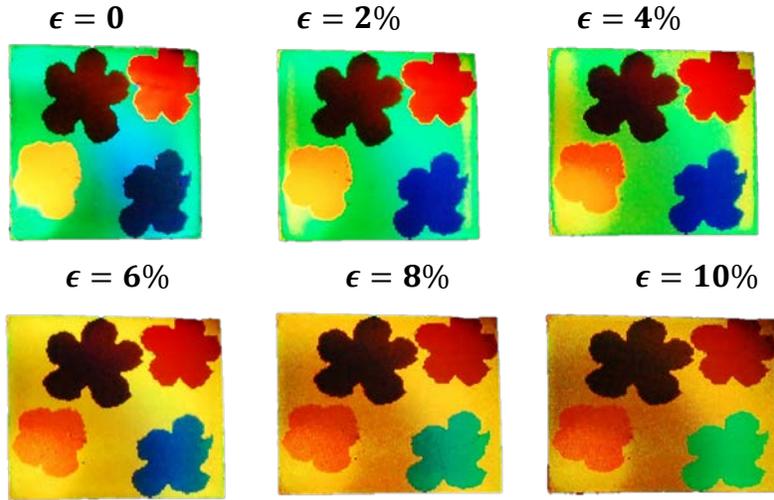
Figure 3.21 Photos of the flower pattern under deformation from 0 to 10%.

3.5 Flexible HCM for Display and Camouflage

The flower and color palette designs are aiming for optimizing the diffraction efficiency in the -1st order. In the dual order diffraction regime, the observation configuration has oblique angle incidence and the -1st diffraction order is at the same side as the incidence light, as respect to the vertical axis. However, the oblique angle observation is not desirable. It is much easier for a person to find the surface normal angle instead of an arbitrary oblique angle. Therefore, the surface normal configuration can is more convenient for bare eye observation. In addition, the display can also be configured with other optics, such as projection lens, etc. The optics design can be much more simplified with the display in the plane that is perpendicular to the optical axis, because the entire display has the same distance to the focal plane and share the same focus condition.

However, in the surface normal configuration, there exists at least three diffraction orders, including 0th, -1st and -2nd, to make -1st aligned to the vertical axis. This can be proved mathematically as following. The incidence angle θ_i is

$$\sin \theta_i = \frac{\lambda}{\Lambda} < 1, as\ \theta_{-1} = 0 \qquad 3.8$$

Therefore, the diffraction angle for -2nd order is a real value:

$$\Lambda(\sin \theta_i + \sin \theta_{-2}) = 2\lambda \rightarrow \sin \theta_{-2} = \frac{\lambda}{\Lambda} < 1 \qquad 3.9$$

Because of the additional diffraction order, the diffraction enhancement at the -1st needs to design the interference to achieve constructive interference at R_{-1} for the reflection type, while

suppressing the rest of the 5 diffraction orders. The extra constrain makes the design tolerance much smaller.

However, the requirement for the bandwidth and the diffraction efficiency really depends on the specific applications. For applications focusing on the color rendering instead of the power, the most important consideration is the color characteristics and its sensitivity to the structure variation. The requirement for the diffraction efficiency can be relatively relaxed.

The HCM designs are found in the following strategy. We choose the thickness to be 200 nm so we can start with the 220 nm SOI wafer with a good thermal SiO_2 hard mask thickness. When calculating the diffraction spectrum, the HCM period needs to be associated with the wavelength in order to guarantee the R_{-1} is in the surface normal direction. The duty cycle is swept for the optimum efficiency. The contour map for the designs is shown in Figure 3.22. The region between the two white lines are the parameter space that can work with current processing limits. The regions outside the white lines either have bar width or gap width less than 250nm, being intestinally set as dark blue in the contour plot.
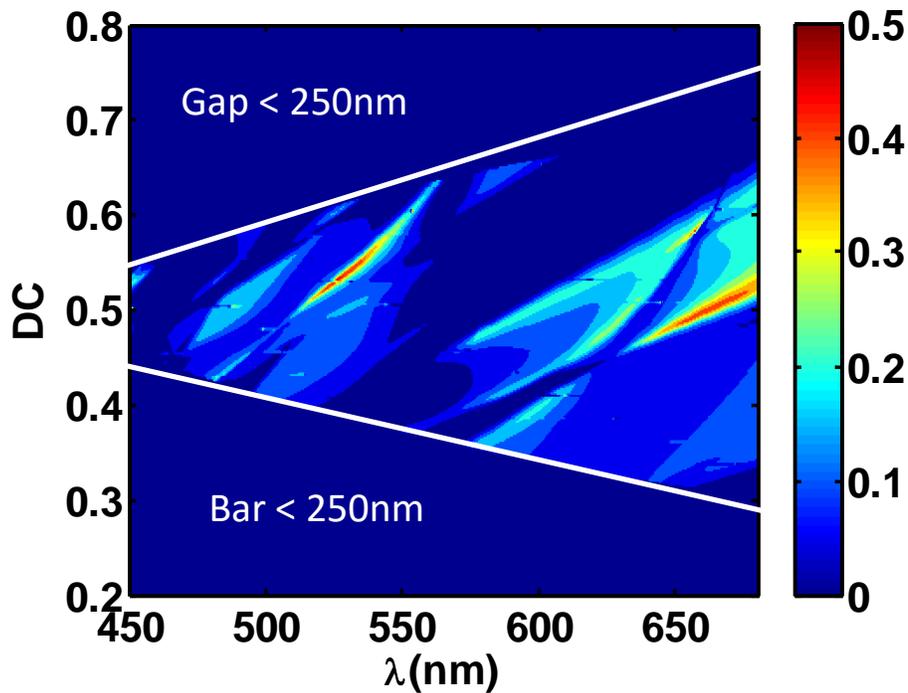
Figure 3.22 Diffraction efficiency spectra for R_{-1} with varied duty cycle.

Nine different color HCM designs for the color ranging from blue to red are listed in Table 3.2. The design constrain from the UV stepper is applied to make sure the minimum linewidth is greater than 250 nm. The display configuration is designed to have the incidence light from 50° as respect to the surface normal incidence and view at the normal direction.

55

Design #	Color	Bar (nm)	Gap (nm)	DC	Period(nm)
1	460nm	303	258	0.54	561
2	480nm	336	250	0.57	586
3	500nm	281	330	0.46	610
4	520nm	317	317	0.5	635
5	560nm	424	260	0.62	684
6	580nm	462	250	0.65	708
7	600nm	477	255	0.62	732
8	620nm	507	250	0.67	756
9	640nm	414	367	0.53	781

Table 3.2 The design chart for the surface normal HCM design.

The corresponding color of the designs are calculated under varied deformation. Under relaxed state, the designs cover the primary color set, including blue, cyan, green, yellow, orange, red, etc. The color map is shown in Figure 3.23. Under 10% deformation, the primary color set all have large color tuning range. The blue color shifts to green; the green design shifts to yellow and the red design shifts to dark red. Based on the full color set, complex display samples can be designed.
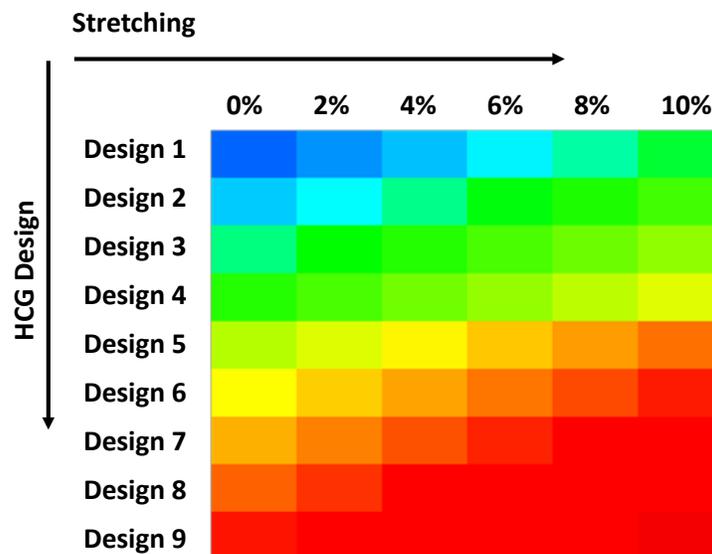
Figure 3.23 The color map for the HCM designs under the deformation from 0 to 10%.

(a)

(b)
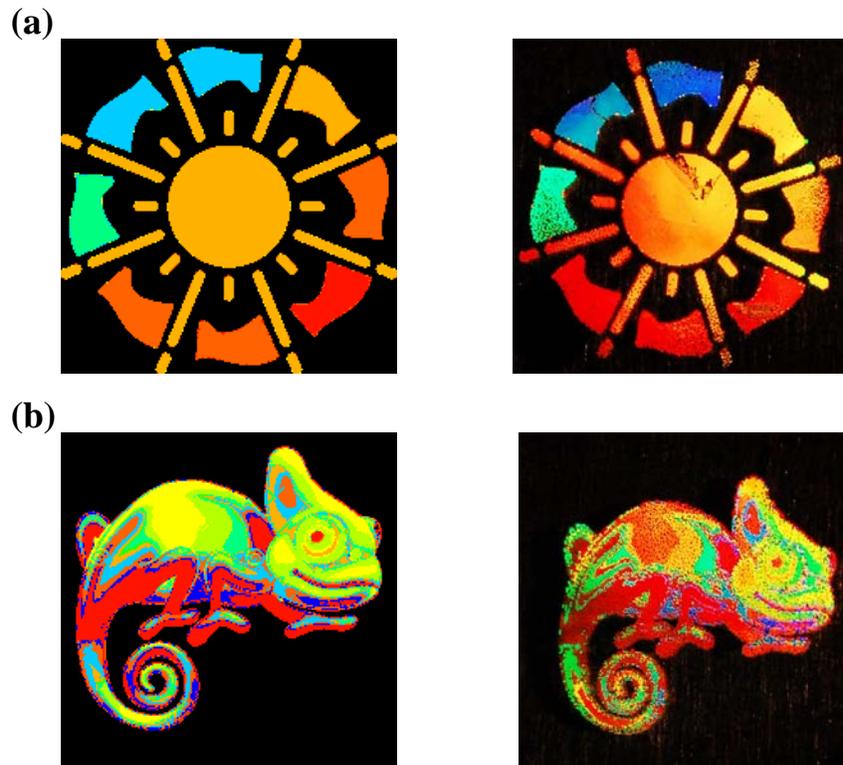
Figure 3.24 (a) IYL logo design (top left) and the photograph of the HCM sample (top right). (b) Chameleon pattern design (bottom left) and the photograph of the HCM sample (bottom right).

Figure 3.24 shows two display designs. As 2015 is the international year of light (IYL) to celebrate 150th anniversary of the Maxwell's equation, we replicate the IYL logo with the HCM designs. We also choose a chameleon pattern to demonstrate the HCM display for more complex patterns. The sample size is 2 cm by 2 cm. The excellent agreement between the design and the real sample is achieved.

In Figure 3.23, we notice that two different HCM designs can have almost the same color when the diffracted light wavelengths of such two HCMs are within the bandwidth of the corresponding color. For instance, as Design 5 and 6 both being stretched for 2%, they both become orange. In addition, for Design 7, 8 and 9, > 6% deformation makes them all dark red. However, human eyes are much more sensitive than the theoretical model. It is extremely difficult to achieve the camouflage under the pure color approach.

Inspired by the military camouflage clothing, we choose to use the color lumps to achieve the camouflage effect. Instead of trying to match the front and background colors, we try to match the color pattern with stretching the flexible HCM display. Even though the color can be still different under the bare eye, the image can be hidden in the background as soon as they have the same color lump pattern. This effect is shown in Figure 3.25.
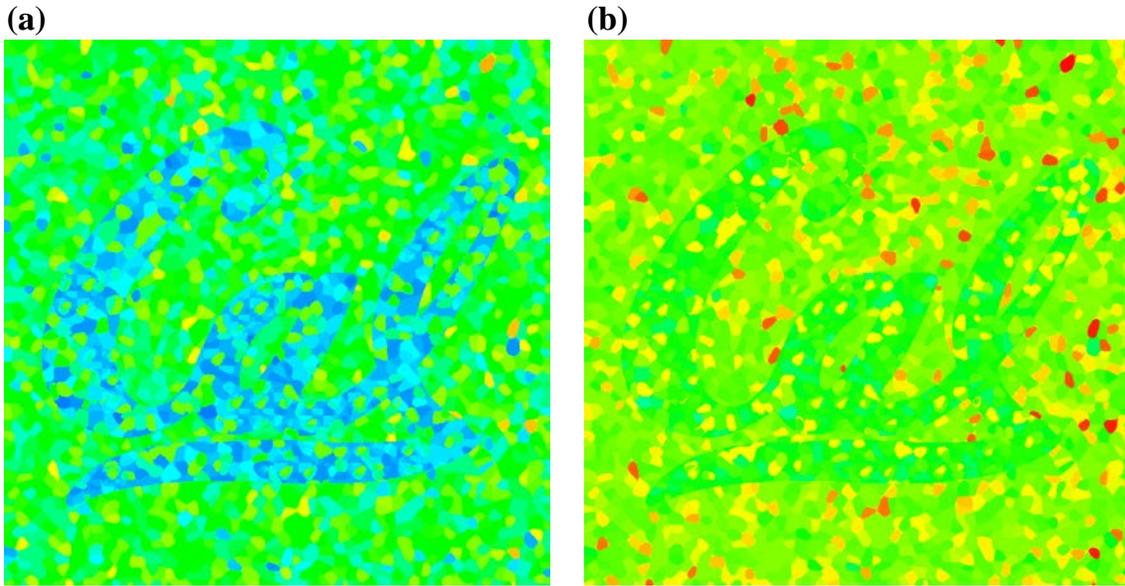
Figure 3.25 (a) The CAL logo image at the relaxed state. (b) The display under 7% deformation.

3.6 Summary

In this chapter, we describe a completely new phenomenon for a planar periodic diffractive structure which exhibits anomalous reflection and refraction. We demonstrate the first flexible semiconductor metastructure and use it for active coloration. Excellent figures of merit and agreement with theoretical predictions have been achieved with the chosen implementation. Greater than 99.9% process yield is achieved for macroscale samples, making this approach very suitable for large volume production. With the flexibility of a PDMS membrane, an HCM can be coated on the surface of objects, making a color display sensitive to geometrical change. Based on the large amount of reports about regarding PDMS for MEMS applications, we expect excellent repeatability for a large number of stretching cycles. The minimum requirement for a single-pixel HCM is two periods, which can transcend state-of-the-art displays below single micron resolution. The results presented here provide an illustration of the opportunities available for utilizing HCMs in flexible optics applications, ranging from camouflage and the visual arts at the macroscale, down to bio-labeling and imaging at the microscale.

Chapter 4

Flexible HCM VCSEL

4.1 Short Cavity HCM VCSEL

4.1.1 VCSEL without DBR

Vertical Cavity Surface Emitting Lasers (VCSELs) are a very promising low cost and low power consumption laser source for metro area access networks, PON applications, active optical cables and other datacom links [63-66]. In particular, VCSELs emitting in the 1.3~1.6 um wavelength range are of interests for longer range wavelength-division-multiplexed (WDM) and optical interconnects [67-69]. Silicon transparency of long wavelength VCSEL makes it an ideal light source silicon photonic circuit [70]. Additionally it is desirable to have wavelength tunable VCSELs for WDM-PON and datacenter applications [71]. By electrostatically actuating the high contrast grating (HCG) mirror, the depth of air gap between the HCG and the rest of the structure will be varied, thus different lasing wavelengths could be attained by varying the cavity length.

The tunable VCSELs reported before have limited wavelength tuning ranges [23]. This is due to the use of either one or two distributed Bragg reflectors (DBRs), comprising of alternating layers of materials with a low index contrast. The DBR makes the VCSEL cavity having a relatively long effective length, and thus limits its tuning range. This will be even more challenging for 1.55 um HCG VCSELs on an InP platform where the DBRs have even smaller index contrast [72]. Therefore, a DBR reflector based on the InP materials system requires at least 45 pars of DBR pairs to achieve > 99.5% reflectivity. That makes the full epitaxy wafer structure easily go beyond 200 layers, making the growth very expensive. Additionally, integrating such a thick VCSEL structure onto silicon is difficult, because 1) very thick epi-structure induces bowing, strain and defects which reduces the yield of III-V to silicon bonding, 2) very thick epi-structure will also prevent conducting the dissipated heat out of the active region effectively.

In addition, reducing the cavity length of the VCSEL can bring many important benefits for the laser performance. First of all, shorter cavity means larger confinement factor between the quantum well and the cavity standing wave. It can reduce the threshold current and improve the VCSEL power efficiency. This effect is opposite to the edge emitting lasers. The intuitive difference between the VCSEL and the edge emitting laser is that the gain in VCSEL is determined by the quantum well thickness and independent from the cavity thickness. Therefore, reducing the cavity length leads to less material loss in the region outside the quantum well. As a consequence, the gain required to reach the threshold is reduced.

For the tunable VCSEL, the tunability, which is defined as the ratio between the wavelength shift over the cavity length change, noting as $\eta = \Delta\lambda/\Delta L$. The tunable VCSEL that consists one HCM mirror and one DBR mirror reported in [28] has tunability around 4%. That means 25 nm mirror displacement needs to be created for 1 nm wavelength shift. By reducing the cavity length to 4

standing wave peaks, the tunability can be increased to 25%. For a MEMS actuated tunable VCSEL, higher tunability means stronger spring can be used under the same tuning voltage, providing faster MEMS response and smaller Brownian motion.

As describe in Chapter 2, the HCM has been adopted to replace to top VCSEL mirror [22, 23, 28, 72]. The thickness of the HCM mirror is only a fraction of the wavelength, which is 50 times thinner than the DBR. It reduces the cavity length by two folds and the mirror mass by 100 times. Therefore, the tunability and the tuning speed are greatly improved. To make a VCSEL with the ultimately short cavity length, both DBR mirror needs to be replaced. In principle, the cavity length can be reduced to a half of the wavelength. However, as the HCM mirror requires to be fully surrounded by the low index medium, there exists an index transition from the low index gap to the active region. Thus, two additional standing wave peaks need to be added at the index transition interface. The benefit of removing the DBRs from the VCSEL design is significant. About 180 layers of the DBR layers can be removed from the epi structure, which tremendously simplifies the epi wafer growth. And the shorter cavity length makes the laser to be modulated and tuned faster.

However, the challenge of such device is also obvious. The HCM fabrication at both side of the device is demanded. Therefore, the flip-chip bonding and substrate removal has to be performed for the second HCM mirror fabrication. As the epi layer is less than one or just a few microns thick, processing on such a thin layer bonded on an alien substrate is extremely challenging.

4.1.2 Short Cavity Surface Emitting Laser Design

Here we propose an alternative structure leveraging HCM with or without airgap from the substrate, integrated with VCSELs. Such Short Cavity Surface Emitting Laser (SC-SEL) can increase the wavelength tunability, reduce the total epi-structure thickness and enable large-scale manufacturing of III-V and silicon heterogeneous integration. It also reduces photon lifetime and electron transit time, which are desirable for high speed direct modulation.

In order to achieve better thermal conductance, the low index gap for the bottom HCM reflector is not favored. For the HCM VCSEL in the previous reports, the HCM structure is released to be suspending in the air. The full low index surrounding can provide the highest reflectivity and the largest bandwidth. When the HCM mirror serves as the bottom reflector, this air gap between the VCSEL active region and the substrate creates extra thermal resistance. Therefore, the HCM reflector design with the physical connection between the active region and the HCM bars are desired.

There are some reports for this kind of reflector [73, 74]. The first structure is essentially a T-shape HCM, with a narrow neck connecting the HCM and the active region, as shown in Figure 4.1(a). For the 1550 nm design, the HCM bars are made of AlGaInAs and the narrow neck is made of InP. The HCM is designed as $\Lambda = 660\ nm$, $DC = 0.66$, $t_g = 400\ nm$ to achieve high reflectivity for TM-polarized light. The contour map is plotted to sweep the optimal thickness for the narrow neck, as shown in Figure 4.1(b). The corresponding reflectivity is simulated to show better than 200 nm bandwidth with reflectivity greater than 99%. The field distribution of the T-HCM reflector under surface normal incidence is simulated by FDTD method, as plotted in Figure 4.1(d).
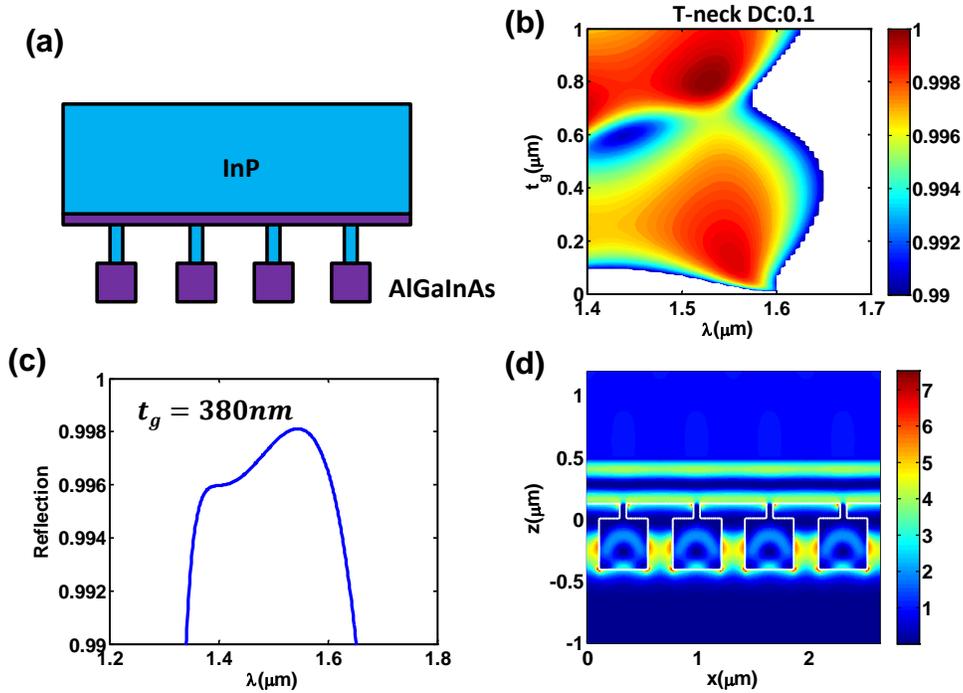
Figure 4.1 (a) Schematic for T-HCM reflector (b) The reflection contour plot for the T-HCM with TM-polarization incidence. The spectra is plotted by varying the T-neck thickness. The duty cycle of the narrow neck is 0.1. (c) The reflection spectrum of the T-HCM. The wide part dimension is $\Lambda = 660\ nm$, $DC = 0.66$, $t_g = 400\ nm$. (d) The field profile of the T-HCM reflector.

Another approach is called Giant Reflectivity to Order (GIRO)-grating. Comparing with the HCM reflector, the refractive index of the incidence region is also high index, as shown in the inset of Figure 4.2. The GIRO reflector can also achieve very high reflectivity. However, because of the minimal index contrast at the incidence interface, the bandwidth for high reflectivity is much smaller, covering from 1532 nm to 1566 nm. The advantage of the GIRO structure is the simple fabrication. The grating can be realized with one step of etching and the grating layer can be made of the one uniform layer. Comparatively, the HCM or T-HCM reflector requires selective etching for the undercut. It is a complex process to undercut the narrow neck with maintaining straight side wall.
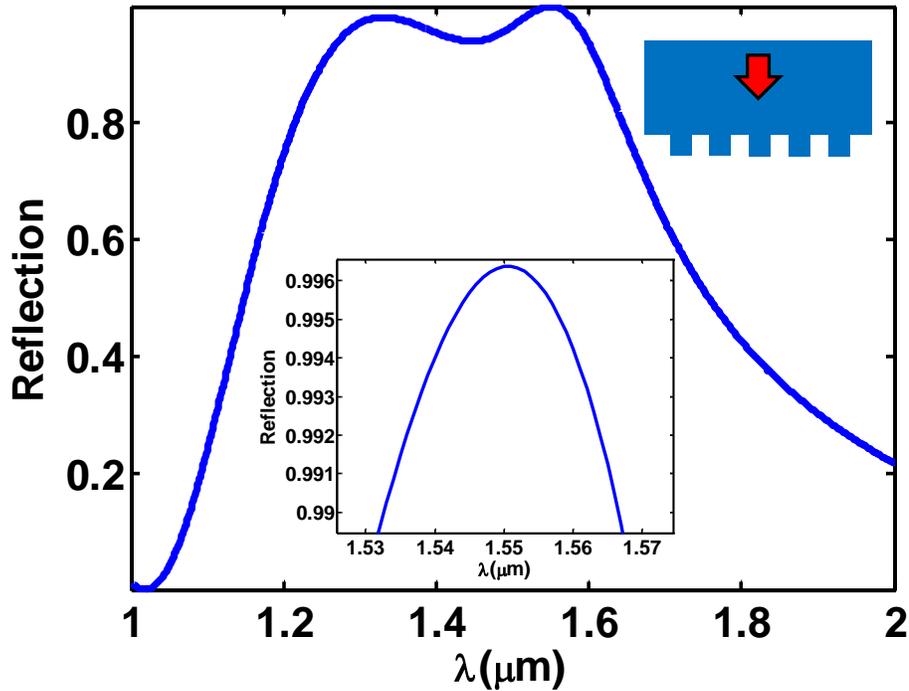
Figure 4.2 The reflection spectrum of the GIRO reflector. The insets show the schematic of the GIRO grating as well as the zoom-in plot for reflectivity greater than 99%.

The schematics of the Short Cavity Surface Emitting Lasers (SC-SEL) are shown in Figure 4.3. The SC-SEL hetero-structure consists of a current spreading layer, active region and two mirrors. The mirrors are high reflection HCM. In this case, they are directly placed on top and bottom of the laser cavity and do not have an airgap from the laser cavity, referred here-in-forth as GIRO grating. In Figure 4.3, the HCM consists two layers, designed for selective etch-stop at layer 3. However, it could be made to consist multiple layers. In addition, layer 2 can have smaller width than layer 1, making it a T-HCM. Also, in Figure 4.3, the SC-SEL is shown to be bonded onto a carrier substrate, which has a uniform metal coating. However, this metal layer does not need to be present under the HCG. The proton implantation [75] or quantum well intermixing [76] can be used for the lateral current confinement. The schematic of the current confinement is also shown in Figure 4.3(a) and (b).
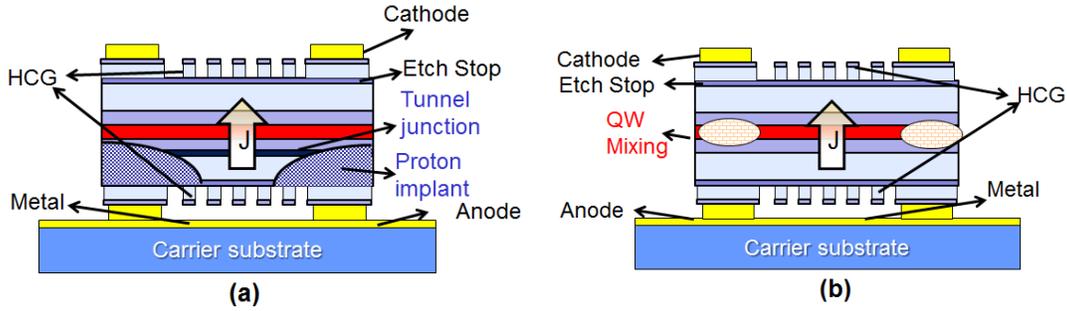
Figure 4.3 (a) SC-SEL with current confined by proton implantation (b) SC-SEL with current confined by Quantum Well mixing

The wafer design is shown in Figure 4.4 and Figure 4.5. Between the current spreading layer and active region, there can be a tunnel junction to facilitate efficient carrier injection and reduced free carrier absorption loss. The active region may consist of quantum well, quantum wire, quantum dot or bulk regions, and it can be any InP, GaAs, GaSb, GaN, and GaP-based materials emitting from 0.3 µm to 10 µm. The current confinement and optical confinement can be realized by proton implant, QW mixing or buried tunnel junction (not shown here). The carrier substrate can be Si, AlN, Al_2O_3, SiO_2, Si_3N_4, Diamond, metal or other III-V materials. The bonding between III-V and carrier substrate may be achieved by metal-to-metal bonding, molecular bonding or polymer bonding.
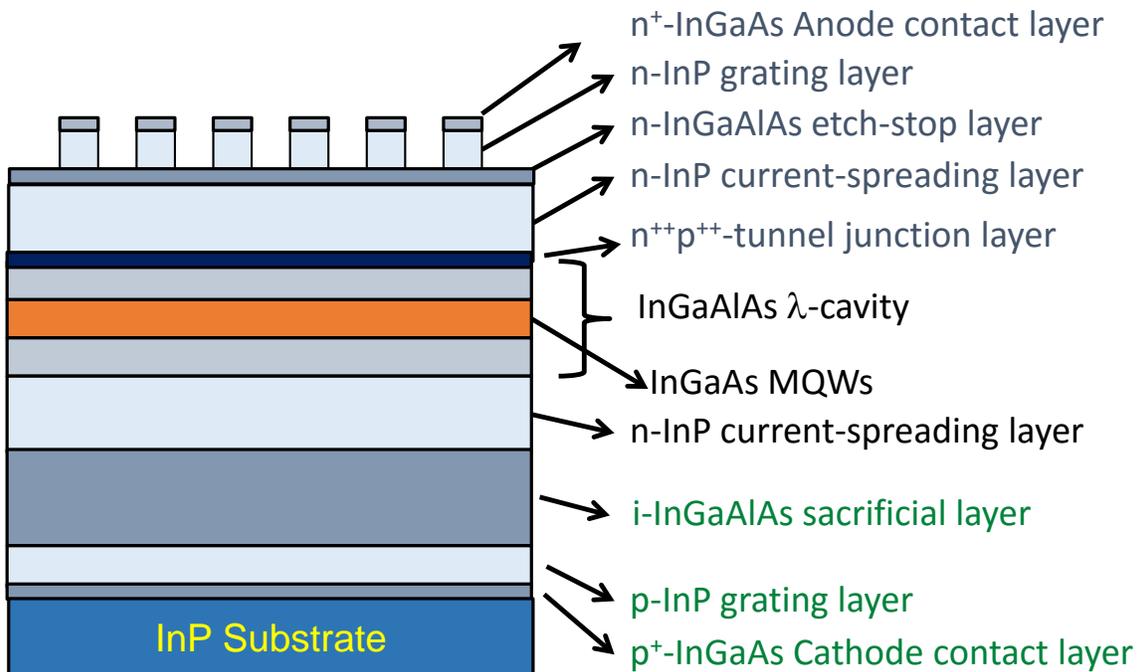
Figure 4.4 Wafer design for tunable proton implanted SC-SEL
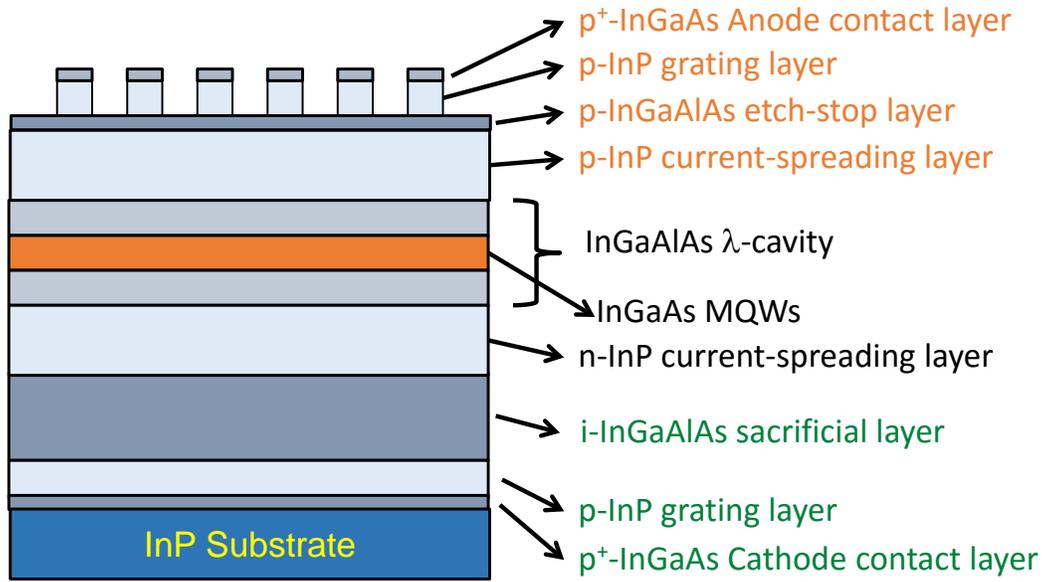
Figure 4.5 Wafer design for buried heterostructure SC-SEL

The optical cavity can be designed as the following strategy. The GIRO mirror is a subwavelength grating with high index in the input plane and low index in the output plane. It is defined by three parameters, period Λ, thickness t_g and duty cycle η which is defined by the ratio of the grating bar width s and the period Λ. By sweeping the parameters, the high reflection region (>0.99) is obtained, as shown in Figure 4.6.
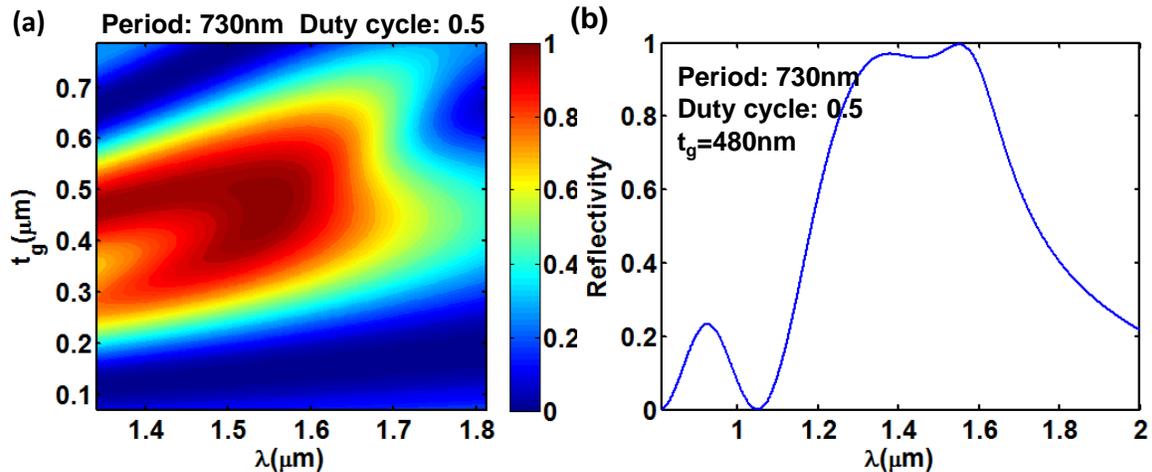
Figure 4.6 (a) Reflectivity spectrum contour map for different grating thickness (b) Reflection spectrum for 1.55 μm design.
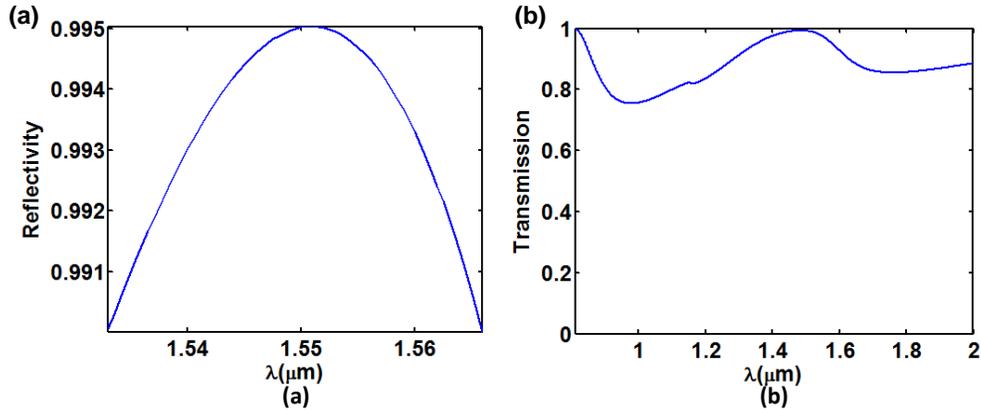
Figure 4.7 (a) High reflection spectrum of the mirror (b) Transmission of the GIRO with input from the low index plane

The cavity can be designed by tuning the phase matching layer inside the cavity to make the resonance at 1.55 μm or any other wavelength between 0.3 μm and 10 μm in principle. The field profile and Q value is therefore obtained by applying FDTD simulation. In the simulation, an external plane wave source is put upon the cavity in the low index surrounding. For HCG mirror without airgap, when the input source is from the low index side, it is highly transparent, as shown in Figure 4.7(b). Therefore, for the cavity, the transmission will be high except for the resonance. Figure 5 is the transmission spectrum of the cavity, a narrow dip occurs at the resonance frequency. According to the resonance spectrum, the Q value is 8000.
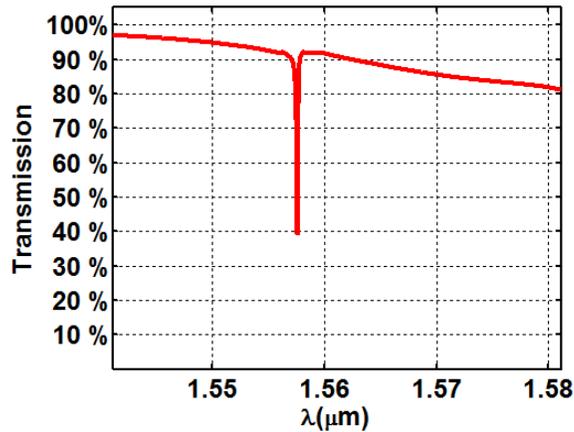
Figure 4.8 Transmission spectrum of the double GIRO cavity

In order to make the VCSEL tunable, one mirror is replaced by high contrast grating (HCG) with airgap. HCG is a subwavelength grating with high index contrast. In design, it is floated in the air and tuned by the MEMS structure. The schematics of such tunable VCSEL are shown in Figure 4.9(a) and (b). HCG can be designed as an ultra-broad high reflection bandwidth mirror. By varying the gap between HCG and the gain material, the cavity resonance frequency can be tuned.

The tuning of HCG mirror can be achieved by electrostatic actuation, piezoelectric actuation, or thermal actuation. Figure 4.9(d) shows the reflection spectrum with different air gap thickness. The sharp reflection change presents the resonance. According to this simulation, the tuning efficiency, which is defined as the ratio of the resonance wavelength change and tuning displacement, is 27.4%.
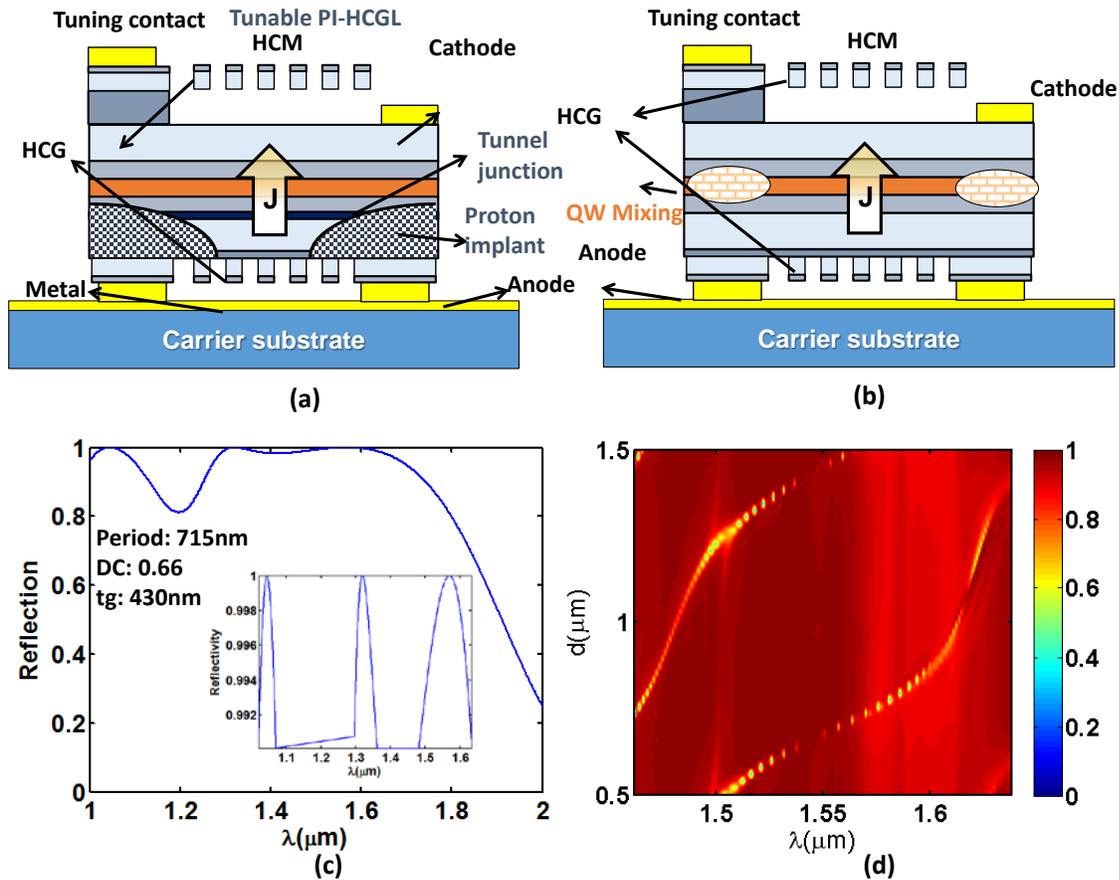
Figure 4.9 (a) Tunable SC-SEL with current confined by proton implantation (b) Tunable SC-SEL with current confined by Quantum Well mixing (c) Reflection spectrum for HCG (d) Reflection spectrum for different airgap thickness between HCG and gain media.

There is an important consideration for choosing the type of the bottom reflector, which is the field intensity at the etching surface. Because the etching can create many defects at the etching surface, strong field intensity around the surface can create excessive surface recombination that gives extra loss to the cavity. As a comparison, the field profiles of the GIRO and T-HCM reflectors are plotted in Figure 4.10. Unfortunately, the maximum intensity locates at the sidewall for both of the reflectors. However, the field for T-HCM reflector is about 4 times lower. The standing wave profile optical cavities made of both types of reflectors are also compared. As shown in Figure 4.11, the standing wave profile for the GIRO reflector cavity show very clear intensity peak at the interface of the reflector. It translates to large loss from the surface recombination. On the other

66

hand, the power intensity at the etching surface of the cavity with T-HCM reflector is suppressed to be much weaker than the field inside the active region. Therefore, even though the GIRO reflector has great advantage for the convenience in fabrication, the T-HCM is preferred to achieve lower optical loss from the mirror.
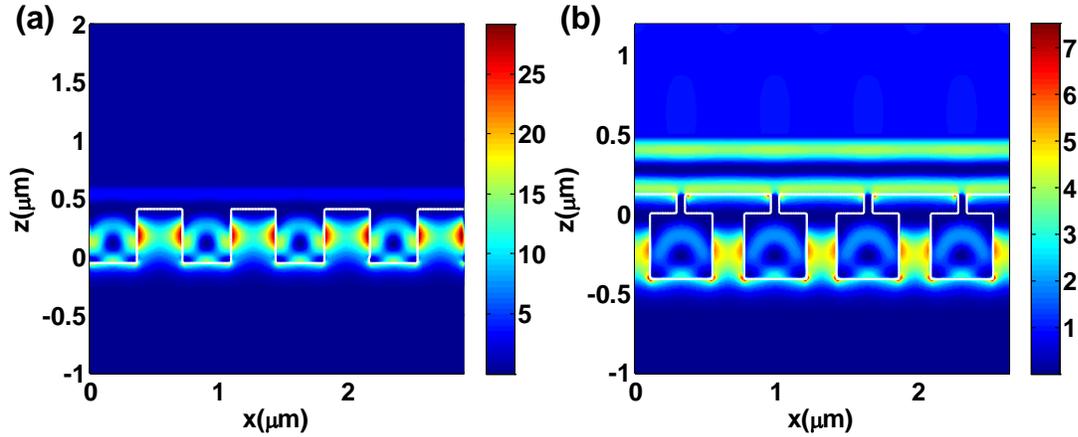
Figure 4.10 Optical field distribution for (a) GIRO reflector (b) T-HCM reflector.
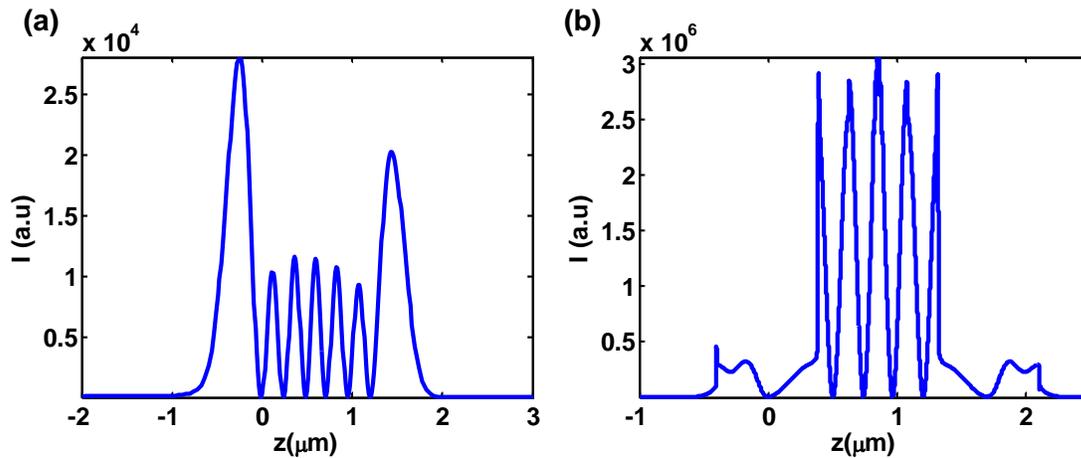
Figure 4.11 The standing wave power distribution for (a) GIRO reflector cavity (b) T-HCM reflector cavity.

4.2 InP-based VCSEL on Silicon HCM

4.2.1 Laser on Silicon for Optical Interconnection

In the past decades, the optical links are replacing the electronic interconnections for data communication in different scales. The long-haul optical communication has been the backbone of today's internet. Starting from 2005, the optical fiber links starts to replace the copper cables for the rack to rack communication in the data centers and super computers [77]. As the computing

capacitance keeps following the Moore's law, the I/O speed for board to board and chip to chip communication has been pushed to 40 Gbps and above. Those ultra-high speed links are currently still working on the electronic links for short distance. However, as the circuit parasitic scale up with the data rate, the electronic link suffers from tremendous signal degradation. The power consumption also increases as charging larger parasitic capacitors. Therefore, the electronic link is reaching its limit for the short distance interconnections.

However, the circuit parasitics do not affect for the optical interconnections. The optical channel provides a much cleaner channel for the bit transmission. It also eliminates the parasitic capacitance in the signal transmission, and as reduces the power consumption. In addition, the signal with better fidelity can also reduce the complexity for the receiver to reconstruct the data. An integrated light source on the circuit, in particular on silicon, will pay a key role in addressing the fast growth of the interconnect and width [78]. Several devices have been proposed to approach the laser integration on silicon [79], including silicon Raman laser, Ge-on-Si laser, hybrid silicon microring and microdisk laser,etc. However, such devices are still in very early stage and far from being ready for system adoption.

VCSELs are particularly promising candidates as light sources for silicon photonic circuits because of their low manufacturing costs, testing scalability, low power consumption, facilitation of 2D array, and high data transmission rates [28]. A major challenge to integrate a VCSEL onto an SOI substrate lies in the very large thickness of a typical distributed Bragg reflector (DBR) required for a long-wavelength VCSEL, making it difficult to couple its output light to an in-plane waveguide. In addition, the vertical optical coupling needs to be addressed to coupling the light emission from the VCSEL in the surface normal direction into the photonic waveguides on the chip.

We have been repeatedly using the unique high reflection property from the HCM. In chapter 5, we will show the HCM can be designed as a very efficient vertical coupler, providing > 95% coupling efficiency. Here, we combine both of the functions into one HCM structure to enable the VCSEL to silicon photonics integration. First of all, this HCM serves as the cavity mirror for the VCSEL, providing > 99% reflectivity. In addition, it also serves as the vertical coupler to couple the output power into the silicon photonics chip. The schematic of this structure is shown in Figure 4.12. This HCM reflects > 99.4% of the light, and also couples 47% of the output power into the in-plane waveguide. The reflection and coupling spectra are shown in Figure 4.12(b). To give a more straight forward value for the coupling efficiency, the coupled power is normalized by the total output power. At 1550 nm wavelength, almost half of the output power is coupled into the waveguide.
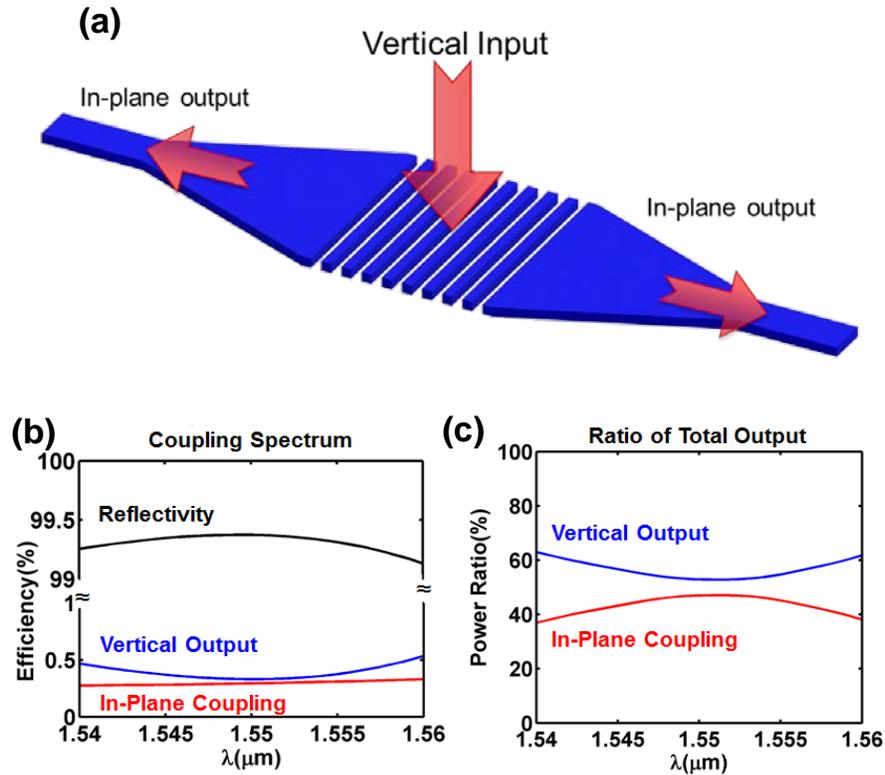
Figure 4.12 HCG reflector and coupler simulation with FDTD. The HCG layer consists of a 358-nm thick silicon layer on an SOI substrate.

Because the gain of the VCSEL has to come from IIIV compounds, in specific, InP material system, for the direct bandgap based on current technology, the InP epi structures need to be bonded on the silicon photonics chip. We choose to use a AuSn eutectic thin film to facilitate this bonding. The metal alloy is also used as the contact and heat conductor for the VCSEL operation. The schematic of the VCSEL is shown in Figure 4.13. The bottom HCM is made on the device layer of the SOI wafer. The InP epi layers are flip-chip bonded onto the SOI chip. Currently, the top mirror is still DBR reflector. More efforts are being made to replace the top DBR mirror by another HCM reflector and consequently totally remove the DBR from the VCSEL structure.
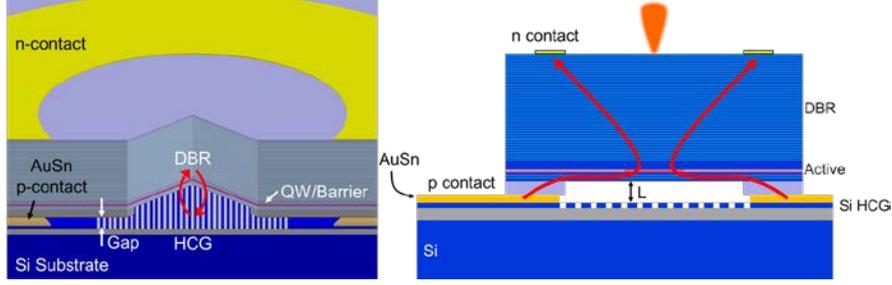
Figure 4.13 Schematic of VCSEL with silicon HCG as bottom mirror.

Unlike the full VCSEL on InP substrate, the VCSEL built from this integration strategy ca have the extra freedom to control the cavity optical length (L) in the fabrication process. It is realized by controlling the boding metal thickness. This degree of freedom helps us to compensate the inaccuracy of the epi-layer thickness, in order to achieve the round-trip phase condition for the FP cavity. The optical length is defined as the summation of all epi-layer thickness weighted by their refractive indices, show as:

$$L = \sum_{i=1}^{N} n_i L_i \qquad 4.1$$

The phase matching condition is:

$$\frac{2\pi}{\lambda_0} \cdot 2L + \varphi_{HCM} = 2m\pi \qquad 4.2$$

Giving:

$$L = \frac{2m\pi - \varphi_{HCM}}{4\pi} \cdot \lambda_0 \qquad 4.3$$

Notice φ_{HCM} is the reflection phase from the HCM reflector. It can be obtained from the analytical formulation. For an HCM reflector designed with 660 m period ad 275 nm air gap width, the phase response is $\varphi_{HCM} = 1.2\pi$. As a result, the metal thickness needs to be $L = 1.8\ \mu m$. In principle, Thinner metal thickness at around 1um can also satisfy equation 2.13 and give shorter cavity length. However, the HCM should not be placed too close to the active region to void the tunneling coupling between HCM and the active region.

The standing wave distribution is calculated by the transfer matrix method, as shown by the traces in Figure 4.14(a). The red trace represents the refractive index distribution of the epitaxial structure. The green trances are the band diagram for the conduction and valence band. The optical intensity of the standing wave is shown by the blue trance. The key for the cavity design includes two parts: one is to make sure the quantum wells aligned to the peak of the intensity to maximize the confinement factor. The other is to make sure the interface between the active region and the low index gap is aligned to the intensity peak, so to minimize the field intensity in the low index gap

70

and the HCM reflector. The optical intensity of the quantum wells and the interface plotted in Figure 4.14(b).
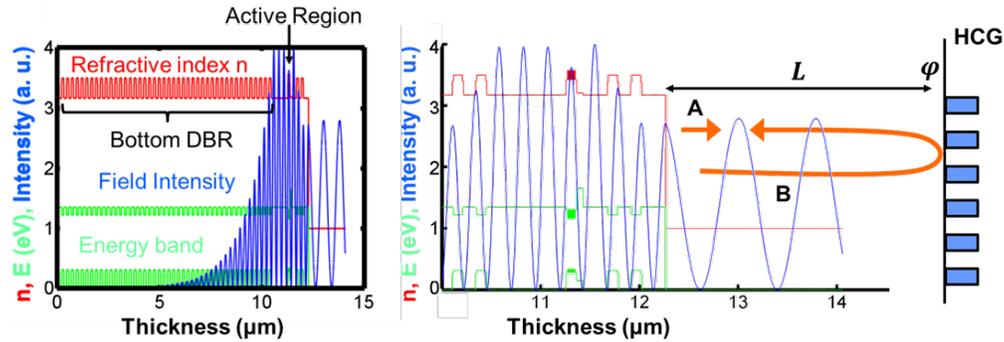
Figure 4.14 TMM simulation of the VCSEL cavity.

4.2.2 InP VCSEL on Silicon

The silicon HCG is fabricated on a 6" SOI wafer using a 248nm DUV ASML lithography stepper and a Cl_2-HBr dry etching process. A 1.3 μm thin film metallic stack is deposited with electron-beam evaporation at a hyper-eutectic composition for the AuSn material system. In Figure 4.15(a)and (b), we show a tilted-view colorized SEM of the Si-HCG reflector on an SOI substrate, surrounded by the AuSn thin film (yellow) ready for bonding. The flip-chip thermo-compression bonding process is performed in inert nitrogen ambient at 340 ℃ with 10 N of force. InP substrate removal is done via wet chemical etching using HCl and H_3PO_4. Figure 4.15(c) shows a 3D-scanned confocal microscope image of a Si-HCG VCSEL.
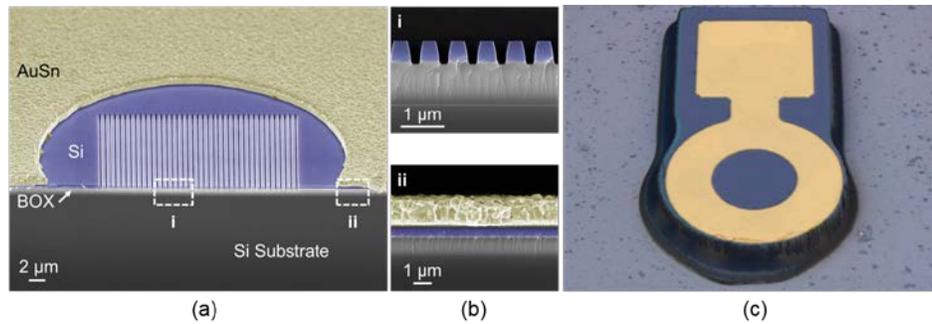
Figure 4.15 (a) Tilted-view colorized SEM of Si HCG reflector with a AuSn film. (b) Cross section view of Si HCG (i) and AuSn alloy (ii) (c) confocal microscope image of VCSEL.

Figure 4.16 shows the temperature dependent light-current-voltage (LIV) characteristic of a VCSEL with CW operation achieved up to 60º C, and >1 mW CW output power at 15 ℃. The inset shows the near field intensity below and above threshold. Also in the inset is a 3D-scanned optical micrograph of a fabricated VCSEL. Single transverse and longitudinal mode emission was observed over the entire current and temperature range. The VCSELs exhibit thermal rollover with

increasing current bias due to gain spectrum red-shifting more rapidly than the resonant cavity spectrum, an effect typical in VCSELs. The devices have slope efficiencies of ~0.3 mW/mA and threshold current i_{th} as low as of 7 mA. The ripples on the LI curve are due to residue reflection from the back of the silicon substrate/air interface, as verified by the output spectra measured at various currents corresponding to the peaks and valleys of the L-I curve and the substrate thickness. In the future, the L-I ripples can be eliminated with roughening the backside of the substrate.
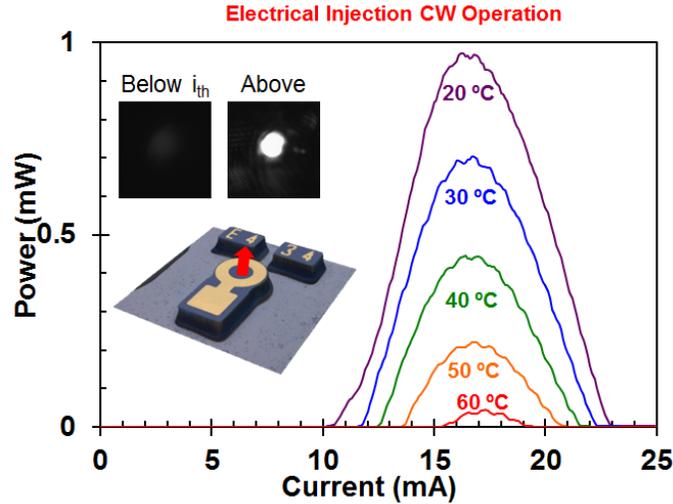
Figure 4.16 Temperature dependent CW LIV.

Using a Si HCG and AuSn bonding layer—instead of a traditional quaternary alloy DBR—results in excellent thermal performance. As mentioned above, the thermal conductivity of AuSn is roughly an order of magnitude better than for a quaternary alloy such as AlGaInAs The thermal resistance of the laser is determined by the following ratio:

$$R_{th} = \frac{\Delta T}{\Delta P} = \frac{\Delta\lambda/\Delta P}{\Delta\lambda/\Delta T} \qquad 4.4$$

The top and bottom terms in Equation 4.4 can be extracted from the spectral properties of the laser. Figure 4.17 shows the wavelength shift of the device for varying injection bias (at a fixed heat sink temperature of 20 ℃), as well as the wavelength shift versus temperature (at a fixed injection current of 1.5 i_{th}).

The wavelength shift versus dissipated power is measured to be 0.143 nm/mW, and the shift versus temperature is 0.098 nm/K, as shown in Figure 4.18. The latter is determined by the index change of the VCSEL cavity versus temperature. Taking the ratio of these two numbers, the experimental thermal resistance of our device is 1.46 K/mW, better than that was obtained for a long-wavelength VCSEL on an InP substrate.
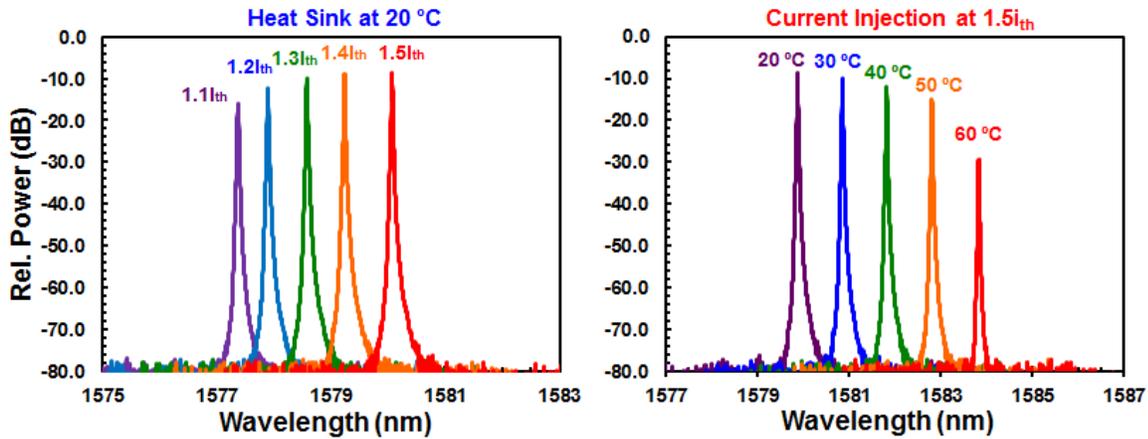
Figure 4.17 Spectrum at different bias currents and temperatures.
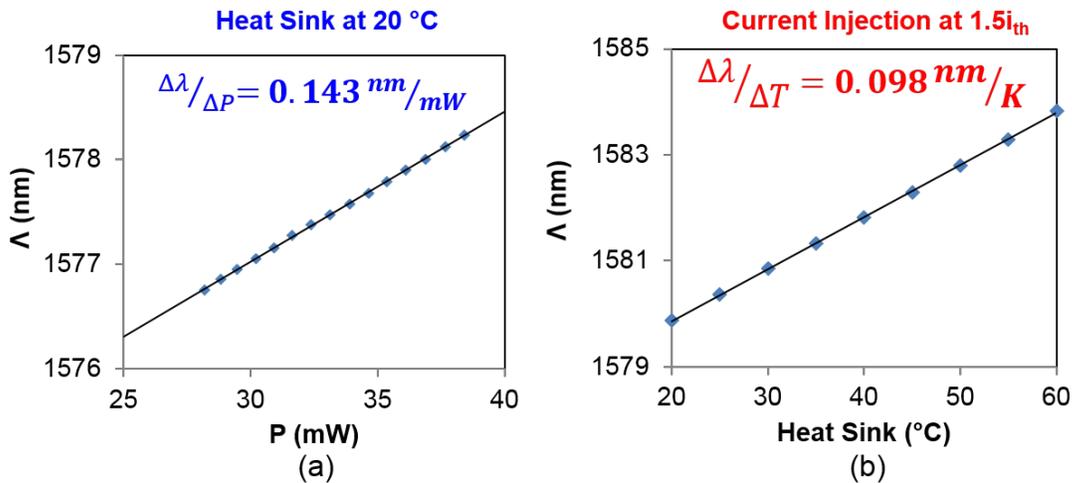
Figure 4.18 Wavelength shift versus dissipated power and (b) versus heatsink temperature.

4.3 HCM VCSEL on Flexible Substrate

4.3.1 Design Consideration for Flexible VCSEL

Photonic integrated circuits (PICs) have been the workhorse of communications, displays, and sensors. However, the rigidness of the devices limits their use in the realm of soft optoelectronic applications. In order to achieve the complete optoelectronic functionality for soft PICs, components such as emitters, transmitters, and detectors, have to be realized on a flexible substrate with performance comparable to the devices on a rigid substrate. The latter two can be readily transferred to a flexible substrate without having to overcome major obstacles in device physics, owing to the tight light confinement of silicon waveguides, and efficiency and sensitivity of

73

germanium photodetectors. The emitter, on the other hand, is challenging to transfer, especially for laser devices that operate at silicon-transparent wavelengths (e.g. 1550 nm), because of the poor thermal conductance of flexible substrates.
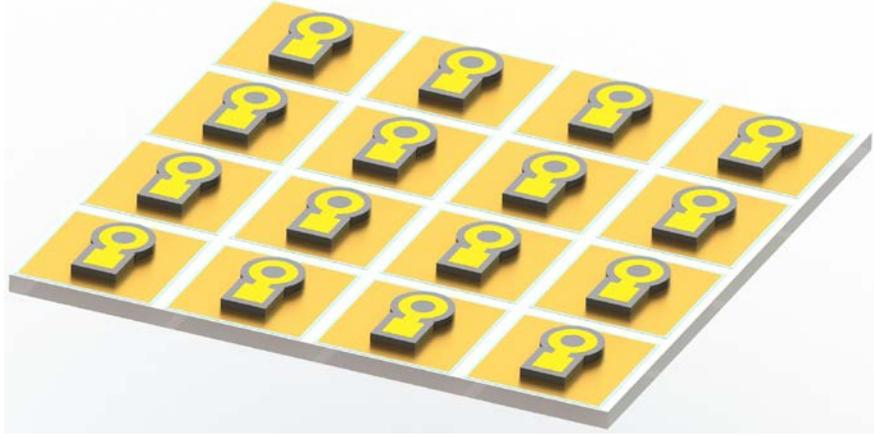
Figure 4.19 The schematic of the Si-HCM VCSEL on flexible substrate.

The conventional VCSEL width DBR reflector as well as the top mirror HCM VCSEL both have a thick DBR reflector between the active region and the substrate, which is typically where the heat sink is. The thermal conductance of the DBR as a bulky superlattice is compromised. The thermal simulation of the device is performed by Finite Element Method (FEM) in a commercial package COMSOL. In the simulation model, the heat generation is assumed to the 25 mW in the active region, which is a fair number from empirical statistics of the fabricated devices. The simulation shows that the maximum temperature in the active region can be up to 183°C, as shown in Figure 4.20(a). This temperature is much hotter than the cold cavity at the room temperature. The high temperature not only reduces gain. It also causes the red shift of the resonance wavelength of the cavity and the bandwidth for the gain. As a rough estimation, the gain red shifts twice as faster as the cavity resonance wavelength. Once the resonance is off tuned from the gain, the VCSEL will stop to laser. Therefore, as the device operates on a flexible substrate, much higher temperature can be reached since the substrate is typically made of polymer or plastics, possessing the thermal conductance 1000 times lower than the crystalline semiconductor. A schematic of the flexible device is shown in Figure 4.19.

One can argue than the HCM VCSEL in [28] can be transferred in the flexible substrate upside down, such that the active region is much closer to the substrate. However, the HCM structure is fully suspended in the air. Flipping the device on to a new substrate can very easily break the HCM. Therefore, this approach is not favored from the processing point of view.
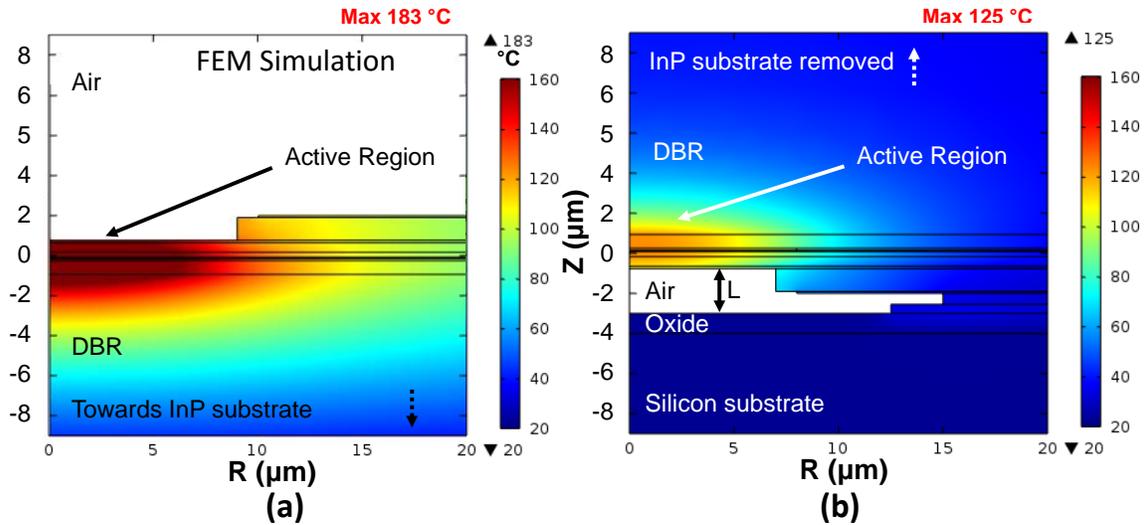
Figure 4.20 COMSOL FEM heat distribution of (a) HCM VCSEL and (b) bonded Si-HCG VCSEL.

On the other hand, the Si-HCM VCSEL in Section 4.2 has the low index gap sealed by the bonding metal. Therefore, extra processing steps can be performed after the HCM is being made, without the concern of collapsing the HCM, as the devices reported in [28]. The active region in this case is much closer to the heat sink. Similar thermal simulation is also performed by FEM. Under the same heat generation, the maximum temperature is reduced to 125°C. That is 60°C lower than the HCM VCSELs.

4.3.2 Flexible Si-HCM VCSEL
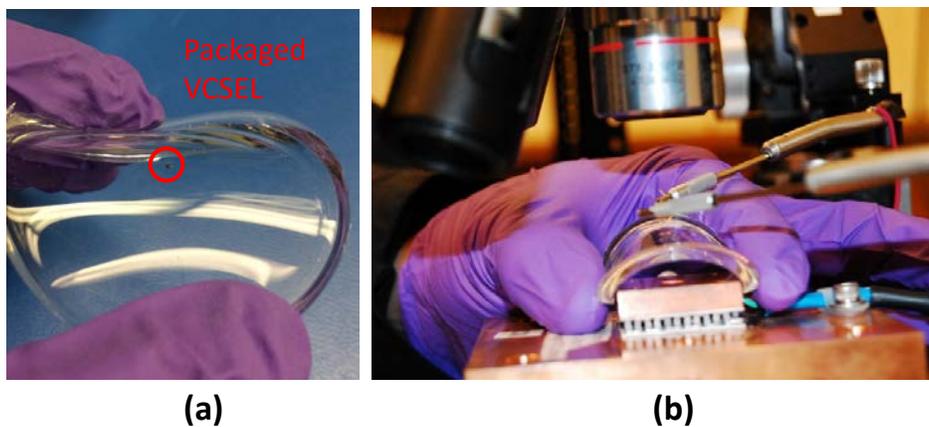
Figure 4.21 The photograph of (a) packaged VCSEL in PDMS substrate and (b) the measurement setup.

The Si-HCM VCSEL is packaged inside the PDMS substrate, as shown in Figure 4.21(a). As the concept demonstration, the device is tested by the probe tips with the substrate bent to demonstrate

its flexibility in operation. The PDMS substrate can also be heated up for testing the device characteristics under different temperatures.

The LI curve of the flexible VCSEL is shown in Figure 4.22(a). The maximum output power can reach 0.65 mW. And the spectrum of the output light shows very clean single mode operation. However, the heat accumulation becomes overwhelming after the device operates for a few seconds. The lasing wavelength red shifts as the device temperature is rising. Once the cavity resonance wavelength and the gain spectrum are detuned, the device stops lasing. This process happens in about 5 seconds. However, it is a reversible process. By stopping the pump for around 30 sec, the device can start to lase again.
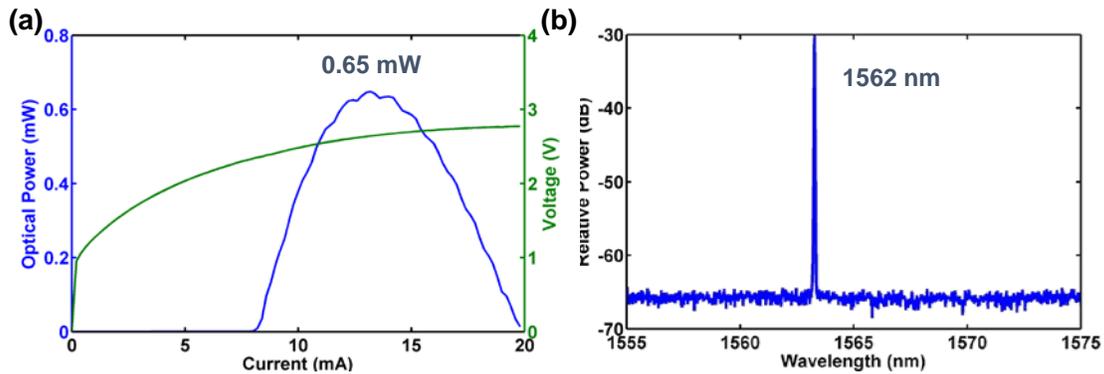
Figure 4.22 (a) L-I curve of the Si-HCM VCSEL in the flexible substrate. (b) The optical spectrum of the VCSEL output.

This behavior clearly show that the VCSEL operation is limited by its thermal conductance. The heat distribution is analyzed in Figure 4.23(a). It shows the maximum temperature of the device reaches 177°C. That is a 50°C temperature increment from the original device.
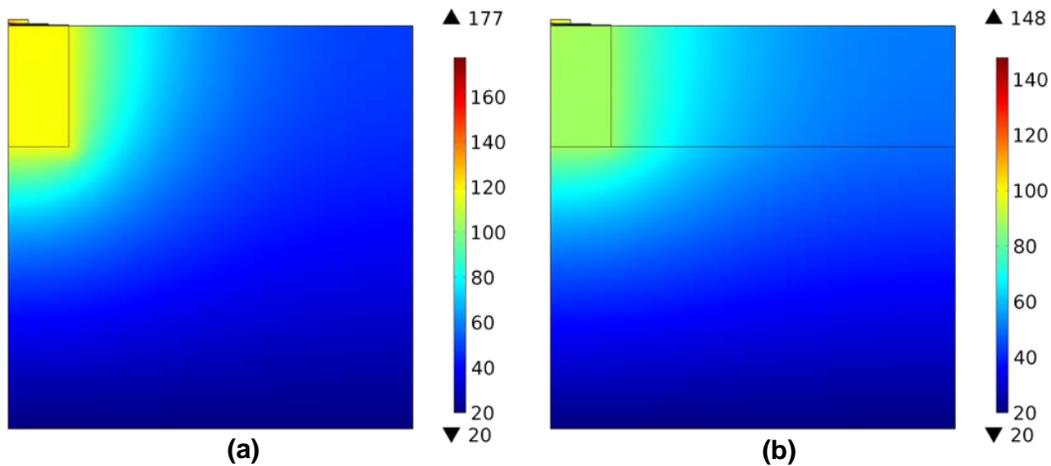
Figure 4.23 COMSOL FEM heat distribution of (a) Si-HCM VCSEL on PDMS and (b) Si-HCM VCSEL on PDMS with metal heat spreading.

To extract the heat out from the VCSEL more efficiently, we use a metal heat spreading layer. Before packing the VCSEL, the PDMS substrate is coated by a 500 nm thick gold film. The VCSEL is packaged on the gold layer. Under this approach, the excessive heat can spread laterally, which consequently reduce the temperature in the cavity. This effect is simulated in Figure 4.23(b). The extra heat spreading provides 30°C temperature reduction, making the cavity only 20°C hotter than the device on the silicon substrate.
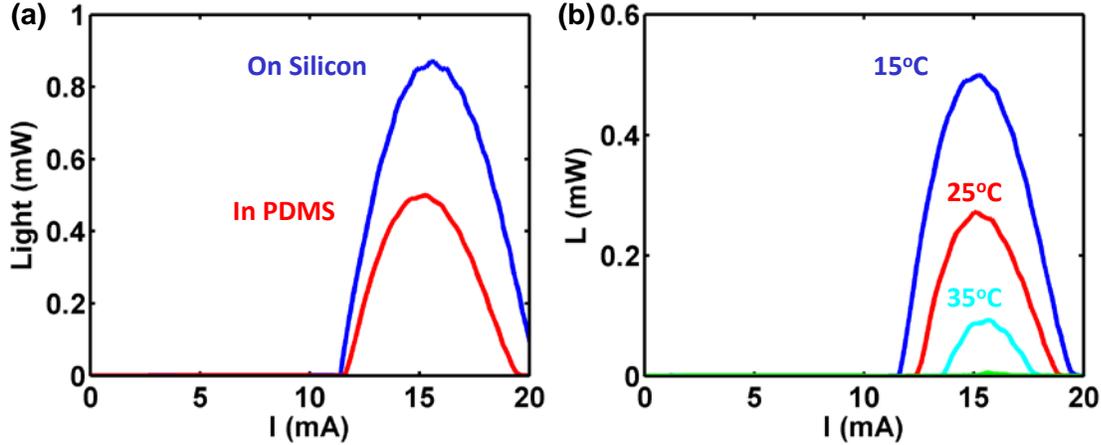
Figure 4.24 (a) LI curve of the VCSEL on silicon substrate and in PDMS substrate with the heat spreading layer. (b) The LI curves for the VCSEL in PDMS substrate under different substrate temperature.

With cooler active region, the VCSEL achieves real continuous wave operation at the room temperature. As a comparison for the device on silicon substrate and in the PDMS, the threshold current of the flexible VCSEL is actually very close to the device on silicon. However, because of the extra heat accumulation, the maximum output power is reduced by 40%, with earlier roll over behavior.

The flexible VCSEL is also tested under the different substrate temperature, as shown in Figure 4.24(b). The CW operation is achieved for the substrate heated up to 35°C. This temperature is very close to the human body temperature, making the device have great potential for the flexible systems operating on the human skin.

The thermal resistance is measured with the approach described in Equation 4.4. Output wavelength is measured under different pump current and substrate temperature. The extrapolation results the thermal resistance to be $R_{th} = \frac{\Delta T}{\Delta P} = \frac{\Delta \lambda / \Delta P}{\Delta \lambda / \Delta T} = 2.1 \, K/mW$. It is anticipated to be higher than the value on Si substrate, which is $1.46 \, K/mW$. However, it is already comparable to the HCM VCSEL in [28] with the metal heat sinking.
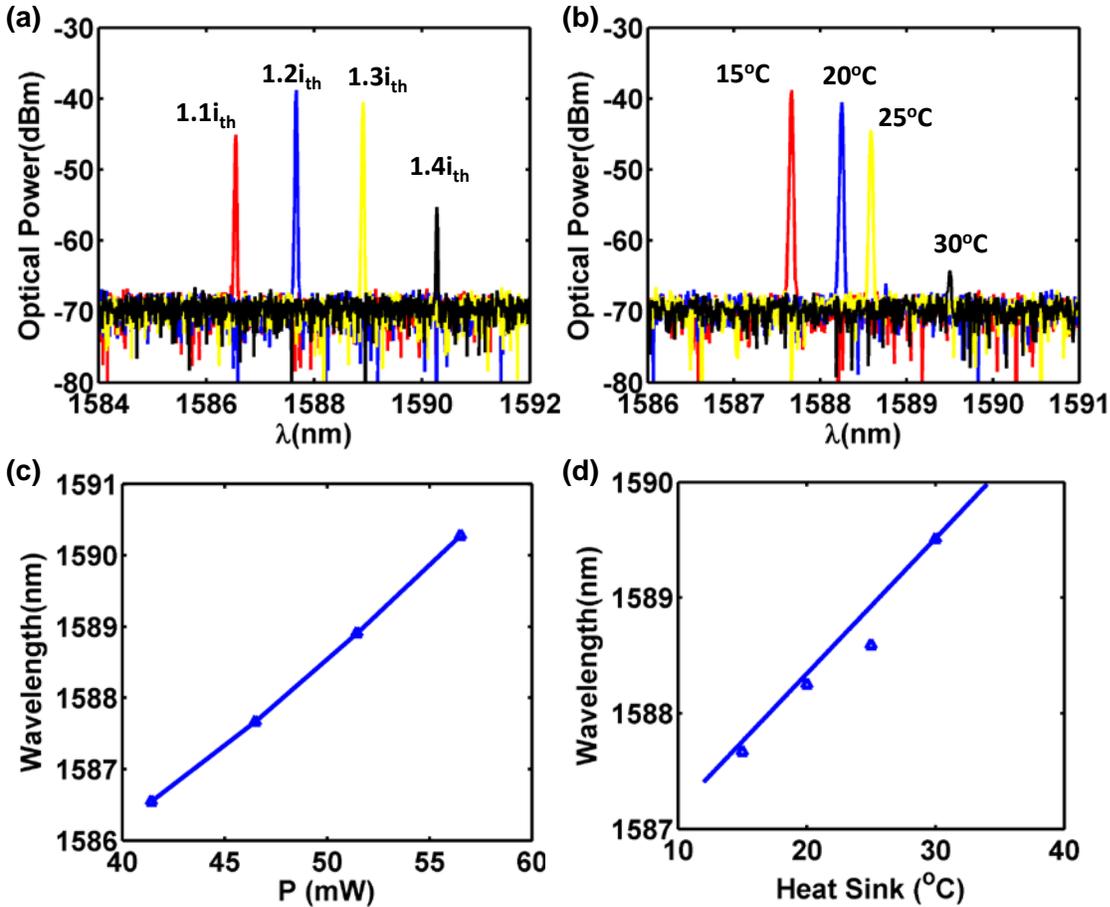
Figure 4.25 Spectrum at different bias (a) currents and (b) temperatures; Wavelength shift (c) versus dissipated power and (d) versus heatsink temperature.

4.3.3 Outlook for Flexible VCSEL Array

The device in Section 4.3.2 is fabricated by packaging the VCSEL dies into the PDMS substrate. This approach is not suitable for make large flexible VCSEL arrays, since the rigidness starts to impact the flexibility as the die size becomes larger. A process follow based on the transfer printing method is described in Figure 4.26.

Because the bottom HCM is fabricated on the SOI substrate, the buried oxide (BOX) layer can be selectively etched away, releasing the VCSELs from the substrate. Next, the PDMS stamp covers the chip uniformly to reach adhesion to the VCSELs. After peeling of the stamp, the VCSEL array is transferred to the PDMS stamp. However, it is important to note that all the metal contacts are at the bottom side of the device at this moment. They cannot be reached until the second transfer step is performed. Based on this approach, the VCSEL arrays can be transferred to any alien substrates, such as polymer, plastics, glass, etc. The receiver substrate can be treated by O_2 plasma to promote the adhesion to the VCSELs.
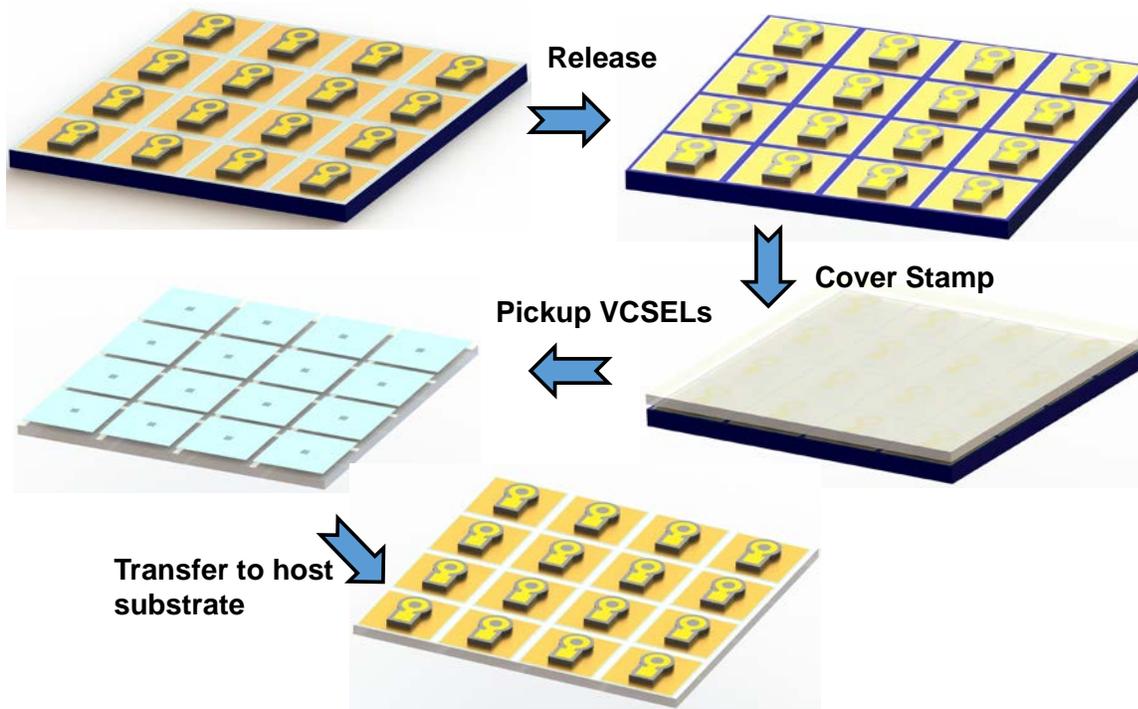
Figure 4.26 Process flow for the large flexible VCSEL array with transfer printing method.

4.4 Summary

The HCM reflector can replace the DBR reflector in the VCSEL design to achieve larger high reflection bandwidth with 50 folds thinner thickness. It can significantly reduce the number of the layers in the epitaxial wafer and improves the thermal conductance from the quantum wells to the heat sink. In this chapter, we proposed the design for the short cavity VCSEL with both mirrors replaced by the HCM reflectors. To further improve the thermal conductance, we adopted the HCM reflector with small mutation. It can be designed to have a narrow neck connecting the HCM and the high index active region, known as the T-HCM reflector. Or, the low index gap can be removed while still achieving high reflectivity with the light incidence from the high index medium.

We also developed the flip-chip bonding technique to achieve the VCSEL with the bottom DBR mirror replaced by the HCM reflector. The thermal conductance is significantly improved with this scheme, as the distance between the quantum wells and the substrate is much smaller. With such a large improvement, we further investigated to use this Si-HCM VCSEL in the flexible substrate. The initial demonstrate proves that the VCSEL is capable to achieve lasing even being placed on the polymer substrate with 1000 times worse thermal conductance. However, the excessive heat generated by the pump current is not properly addressed and the device stops lasing after 5 seconds. To better extract out the heat from the laser, we add a metal heat spreading layer in the flexible substrate. It can reduce the maximum temperature in the active region by 30ºC. Continuous wave operation is achieved with this optimization and the flexible VCSEL keeps lasing

with the substrate temperate increased up to 35ºC. For the large VCSEL array on flexible substrate, we also propose a transfer printing process to attach the VCSEL array on to any arbitrary substrates.

Chapter 5

HCM for Photonic Integration

5.1 Coupled HCM Resonance

The HCM can be designed as an excellent resonator with extremely high quality factor [31, 39]. The resonance mechanism has been described in Chapter 2. In essence, it is created by the constructive interference of the resonance of two eigen-modes in the HCM. For a resonator working in the dual mode regime under surface normal incidence, only 0th and 2nd array waveguide mode are excited. The single trip phase accumulation for them are noted as Ψ_0 and Ψ_2. When $\Psi_0, \Psi_2 = m\pi$, the eigen-mode satisfies with Fabry-perot resonance condition. When the resonance of the 0th and 2nd order mode happens at the same wavelength for an HCM structure, the phase difference $\Delta\Psi = |\Psi_2 - \Psi_0|$ could be either even or odd number times π. If it is an even number, the resonance of 0th and 2nd order is so called in-phase, which can achieve constructive interference. Therefore, the resonance have strong coupling to each other and make the HCM as an excellent resonator.

When the HCM resonator is placed next to an external photonic structure possessing a definitive eigen-mode, the optical coupling can exist if the distance between the HCM and the external structure is smaller than the penetration depth of the evanescence HCM surface wave. The schematic of such a structure is shown in Figure 5.1. The coupled resonance structure consists of two parts: an HCM structure and a waveguide on an SOI wafer. They are placed very close to each other with a low refractive index gap.
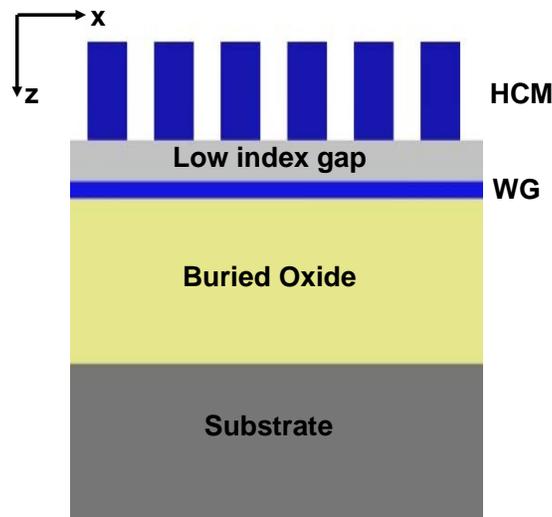
Figure 5.1 The schematic of the coupled HCM resonance structure. A HCM is placed on top of a photonic waveguide made on the SOI wafer. There is a low index

gap between the HCM and the waveguide to ensure the low index surrounding for the HCM.

As the period of the HCM is smaller than the wavelength, only 0th diffraction order allows propagation wave under the surface normal incidence. However, the evanescence wave still exists in the rest of the diffraction orders, whose propagation constant in z-direction is an imaginary number. The optical field in those orders are tightly bounded to the HCM interface, and the field intensity decays exponentially as the distance from the interface increases. As a result, those surface waves cannot be observed in the far field. However, if a high refractive index medium within the reach of the surface wave, the distance of which is typically defined at the field intensity decays less than e^{-1} of the intensity at the interface, the evanescence wave can be picked up in the high index medium and coupled into a propagation wave. This is also known as the optical tunneling effect.

In the case shown in Figure 5.1, if the surface wave matches the waveguide eigen-mode in the x-direction, the coupling between the HCM and the waveguide can be created. This condition can be determined by the phase matching condition. In general, for periodic structure, incident light with an angle θ_i with respect to surface normal direction is spatially modulated in the x-direction by the periodic structure. At the exiting plane $z = t_g$, the light field can be expressed as $E(x) = E_0 e^{ik_0 \sin \theta_i x} \sum_{m=0}^{\infty} A_m e^{i\frac{2\pi}{\Lambda}mx}$, where A_m is the amplitude of the mth diffraction order obtained from Fourier transform calculations. For a waveguide mode with effective refractive index n_{eff}, the phase will be matched between that of the near-field light wave and the waveguide mode if $n_0 \sin \theta_i + m\frac{\lambda}{\Lambda} = n_{eff}$, where n_0 is the refractive index above the incidence plane. Light thus couples into the waveguide with a coupling efficiency γ_0 at phase matching. Because n_0 is always smaller than n_{eff} for a waveguide, the coupling order m has to be larger than 0. Typically, m is chosen to be 1 to minimize the light leakage to other higher diffraction orders.

Now, as we understand the coupling between the HCM and the nearby waveguide is possible, how to evaluate the coupling strength. In the other words, how to use our simulation tools to find the HCM design to achieve strong coupling between the HCM and the external waveguide. One straight forward method is to use the FDTD simulation. If the strong resonance happens between the HCM and the waveguide, the field in the waveguide has to be greatly enhanced. Therefore, we can use the field intensity inside the waveguide to evaluate the coupling resonance strength. However, the drawback of this method is the simulation complexity. The variables of the simulation include the gap width, HCM duty cycle and thickness, as well as the wavelength. Looking for strong field enhancement in the 4-dimensional space is extremely difficult.

Another approach to find the resonance is to look for the resonance fingerprint in the optical spectrum. Because the diffraction spectrum of the HCM structure can be easily calculated by the analytical formulation or the RCWA method, this approach can be much faster with the guideline from the resonance physics. For a typical resonator, for instance, Fabry-perot resonator, the reflection spectrum has a sharp dip around the resonance wavelength. The narrow the dip with is, the high the quality factor will be. For the coupling between two resonances, we will expect to see the anti-crossing behavior in the dispersion curve.

Figure 5.2(a) plots the reflection spectrum of a single layer of HCM with varied thickness, without incorporating the waveguide structure underneath. As we have discussed in Chapter 2, the checkboard pattern defined by the interleaved lines are created by the resonance of the HCM eigen-modes. Those interleaved lines are the resonance conditions for the corresponding eigen-mode resonance. Therefore, in every resonance line, the propagation constant β_m satisfies $\beta_m \cdot t_g = n\pi$. Here, m denotes the order of the eigen-mode and n denotes the resonance order of the corresponding eigen-mode. Thus, t_g is the inverse of the propagation constant. The horizontal axis is the wavelength, which is the inverse of the frequency. Therefore, the resonance line is essentially the $\omega - k$ diagram, representing the dispersion curve of the resonance. For the oblique angle incidence, the odd order eigen-mode can also exist. As shown in Figure 5.2(b), an additional set of resonance curves show up for the 1st order mode.
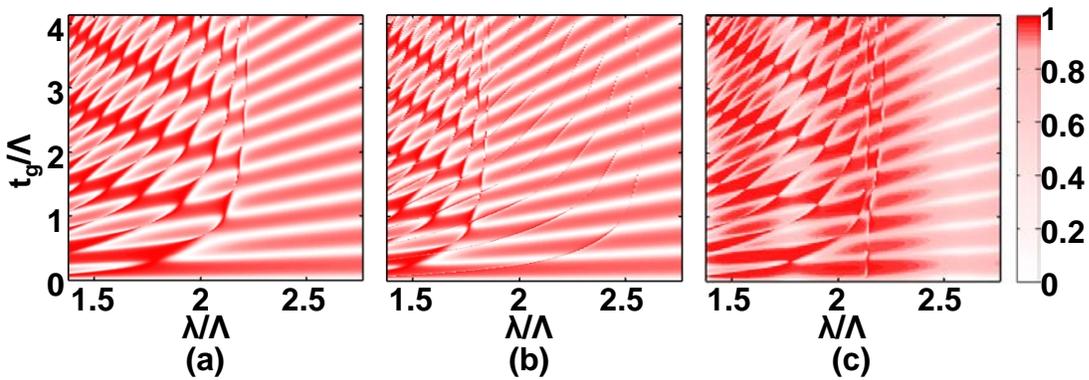
Figure 5.2 Reflection spectra from a single-layer high-index-contrast grating coupler. (a) Surface-normal incident light. (b) 10°-oblique incident light. (c) Surface-normal incident light with waveguide placed underneath the grating structure.

Now, we add the waveguide structure under the HCM. The structure geometries are as following. The HCM has duty cycle $\eta = 0.61$. The gap between the HCM and the waveguide is 320nm. The waveguide thickness is 100nm. The HCM is made of silicon with index $n_{bar} = 3.48$. The low index gap is assumed to be air. The diffraction spectrum is plotted in Figure 5.2(c) under the TE-polarized surface normal incidence. We notice that there exists an additional vertical line comparing with the plot in Figure 5.2(a). This vertical line is somewhat independent from t_g, locating at $\frac{\lambda}{\Lambda} = 2.13$. In the meanwhile, we notice that the effective index of the fundamental TE mode for the waveguide is also $n_{eff} = 2.13$. This vertical line is really created when the phase matching condition is satisfied, where $n_{eff} = \frac{\lambda}{\Lambda}$ with surface normal incidence.

As the resonance curves in the contour map reveal the dispersion of the resonance, we zoom into the region, where the vertical line crosses through the HCM resonance curve, as shown in Figure 5.3. Similar to other strong coupling phenomena, the dispersion curve of the HCM resonance and the waveguide eigen-mode repel each other at the cross and form the anti-crossing, which creates a forbidden zone in between the anti-crossing line. Strong coupling between the HCM and the

waveguide will be associated to this anti-crossing region. The coupling strength is monotonically related to the width of the forbidden zone.
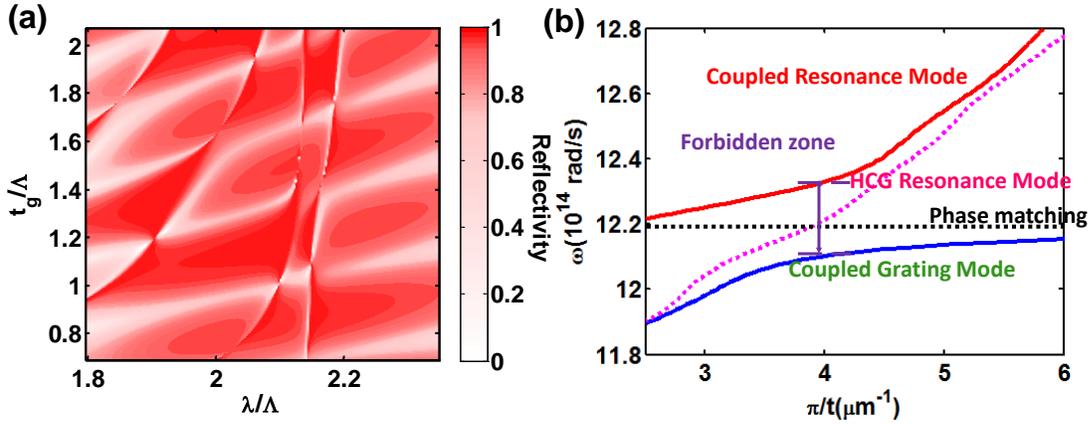
Figure 5.3 (a) The zoom-in plot for the contour map in the anti-crossing region for the HCM with waveguide underneath (b) The dispersion curve of the HCM resonance and the coupled waveguide mode converted from the reflection contour map.
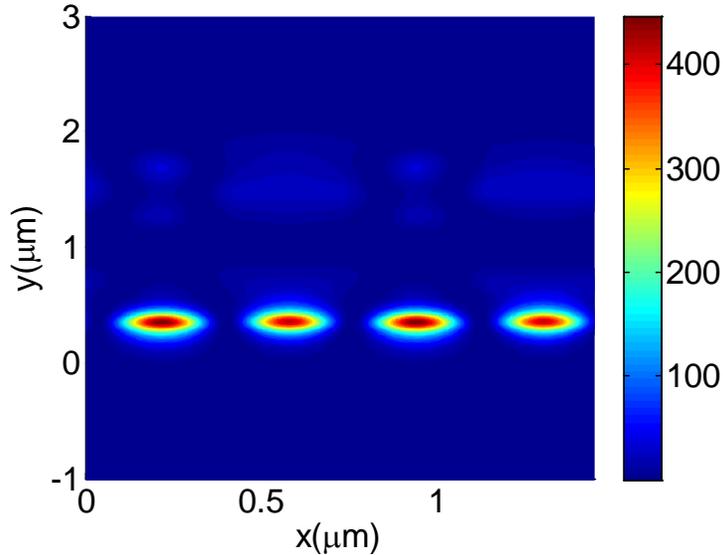
Figure 5.4 The field profile of the coupled HCM resonance.

The FDTD simulation is performed for the HCM design inside the forbidden zone. The HCM thickness is chosen to be 960 nm. The periodic boundary condition is applied to make the structure have infinite number of periods in the x-direction. The field inside the waveguide has been enhanced for more than 400 times. This resonance is very unique comparing with the conventional resonators. The HCM still serves as a resonator, however, the field is concentrated in a photonic

structure outside the resonator. Therefore, it is particularly interesting to use the HCM as the field concentrator for applications like solar cells.

5.2 HCM Vertical Optical Coupler

5.2.1 HCM Vertical Coupler Mechanism

Ultra-compact photonic integrated circuits (PICs) have the potential to replace conventional electronic integrated circuits and revolutionize a variety of technologies. Built from submicron-sized silicon photonic wires that carry light, PICs offer faster processing speed, a more compact size and the ability to integrate different optical functionalities onto a single chip. They are promising for applications ranging from light-based communication to interconnects to low-cost lab-on-a-chip systems[80, 81]. For practical purposes, it is important to be able to couple external light (from an optical fiber, free-space optics or device such as a laser) onto the chip efficiently and into on-chip waveguides for further use. However, single-mode silicon waveguides and external, out-of-plane light beams usually differ in size by two orders of magnitude. As a result, coupling efficiency is normally low and ultra-precise optical alignment of the components is necessary to achieve a level of useful coupling. This severely constrains the ability to test and package such systems, and therefore their practicality.

To date, efforts have been made to use inverse tapered waveguide to improve the coupling between on-chip waveguides and external light beams[82]; however there are a number of drawbacks with such approaches. Typically, specialized optical fibers and cleaved devices with polished facets are required. Very precise optical alignment and therefore custom device packaging is needed, which drastically increases the cost. Diffraction-grating-based light couplers have been studied extensively and are attractive because of their planar fabrication process and the ability to test their performance on the wafer-scale. However, while the optical coupling happens in the second-diffraction order, the principal diffraction order always exists and leads to light coupling with an efficiency that is decibels from unity [4-6]. Furthermore, this low coupling efficiency usually goes hand in hand with strong reflection to the incident light source, which poses an additional challenge given the difficulty of introducing an optical isolator into the compact integrated optical system.

We described in section Chapter 5, the HCM can be designed achieve strong coupling to the external waveguide. This effect can be used to enhance the vertical coupling efficiency. For the conventional second order grating coupler, light is coupled from the vertical incidence to the waveguide through 1st order diffraction. However, as the 0th order term A_0 always exists and has a real propagation component in the z-direction, the energy carried in this order is lost during the coupling. This "directionality problem" is a fundamental issue for grating-based waveguide couplers [83].

To solve this problem, one can set up an optical cavity in the z-direction in order to prevent the light from escaping in the 0th order before being coupled into the waveguide. Light is confined to the cavity and thus forced to undergo a much longer interaction with the coupler. Let us assume that light traverses the coupling cavity an average of N times before escaping. The enhanced coupling efficiency would then be $\gamma = 1 - (1 - \gamma_0)^N$, which exponentially approaches unity if N

is sufficiently large. This can be achieved by increasing the confinement of the light to the cavity. Previous work has proposed the use of a reflector below the waveguide structure to prevent 0th-order diffraction on the light transmission side[84]. However, from a practical standpoint it is not very convenient to place the other reflector at the incidence side ($z < 0$), as incoming light is usually delivered by an optical fiber, free-space optics or other light source. Thus setting up the resonance in the z-direction within the coupler itself is the ideal approach to suppressing the 0th-order diffraction and therefore maximizing light coupling efficiency.
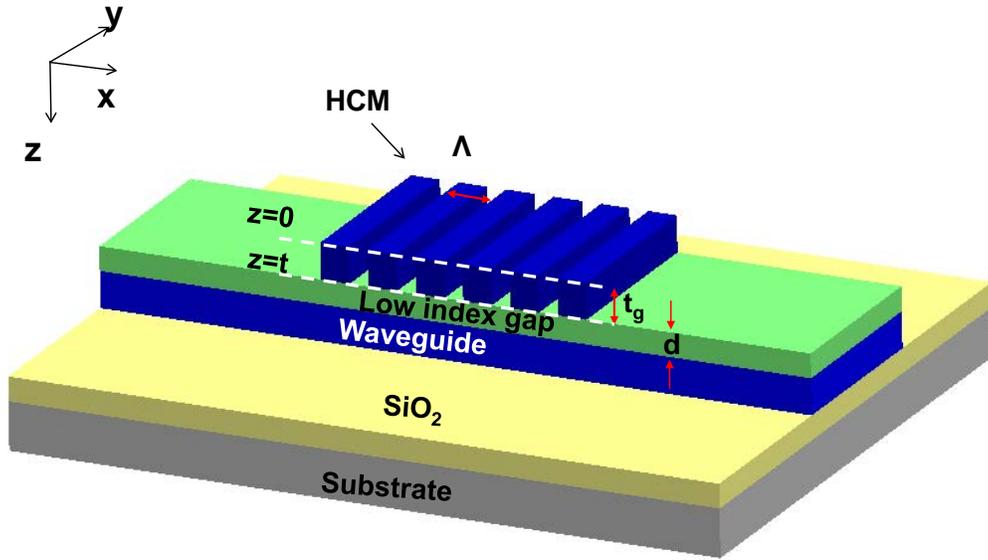
Figure 5.5 Schematic of the HCM vertical coupler. The HCM is sitting on top of the waveguide with a low index gap d.

The schematic of the proposed HCM vertical coupler is shown in Figure 5.5. The HCM is located on top of the waveguide with a low index gap. In the simulation, the gap is assumed to be air. However, SiO₂ can also be used to simplify the fabrication process. The HCM size is designed to match the mode spot of the incidence wave. For the input from the optical fiber, the HCM coupler can be designed as 10 µm by 10 µm. The light is first coupled into a wide waveguide, which can be modeled as a slab waveguide when the width is much larger than the optical wavelength. It can be adiabatically tapered down to the single mode waveguide after the vertical coupling.

5.2.2 FDTD Simulation Results

The FDTD simulation is performed to calculate the power being coupled to the waveguide. . In these simulations, the grating-based structure is made from silicon and the waveguide is made from silicon-on-insulator. The coupler is designed to couple incoming light of wavelength 1.55 µm. We use TE-mode light for the purposes of illustration, where the electrical field is along the y-direction. For light coupling from surface normal to in-plane, and a waveguide thickness of 100 nm, the period is 720 nm and duty cycle is 0.61. As plotted in Figure 5.6, the optical spectrum collected at the both end of the waveguide is plotted with the sweep of the HCM thickness. It replicates the coordinates in Figure 5.3. By overlapping the anti-crossing curves created by the

HCM resonance and waveguide eigen-mode, we find the strongest coupling happens at the anti-cross zone.
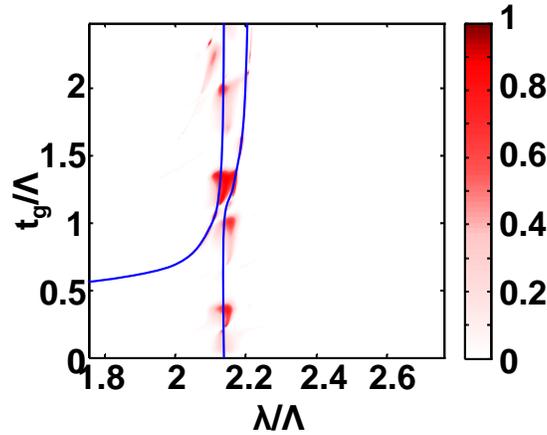
Figure 5.6 Coupling efficiency spectrum aligned with the anti-crossing.
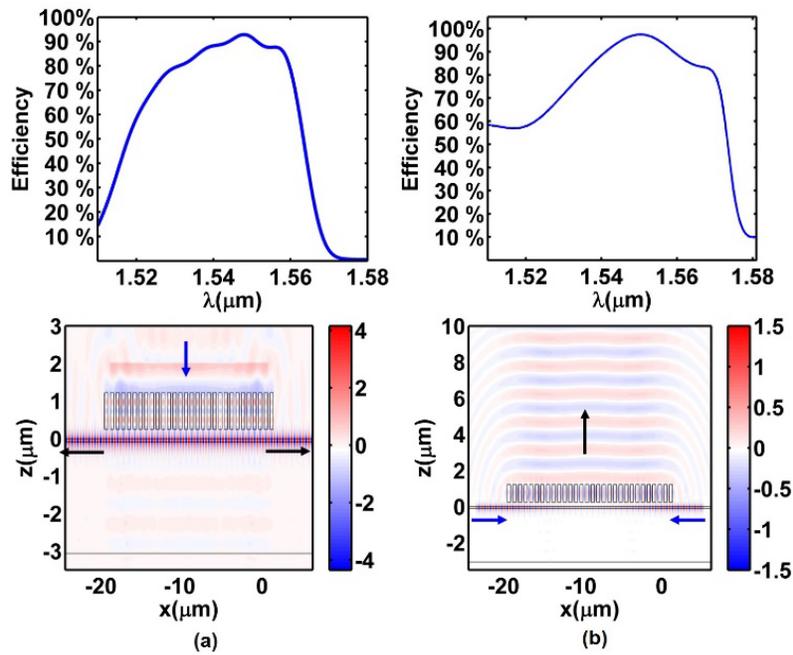
Figure 5.7 (a) Light coupling efficiency and field profile for surface-normal incoming light coupled to an in-plane waveguide. (b) Light coupling efficiency and field profile for surface-normal incoming light coupled to an in-plane waveguide, for symmetrical input.

At the optimized thickness $t_g = 963\ nm$, the maximal light coupling efficiency is 93%, with a bandwidth of 3dB (48 nm). The field profile and coupling efficiency spectrum are shown in Figure 5.7(a). For surface-normal incident light coupled into the waveguide, a small fraction of light in

the waveguide is seen to propagate out of the coupling region. The actual light coupling efficiency between the grating structure and waveguide is therefore slightly larger than the figure of 93% measured. To uncover this "true" efficiency value, two identical mode-matched light sources are inputted into the waveguide symmetrically and the light output in the vertical direction is measured. In this configuration, the peak efficiency is measured to be 98% with a 3-dB (70 nm) bandwidth, as shown in Figure 5.7(b).
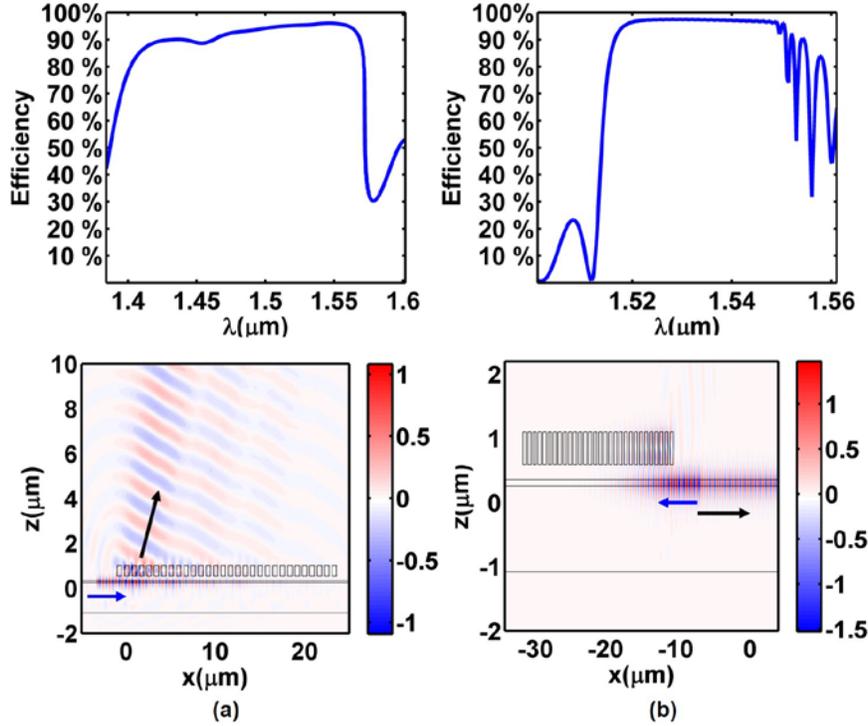
Figure 5.8 Field profile and port outputs for (a) light coupling from surface-normal to in-plane waveguide; (b) light coupling from in-plane waveguide to surface-normal, with symmetrical input. The blue arrow indicates input light; the black arrow indicates output.

For asymmetrical incidence, unlike the configuration shown in Figure 5.7(n) with two identical light source inputs, we use the input from one of the waveguide ports. In this case, the asymmetric resonant mode β_1 will be involved in the coupling mechanism. Based on the aforementioned anti-crossing design rule, we can also have strong coupling between the waveguide and the high-index-contrast grating structure. With this set-up, we can choose to couple the light in two ways: into out-of-plane space or back to the waveguide. For light coupled into out-of-plane space, the grating structure is designed with $\Lambda = 802\ nm$, $t_g = 443\ nm$ and $\eta = 0.61$. The simulated data are shown in Figure 5.8(a). In this case of asymmetrical incident light, the largest coupling efficiency that can be achieved is 96%, with an ultra-large bandwidth of 1 dB (170 nm). Note the output light amplitude decays along the x-direction in this structure. For the purposes of coupling to other optical components such as optical fibers, the high-index grating structure can be chirped to provide better mode matching[85]. For light coupled back to the waveguide, the grating structure

88

can serve as a reflector for light within the waveguide. For a grating structure with Λ = 724 nm, t = 495 nm and η = 0.61, incident light is reflected back (with the identical transverse mode) with 98% efficiency and a bandwidth of 1 dB (37 nm).

FDTD simulations are also performed to calculate the dimension tolerance of the vertical to in-plane coupler. As shown in Figure 5.9, the number of grating periods, HCM duty cycle (η), gap size (d) and HCM thickness (t) are swept. To keep the coupler has >80% efficiency, the thickness tolerance is larger than 100nm. However, the HCM needs around 50nm linewidth accuracy, making high resolution lithography demanded.
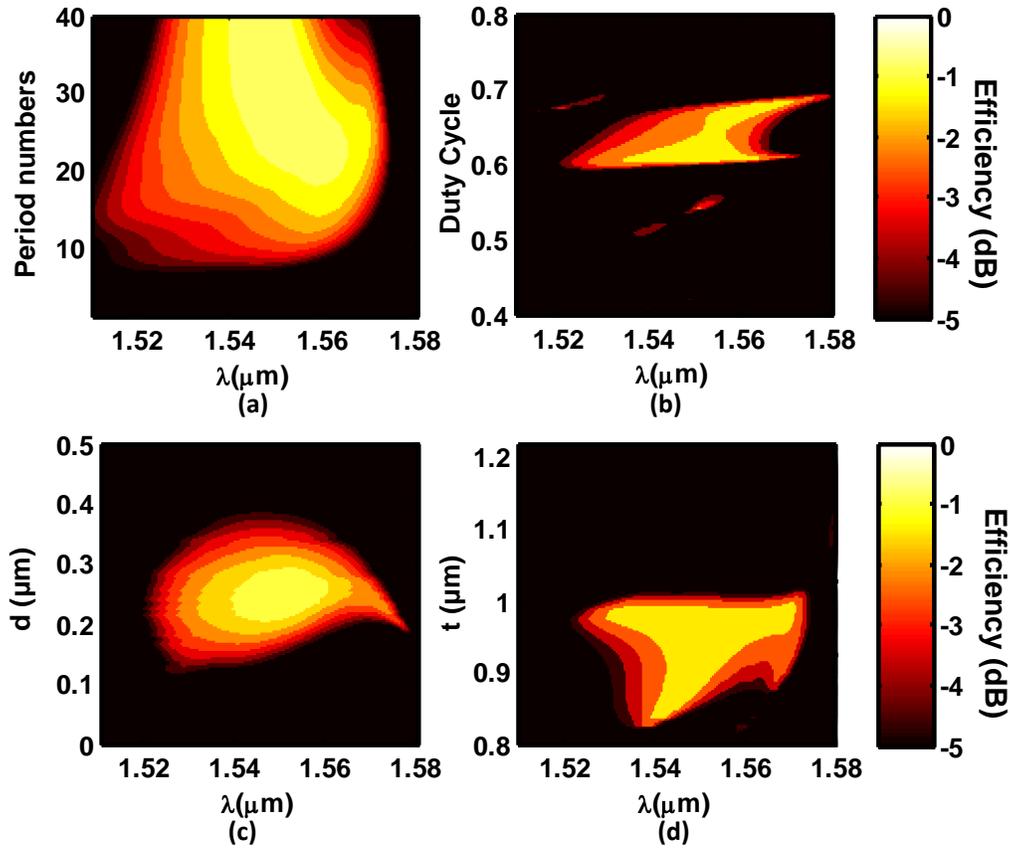
Figure 5.9 Coupler efficiency variation with different (a) Number of grating periods (b) Duty cycle (c) Gap size (d) Thickness
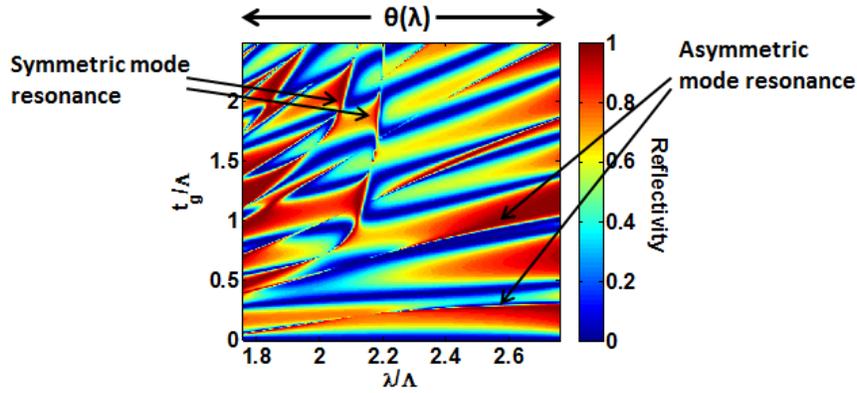
Figure 5.10 The reflection spectrum of single layer HCM with different tilted angle at different wavelength.

The coupling mechanism under the in-plane incidence can be analyzed as following. For the in-plane incidence case, if the light inputs are symmetrically from both waveguide port, it will be the reciprocal process of the surface normal to in-plane coupling; light can be coupled into vertical direction with the same mechanism. However, if input light is only coming from one waveguide port, the symmetry is broken. The asymmetrical mode is therefore introduced into this coupling process. In this case, the phase matching equation $n_0 \sin \theta_i + m \frac{\lambda}{\Lambda} = n_{eff}(\lambda)$ can be satisfied at different wavelength for different angle $\theta(\lambda)$. Here, $\theta(\lambda)$ is a function of wavelength as solved in the phase matching equation. That means the asymmetric mode can also be excited by the waveguide incidence light as it is excited by the plane wave with tilted angle $\theta(\lambda)$. The reflection spectrum of the infinite grating with different plane wave incidence angle $\theta(\lambda)$ at different wavelength is plotted in Figure 5.10. In this map, we can clearly distinguish the resonance of the symmetric and asymmetric modes.

At the center of one particular asymmetrical resonance, HCM acts as a resonant cavity in z direction that absorbs the light from the waveguide. However, the asymmetric mode can have propagation in x direction. Such propagation inside the periodical medium is essentially like a distributed Bragg reflector (DBR). Once the light is reflected back, it couples back to the waveguide reciprocally. With this mechanism, HCM is working as an external DBR mirror for the waveguide without doing damage to the waveguide. On the other hand, when both of the phase matching equation and HCM resonance condition is satisfied, the enhanced coupling between waveguide mode and HCM mode can happen. Because the HCM resonance at this case is Fano shape, it has to have strong output at the output plane towards vertical up direction at the wavelength very close to the resonance center. However, because the asymmetric mode has stronger coupling with the waveguide while the symmetric mode has stronger output at vertical direction, the highest coupling efficiency is expected to appear at the region where the symmetric and asymmetric modes have coupling with each other. Under such condition, light will be coupled into HCM efficiently through the asymmetric mode and coupled out into vertical direction through the symmetric mode with the internal mode coupling of HCM.

90
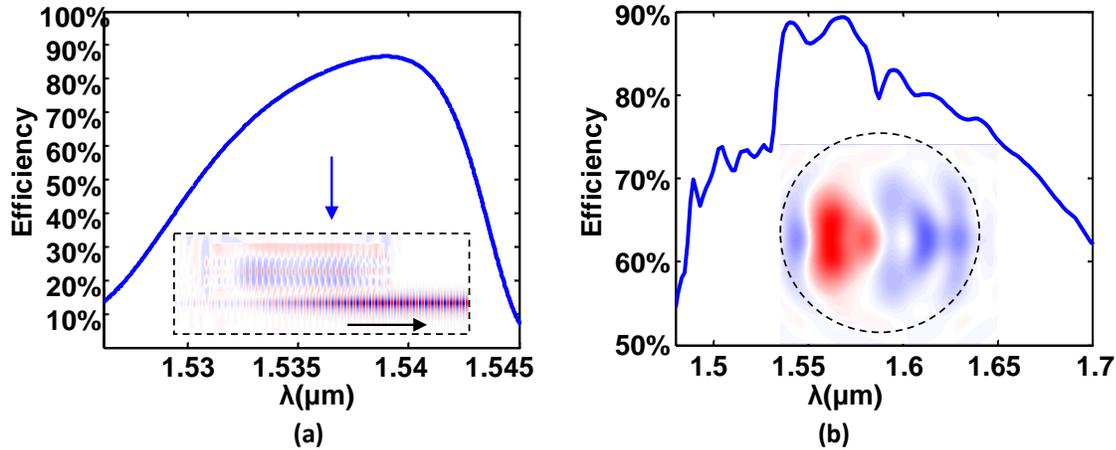
Figure 5.11 Efficiency and field profiles for different coupler configurations. (a) For coupling of light from the surface-normal to a selected direction; (b) Efficiency and near-field output pattern for the curved coupler.

The results shown in Figure 5.7 and Figure 5.8 demonstrate the basic functionality of our light coupling approach – efficient on-chip light coupling and reflection. These functionalities can be combined in interesting and practically useful ways.

One such example is the combination of a coupler with a waveguide reflector, which enables incoming light to be coupled into a preferred direction. The schematic of such a set-up is shown in Figure 5.11(a). A waveguide reflector, which is designed to have the same thickness as the grating coupler, is placed at the forbidden output for one waveguide direction. By optimizing the distance between the reflector and coupler, our FDTD simulations show that incoming light can be directed (coupled) from the surface-normal to a specific in-plane output direction with an efficiency of 88%. A natural application of this set-up is to integrate a multi-wavelength VCSEL array onto a PIC for the purposes of on-chip wavelength-division multiplexing.

Another example involves using a circular outline coupler to fit the mode profile of a curved optical fiber as a way of minimizing waveguide taper length from the narrow waveguide to the light-coupling region. Due to the compactness of PICs, single-mode silicon photonic wires are usually very narrow (500 nm in diameter). However, because the input light aperture is much larger (for the purposes of reducing light losses) – typically around 10 μm for optical fiber, for example – the adiabatic transition taper angle is very small (approximately 1º). This means that the tapered waveguide has to be hundreds of microns in length, which is impractical for use in PICs. Adopting a focusing coupler configuration[86], in which the coupler is curved to focus the wave front inside the taper region, enables a larger taper angle to be used, which translates to low loss. The schematic of the structure is shown in Figure 5.12. By choosing the grating coupler to have a circular profile, the coupler can be made to match the optical fiber. With such a design, an 89% coupling efficiency is achieved with a 26º taper angle. The near-field output profile of the coupler is shown in Figure 5.11(b) (blue curve). This configuration enables the use of a tapered waveguide that is ten times shorter.
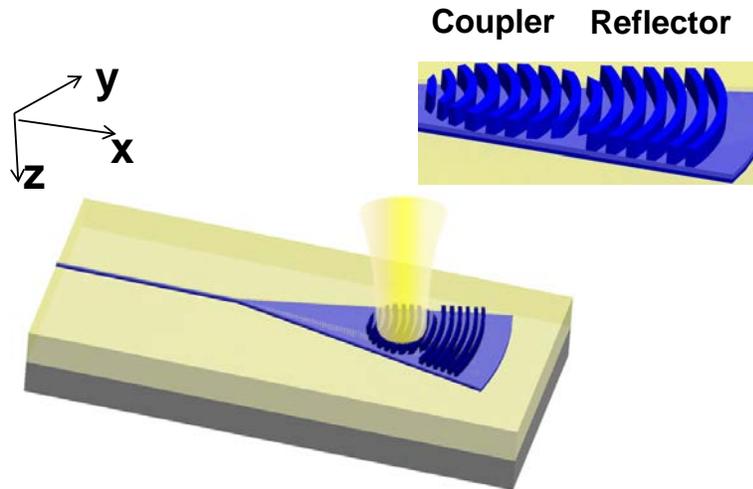
Figure 5.12 Schematic of the focusing HCM grating coupler.

5.2.3 HCM Vertical Coupler Fabrication and Characterization

The HCM vertical coupler is fabricated with the following process. The process starts with an SOI wafer and the silicon waveguide is patterned by UV lithography followed with dry etching. Next, the low index gap (SiO_2) is deposited by LPCVD. The surface of the SiO_2 is smoothen by CMP (chemical mechanical polishing). The deposition of the poly silicon for the HCM layer is performed followed up with another CMP step. Finally, the HCM is patterned by UV lithography on the poly silicon layer. The schematic of the structure is shown in Figure 5.13(a) and the 3-dimensional microscopic image of the HCM vertical coupler is taken by the confocal microscope.
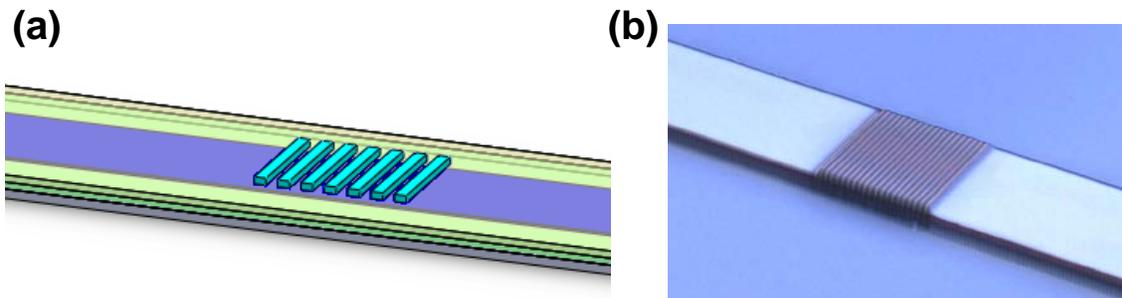
Figure 5.13 (a) Schematic (b) Microscopic photograph of the HCM vertical coupler

The measurement setups are shown in Figure 5.14(a) and (b). The waveguide loss is first calibrated by the straight waveguide without the HCM vertical coupler on the top. The light is coupled with the end-fire method. The vertical coupler efficiency is measured with the incidence light from the optical fiber in the vertical direction and the output light is coupled into another cleaved fiber. The measurement shows -1 dB (80%) coupling efficiency with 39 nm 3 dB bandwidth, from 1516 nm to 1565 nm.
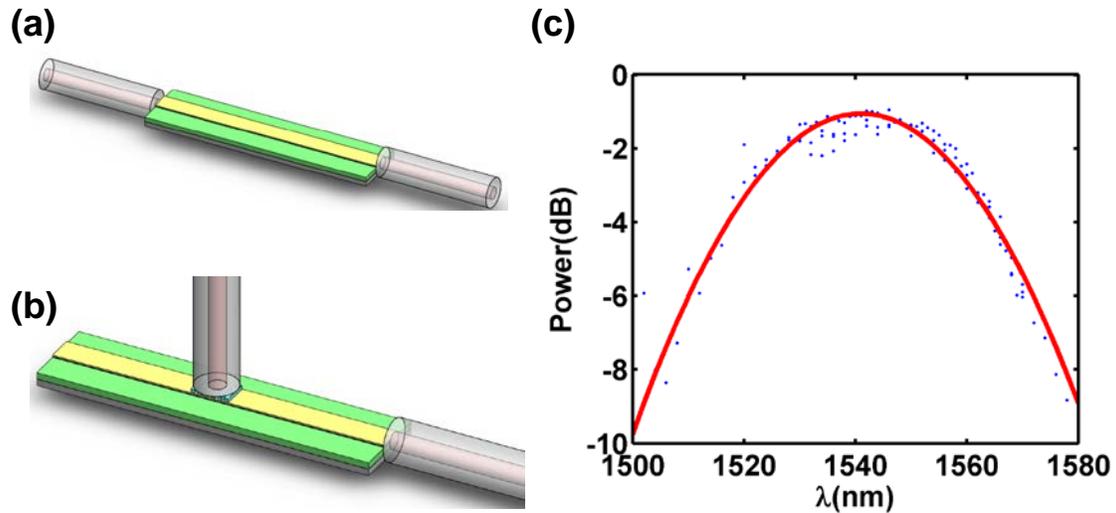
Figure 5.14 (a) Measurement setup schematic for waveguide loss calibration (b) Setup schematic for coupler efficiency measurement. (c) Measurement result for the HCM vertical coupler.

5.3 HCM Multiplexer

5.3.1 HCM Multiplexer Introduction

The growing need of input-output (IO) bandwidth in the network systems, such as high performance computers and data centers, is stimulating the development of the optical interconnects. Starting from 2005, when the first optical link was implemented in the super computer, the number of the optical links being utilized in one high performance computing system has been grown for more than 1000 times over the past seven years, from thousands to millions [77]. As of such dramatically fast growth trend, reducing the physical volume of the data links and the cost on fibers are important considerations for the future network systems. The wavelength division multiplexing (WDM) technology has been rapidly developed and widely deployed in optical communication systems. WDM system enables multiple channel data transmission in a single fiber-optic link and can dramatically increase the aggregate data rate [87]. On the other hand, the tunable VCSEL array [28] provides the possibility to do chip level integration between active multi-wavelength laser source and photonic integrated circuits and reduce the cost of the WDM optical links.

However, the wavelength of the conventional grating based multiplexer (MUX), such as array waveguide grating multiplexer (AWG MUX), is fixed as discrete grids. It limits the use of the tunable laser source, which desires the continuous wavelength multiplexing. Also, based on the diffraction nature of the grating, the wavelength channels have to follow a spatial sequence. It restricts the routing on the photonic chip especially when the photonic circuit has high complexity. In addition, the silica-based MUX/DeMUX has dimensions on the centimeter scale, leading to huge size mismatch with the photonic chips and limiting the WDM applications in computer-com applications. The insertion loss of the AWG MUX is typically more than 3 dB. It gives penalty to

93

utilizing WDM in optical interconnects with the tight link budget. Therefore, it is desirable to have the WDM multiplexer without wavelength grid and sequence restrictions in micron scale footprint to maximize its flexibility and configurability with the tunable lasers and photonic integrated circuits (PICs).

In order to realize the optical functions in micro scale or even nano scale, the high contrast metastructures (HCM) are investigated. HCM is a periodical or nearly-periodic structure with key dimensions smaller than the optical wavelength. The refractive index contrast between the high index and low index materials results in various functions to manipulate the magnitude, phase and propagation direction of optical beams. It is been described in section 5.2 that the HCM can be designed as a very efficiency vertical optical coupler. The coupling efficiency approaching unity is achieved with the bandwidth large enough to cover the C-band for optical communication.

5.3.2 HCM Multiplexer Design

(a) (b)
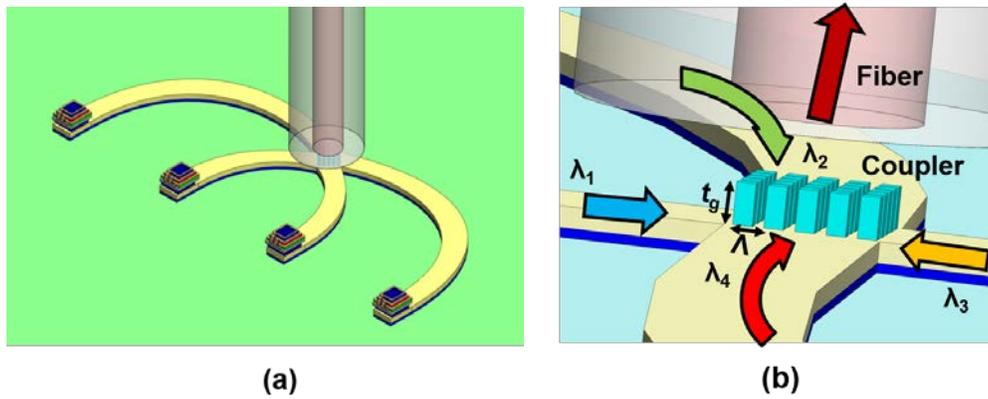
Figure 5.15 (a) Overview of the WDM configuration. Light from the different channels is routed to the cross junction and multiplexed into the fiber at the surface normal direction (b) Zoom in view of the HCM-MUX. The HCM is located upon the junction region with a low index gap to the waveguide. Light from all the channels are coupled into the vertical direction to fiber or other optics.

Here we propose an ultra-small MUX structure leveraging HCMs to enable the multiplexing and coupling of channels at different wavelength on PIC chip to a single optical fiber. Such structure reduces the MUX size to 10 micro meter scale and keeps the high coupling efficiency between on-chip waveguides and fibers and high isolation between different channels. Because the light coupling between one specific channel and the surface normal direction has no dependence on the optical structures of other channels, the proposed MUX can work at any wavelength within the high efficiency coupling band. Since there is no wavelength sequence/position requirement for the input channels, this MUX is uniquely well suited for combining a tunable laser array. This is a function that is being sought after but could not be achieved with traditional grating-based WDM MUX.

The schematic of the high contrast metastructure multiplexer (HCM-MUX) is shown in Figure 5.15. Figure 5.15(a) shows the integration schematic between of the tunable VCSEL array with

94

the PIC. Light from VCSEL is coupled into the on-chip photonic wires by the vertical couplers. The incidence light at different wavelength channel within C-band is routed in the on-chip photonic wires, such as silicon waveguides. To have further functionalities, each channel can have complex on chip optical blocks, which are not shown in this schematic. At MUX region, four channels are merged at the cross junction, as shown in Figure 5.15(b). The high contrast metastructure (HCM) is located upon the junction region with a low index gap. The HCM could be made by silicon or other high index materials. The low index gap could be simply air or filled by SiO_2. There are three parameters to control the characteristics of the HCM: thickness (t_g), period (Λ) and duty cycle (η). For the two dimensional HCM, the period and duty cycle can vary in the two horizontal directions.

The MUX is designed as the following strategy. In order the couple the light into the surface normal direction, the period of the HCM has to match the periodicity of the guided light in the propagation direction. Aiming at the center wavelength λ_0, the guided light wave period in the waveguide is $\frac{\lambda_0}{n_{eff}(\lambda_0)}$, where $\boldsymbol{n_{eff}(\lambda_0)} n_{eff}(\lambda_0)$ is the effective index of the waveguide for wavelength $\boldsymbol{\lambda_0} \lambda_0$. Because all waveguides for different wavelength channels are in the same device layer, the waveguides have the same thickness. The waveguide width at the MUX region has to be around 10μm wide in order to have enough number of HCM periods for coupling, making the HCM-MUX have a footprint of $\boldsymbol{10\mu m \times 10\mu m}$. Therefore, for the wide waveguides, the effective index of the wavelength within C-band is very close ($\boldsymbol{n_{eff}(\lambda) \cong n_{eff}(\lambda_0)}$). Thus, the HCM can be designed to have the same period at both x and y direction for same polarization, which is $\boldsymbol{\Lambda = \frac{\lambda_0}{n_{eff}(\lambda_0)}}$. The strong coupling phenomenon between the in-plane waveguide and surface normal direction is based on the resonance characteristics of HCM. The duty cycle and thickness of HCM is designed to provide optical resonance in z direction. The low index gap is necessary to assure the HCM is fully surrounded by the low index medium and therefore making the resonance to build up at both interface. Due to this low index gap, HCM is located at the evanescence field of the transverse waveguide mode. Therefore, there is an optimum value for the low index gap. It needs to be large enough to guarantee the resonance of HCM; on the other hand, excessive thick low index gap will make the guided transverse mode too small at HCM and consequently make coupling difficult. Typically, the low index gap is around 200 nm for silicon waveguide. At a small range around the optimum thickness, the gap could be a parameter to tune the coupling bandwidth. With the enhancement effect by HCM resonance, light could be coupled into the surface normal direction with very high efficiency.
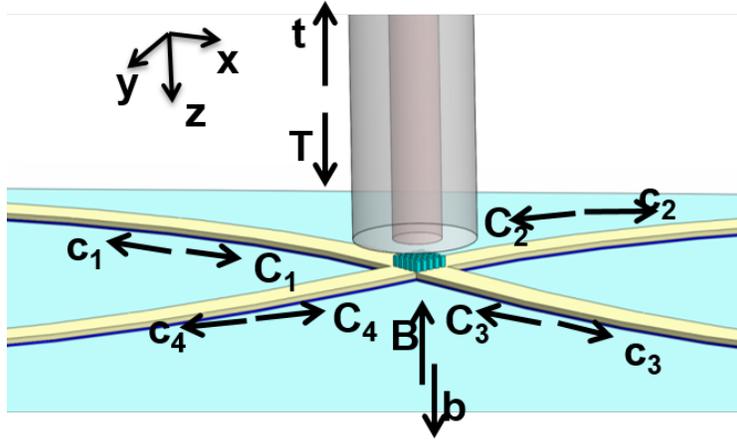
Figure 5.16 Scattering matrix model of the multiplexer. The waveguide channels are defined as port C1 to C4. The fiber output is defined as channel T and the light scattering to the substrate is defined as port B.

The multiplexer with four waveguide channels and the fiber output can be quantified by the scattering matrix. The waveguide channels are defined as port C1 to C4. The fiber output is defined as port T. To make the analysis comprehensive, the light scattering to the substrate is defined as port B. The ports are labeled in figure 2. For multiplexing, the incidence light is coming from the waveguide ports. Therefore, the incidence from fiber and substrate can be designated as 0. Therefore, scattering matrix of this device can be simplified from a 6×6 matrix to a 6×4 matrix, as shown in equation (1). Because the HCM is designed to be symmetric at both x and y direction, the waveguide ports C1 to C4 are rotational symmetric. Such symmetry greatly reduces the complexity of the scattering matrix. By knowing the output from the incidence of one single waveguide channel, which are $S_{ij}, i = 1, 2, 3, 4, t, b$, all of the matrix element can be derived by the rotating the index.

$$\begin{bmatrix} c_1 \\ c_2 \\ c_3 \\ c_4 \\ t \\ b \end{bmatrix} = \begin{bmatrix} S_{11} & S_{12} & S_{13} & S_{14} \\ S_{21} & S_{22} & S_{23} & S_{24} \\ S_{31} & S_{32} & S_{33} & S_{34} \\ S_{41} & S_{42} & S_{43} & S_{44} \\ S_{t1} & S_{t2} & S_{t3} & S_{t4} \\ S_{b1} & S_{b2} & S_{b3} & S_{b4} \end{bmatrix} \begin{bmatrix} C_1 \\ C_2 \\ C_3 \\ C_4 \end{bmatrix}$$

5.1

5.3.3 FDTD Simulation Results

Based on this strategy, the first step is to design the HCM to have high efficiency coupling from one waveguide port into the fiber using the aforementioned method. For the silicon waveguide with 100 nm thickness, the period of HCM is designed as 865nm with a duty cycle of 0.61. The low index gap is 220 nm. FDTD simulation is performed to calculate the matrix elements S_{i1}. The

simulation model is shown in Figure 5.17(a). A broad band light inputs from waveguide port C1. The output of all ports are monitored. The result is shown in Figure 5.17(b). S_{t1}, which stands for the light coupling efficiency from the waveguide to the optical fiber, has the peak value of 90% with 35nm 1dB bandwidth. It makes the device sufficient to cover the entire C-band for WDM application. On the other hand, the isolation between different waveguide ports are also desired to give the lowest impact on the optical functionalities before multiplexing. S_{11} and S_{31} are the reflection from port C1 and light transmission from port C3 passing through the HCM structure. In most of the wavelength bandwidth, they are suppressed below -10dB. S_{21} and S_{41} are the light coupling from the perpendicular waveguide. They are suppressed below -25dB. The scattering into the substrate is typically below -10dB. By having those matrix elements, the entire scattering matrix is known with the rotational symmetry.

(a)   (b)
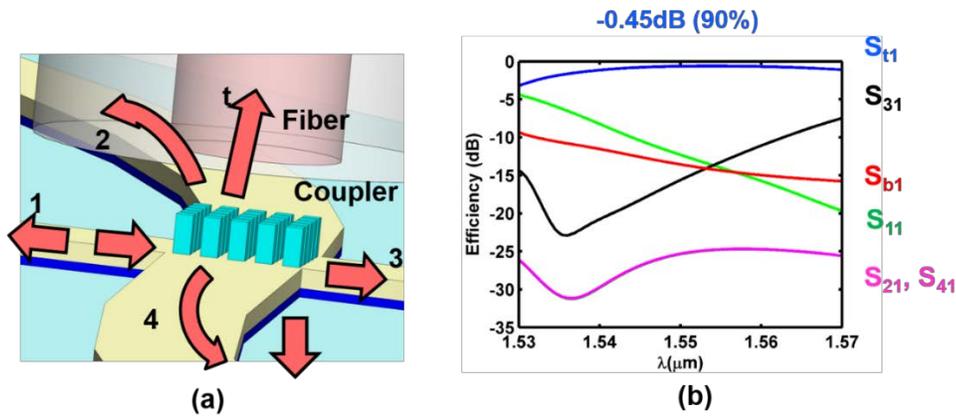
Figure 5.17 (a) Simulation model of the waveguide to fiber coupling with input from channel 1. (b) Simulation result for the matrix elements with the working wavelength bandwidth.

(a)   (b)
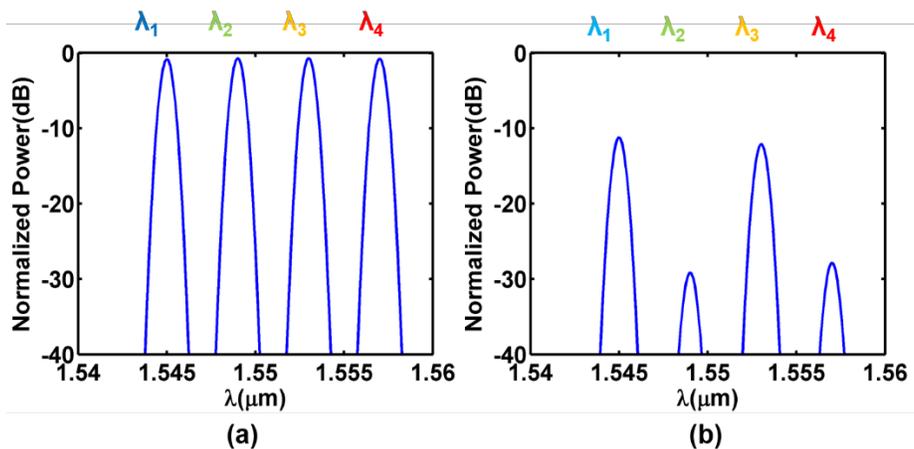
Figure 5.18 (a) Optical spectrum of the output from the optical fiber (b) Optical spectrum of the output from the waveguide channel C1.

97

The next step is to verify the multiplexing of the device. Here the model shown in Figure 5.15(b) is used. In the simulation, four narrow linewidth light sources with different wavelength are placed as the waveguide inputs. The wavelength spacing is 4nm and the linewidth is 0.7nm. The source power at the peak of the spectrum is normalized to unity. Figure 5.18(a) shows the spectrum of the fiber output. The insertion loss of the multiplexing is -0.5dB. Because of the broad bandwidth of the coupling, the spectrum shape from all wavelength channels are well maintained. Figure 5.18(b) shows the output from waveguide port C1, which indicates the isolation between different channels. The returning light is below -10dB. Light transmission from port C3 is also below -10dB. The light coupling from port C2 and C4 are suppressed below -30dB.
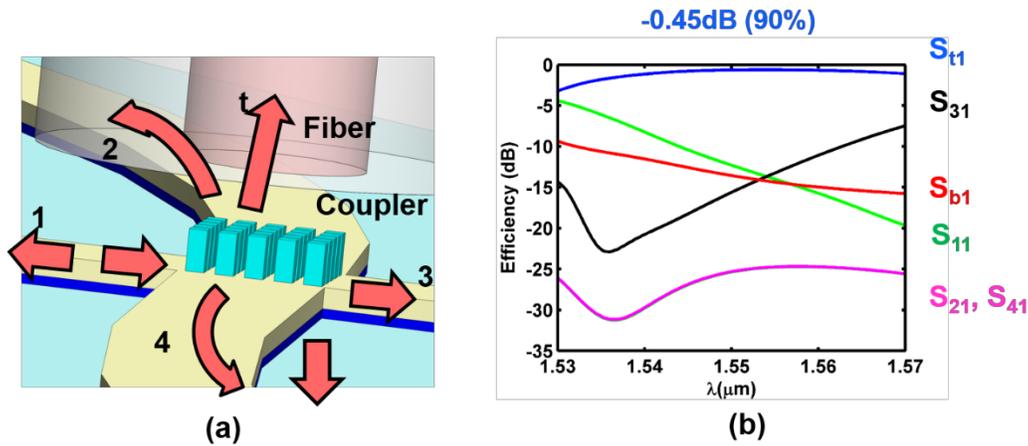
Figure 5.19 (a) Simulation model of the waveguide to fiber coupling with input from channel 1. (b) Simulation result for the matrix elements with the working wavelength bandwidth.

To verify this multiplexer does not have the wavelength sequence dependence, the wavelength sequence at the waveguide ports in the previous simulations are randomized. As shown in Figure 5.19(a), the wavelength of the channels in the previous configuration are switched randomly. Simulation result shown in Figure 5.19(b) confirms that the multiplexer have the identical output as the previous configuration shown in Figure 5.18(a).

5.4 HCM Photonic Switch

As the tremendous growth of the bandwidth and computing hungry applications, such as video streaming, cloud computing, internet commerce, etc, the network bandwidth requirement for the data centers and super computers is rising exponentially. The optical interconnections started to be implemented in such systems from last decade and have managed to replace the traditional electrical cables. The realization of all the network functions on the photonic integrated circuits is ideal to make the optical network to be compact and energy efficient.

The active light switching between the photonic wires on the photonic integrated circuits is very important to enable complex functions on chip. The waveguide directional coupler or ring

resonators can enable efficient light coupling between the photonic wires. However, such coupling requires very large device volume and the tuning by applying the thermo-optic or electro-optic method on the large coupling area consumes significant amount of power. The grating coupler can enable such coupling within very short propagation distance. However, the coupling wavelength characteristics of the conventional grating couplers are determined by the grating geometry, leading to the difficulty of being actively tuned in integrated photonic circuits. Here we propose to use the resonance property of the HCM as the refractive index sensitive coupler to design the optical switch as compact as $0.7\lambda^3$.
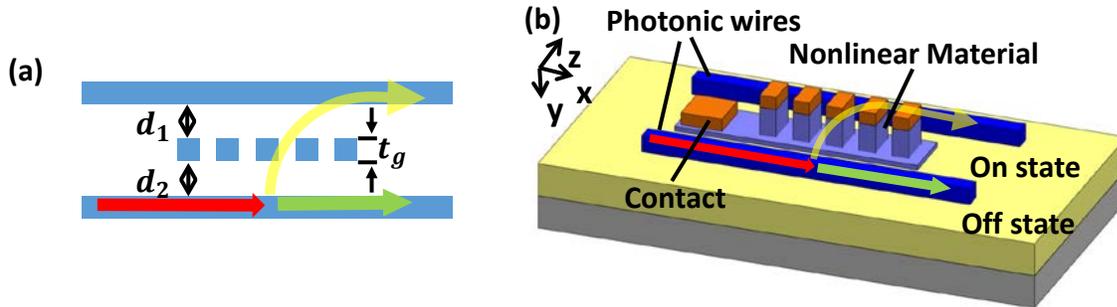
Figure 5.20 (b) Top view and (c) three dimensional schematics of the photonic wire switch structure. The photonic wires are labeled as WG1 and WG2. The HCM may or may not have the same thickness as the photonic wires as labeled in y direction in (c).

It has been demonstrated that the resonance property of HCM can be used to strongly enhance the coupling efficiency between the lightwave with different propagation constant. Because the HCM resonance wavelength has strong refractive index dependence, tuning the grating refractive index shifts the coupling in the spectrum. The grating coupler in that structure is locating apart from the waveguide. Adjusting the gap d between the waveguide and grating can tune the coupling bandwidth without affecting the peak coupling efficiency in a certain range. Such property is ideal to be used for the on-chip light switch with compact footprint and leading to low energy cost.

Our proposed switch structure is shown in Figure 5.20. Two parallel photonic wires are located with HCM at the center. The HCM dimension in y direction is the grating bar length while z dimension is the grating thickness t_g. The photonic wires are usually the silicon waveguide in silicon photonics. The HCM can be made of silicon such that the switch can be fabricated monolithically. Other materials with larger non-linear coefficient, such as InGaAsP, can also be utilized to achieve larger energy efficiency. The signal light at wavelength λ_0 is coming from one waveguide as presented as the red arrow in the schematic. By tuning the refractive index of the grating coupler, the coupling between the photonic wires could be enabled or disabled, which is corresponding to on or off state, shown as the yellow or green arrow in the schematic figure. At off state, light coupling is disabled. The signal light propagates through the photonic wire straightly. At on state, light coupling is enabled. At such condition, signal light is coupled into the other photonic wire. Based on such mechanism, the output of the signal light is switched between different photonic wires actively.
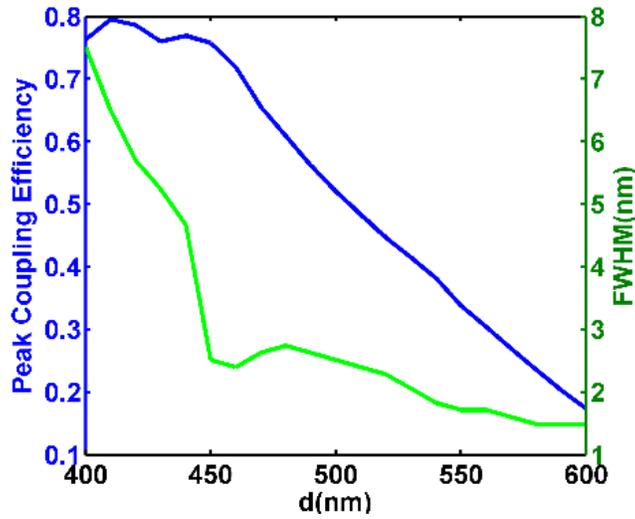
Figure 5.21 The coupling space gap d dependence of the peak coupling efficiency and the FWHM of the HCM photonic wire switch.

A sample design is simulated by the finite difference time domain (FDTD) method. As designed for monolithic silicon photonics, the waveguide and HCM are both designed to have 1μm thickness in y direction. The HCM has period $\Lambda = 850nm$, duty cycle $\eta = 0.61$ and thickness $t_g = 1\mu m$. Figure 5.21 Shows the dependence of the peak coupling efficiency and the full width half maximum (FWHM) to the distance d between the HCM and the waveguide. Between $d = 400nm$ to $d = 460nm$, while the coupling efficiency is relatively flat, the FWHM drops significantly from 8nm to 2.3nm. In order to have efficient switching, keeping the coupling bandwidth broad enough to cover the signal bandwidth, narrower FWHM is desired. Thus, the waveguide is designed to be 460nm away from HCM.
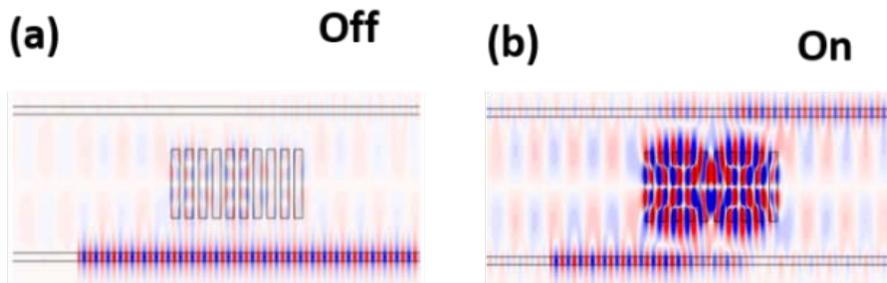
Figure 5.22 The optical field profile of the switch working at (a) on status (b) off status.

At off status, because the coupling is disabled, light passes through the input waveguide, as plotted in Figure 5.22(a). At on status, the coupling efficiency reaches 70% with the optical field plotted in Figure 5.22(b). In the meanwhile, the output of the WG1 drops down to only 6%. By changing the HCM refractive indices, the coupling wavelength shifts accordingly. From to the simulation

result shown in Figure 5.23, the refractive index change of 0.005 can already shift the coupling wavelength for 2nm and provide larger than 15dB on/off extinction ratio for WG1 and larger than 5dB on/off extinction ratio for WG2. Biasing more index tuning can provide larger extinction ratio while the energy efficiency is sacrificed.
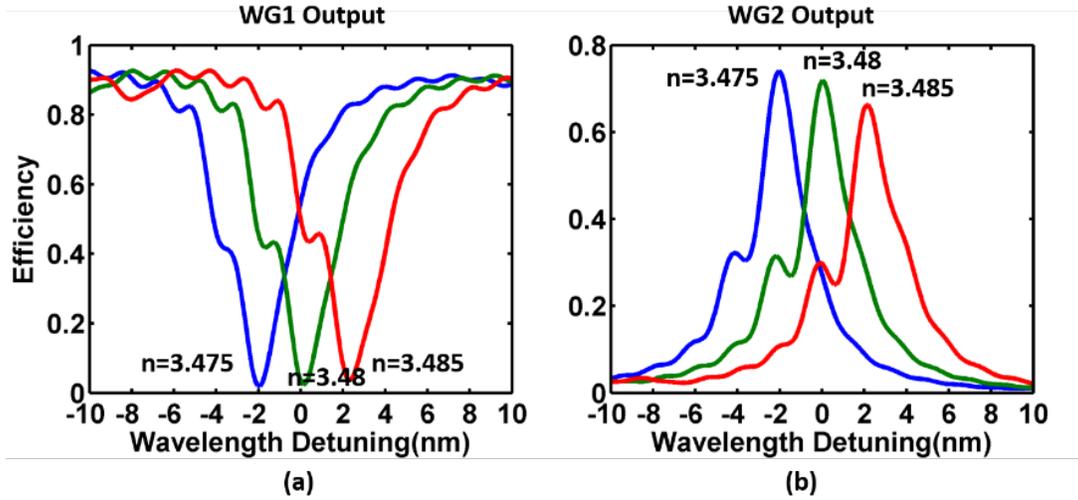
Figure 5.23 The output spectrum from (a) waveguide 1 (b) waveguide 2 with varied HCM refractive indices.

Due to the high index contrast and strong optical confinement, the HCM size is only $1.4\lambda^3$ in volume. Such compact size provides the capacitance as small as 2fF, which is more than 20 times smaller than the ring resonators [88]. With using the large non-linearity material like InGaAsP with the free-carrier plasma effect, the switching energy per bit can be calculated by $E_b = \frac{1}{a^2}\left(\frac{n^2 q^2 d^2}{4\varepsilon}\right)\left(\frac{V_m}{Q^2}\right)$, estimated to be 0.5fJ/bit.

5.5 Summary

In summary, we have demonstrated that it is possible to couple light very strongly from a high-refractive-index-contrast subwavelength grating structure to a submicron waveguide, as is typically used in an optical integrated circuit set-up. Coupling efficiencies of 93% are attainable. This represents an improvement in coupling efficiency of 73% relative to existing approaches, and offers a simpler design that lends itself to integration with PICs. The enhanced light coupling arises as a result of the Fabry-Perot resonance of light inside the cavity provided by the grating structure. The grating structure can be designed to act as a coupler between on-chip light and off-chip light or as a reflector for light within a waveguide. By combining these two functionalities, more advanced optical devices can be conceived. For example, a single-layer grating structure could be used as the basis for an on-chip, in-plane cavity surface emitting laser, without the need for any etching of the active material. This approach could lead to advanced photonic integrated circuits where light coupling is no longer an issue.

With adding the second dimensional periodicity to the HCM vertical coupler, this device can be used as the multiplexer to combine the signals from multiple waveguide input into one single optical fiber. The simulation results shows the 90% efficiency for four channels multiplexing with square lattice structure HCM. The isolation between the channels are better than 10 dB. In principle, with applying more complex lattice structures, more channels can be accommodated. This MUX has continuous multiplexing wavelength without wavelength sequence requirement. It is ideal to work with the tunable laser arrays and complex photonic circuits to enable high bandwidth density optical interconnects with low cost and high flexibility.

The HCM coupler can also be used to couple the light between two waveguides. The coupling efficiency strongly relies on the resonance of the HCM. When the HCM is in resonance, the coupling efficiency can be turned on to 70% while the power in the original waveguide drops down to 5%. The resonance can be switched by tuning the refractive index of the HCM, achieved by the carrier injection. The simulation predicts that only 0.005 refractive index shift is required to shift the resonance wavelength for 2nm, giving 15 dB extinction ratio. Such a compact integrated photonic switch only has $1.4\lambda^3$ in volume, leading to ultra-low power consumption, estimated as 0.5fJ/bit.

Chapter 6

Conclusion

In this dissertation, we explore the physics of the HCM in the near wavelength regime and apply its unique optical phenomena for the novel devices toward flexible photonic integration. The HCM in the subwavelength regime has been well-understood through the extensive study in the past decade. However, the regime that allows two diffraction orders also has rich properties and has been overlooked by the previous research works. We realize that HCM is capable to be designed to enhance or cancel any of the diffraction order in this regime with very large tolerance. This effect equivalently create an anomalous reflection or refection at the diffraction interface, which is not only very interesting as a completely new optical phenomenon, but also very valuable for broadband color splitting applications.

The anomalous diffraction effect is used to make the first artificial chameleon skin. We developed and optimized the transfer printing method to fabricate the HCM with sub-micron feature size in the flexible membrane with extremely high uniformity. Bad-pixel-free display samples are demonstrated with 40,000 pixels. The HCM helps to achieve extremely high optical efficiency, up to 83%, for the color tuning. In addition, the color of the HCM is tuned from green to orange through the flexible membrane deformation. This unique material is further exploited for display and camouflage applications, demonstrating its capability to hide the image to the background with proper tuning. The future direction of this work is to incorporate the electroactive polymer to achieve active tuning of each individual HCM pixels through applying voltage. Additionally, multiple layers of the HCM structure can be stacked, mimicking photonic structure of the real chameleon skin to achieve the wider color tuning with broad view angle range.

We also utilize the ultra-thin HCM reflector to achieve the first flexible VCSEL operating at the silicon transparent wavelength. With replace the bottom DBR reflector by the HCM, the thermal conductance is significantly improved. The flip-chip bonding process is developed to facilitate the process at both sides of the InP epitaxial layer. This device is package inside the PDMS substrate and achieved lasing with electrical injection. Moreover, the metal heat spreading layer is applied to further improve the heat extraction. Those dedicated optimizations for the thermal conductance make the flexible VCSEL achieve continuous operation at up to 35°C ambient temperature with above 0.5 mW light output.

In addition to the unique mirrorless resonance property, the HCM can be placed very close to an external photonic structure to achieve strong optical coupling. This property is particularly useful for the light coupling for the photonic circuits, for instance, the coupling between the VCSELs and the silicon photonics waveguides. The simulation results show 93% coupling efficiency, largely exceed the result from other reports. A two-dimensional HCM vertical couple can be configured as a multiplexer to combine the signal from multiple waveguide inputs into an optical fiber. The device foot print is only 10 µm by 10 µm, significantly smaller than the array waveguide gratings (AWG). The continuous multiplexing spectrum also reduces the system complexity and make the

tunable VCSEL applicable in the WDM scheme. This HCM couple can also be configured as the photonic switch to control the light path between two adjacent waveguides. The coupling is enabled by the HCM resonance that can be tuned by its refractive shift through current injection. Sub-fJ per bit switching is possible attributing to its compact size.

In conclusion, the presented HCM devices build up a platform to realize the flexible photonic integrated circuits (PIC) with efficient light emitting and controlling, as well as low loss input/output interface. It provides a solid foundation to realize the flexible PIC systems for the emerging wearable application.

References

[1]   M. Goodwin, "TOWARDS 2020–PHOTONICS DRIVING ECONOMIC GROWTH IN EUROPE," *Brussels: European Technology Platform Photonics21,* 2013.

[2]   D. Po, L. Xiang, S. Chandrasekhar, L. L. Buhl, R. Aroca, and C. Young-Kai, "Monolithic Silicon Photonic Integrated Circuits for Compact 100+Gb/s Coherent Optical Receivers and Transmitters," *IEEE Journal of Selected Topics in Quantum Electronics,* vol. 20, pp. 150-157, 2014.

[3]   C. Monat, P. Domachuk, and B. J. Eggleton, "Integrated optofluidics: A new river of light," *Nature Photonics,* vol. 1, pp. 106-114, 2007.

[4]   J. Carolan, C. Harrold, C. Sparrow, E. Martin-Lopez, N. J. Russell, J. W. Silverstone*, et al.*, "Universal linear optics," *Science,* vol. 349, pp. 711-6, Aug 14 2015.

[5]   (2015, 11 Nov). *Projected global photonics market size from 2005 to 2020*. Available: http://www.statista.com/statistics/282346/global-photonics-market-size/

[6]   (2015, 11 Nov). *Breakdown of the global photonics market in 2011 and 2020*. Available: http://www.statista.com/statistics/282352/breakdown-of-the-global-photonics-market-by-segment/

[7]   K. Nomura, H. Ohta, A. Takagi, T. Kamiya, M. Hirano, and H. Hosono, "Room-temperature fabrication of transparent flexible thin-film transistors using amorphous oxide semiconductors," *Nature,* vol. 432, pp. 488-92, Nov 25 2004.

[8]   K. Müllen and U. Scherf, *Organic light emitting devices: synthesis, properties and applications*: John Wiley & Sons, 2006.

[9]   A. Sugimoto, H. Ochi, S. Fujimura, A. Yoshida, T. Miyadera, and M. Tsuchida, "Flexible OLED Displays Using Plastic Substrates," *IEEE Journal of Selected Topics in Quantum Electronics,* vol. 10, pp. 107-114, 2004.

[10]   G. Li, R. Zhu, and Y. Yang, "Polymer solar cells," *Nature Photonics,* vol. 6, pp. 153-161, 2012.

[11]   M. M. Tavakoli, K. H. Tsui, Q. Zhang, J. He, Y. Yao, D. Li*, et al.*, "Highly Efficient Flexible Perovskite Solar Cells with Antireflection and Self-Cleaning Nanostructures," *ACS Nano,* vol. 9, pp. 10287-95, Oct 27 2015.

[12]   F. Hao, C. C. Stoumpos, D. H. Cao, R. P. H. Chang, and M. G. Kanatzidis, "Lead-free solid-state organic–inorganic halide perovskite solar cells," *Nature Photonics,* vol. 8, pp. 489-494, 2014.

[13]   D. Liu and T. L. Kelly, "Perovskite solar cells with a planar heterojunction structure prepared using room-temperature solution processing techniques," *Nature Photonics,* vol. 8, pp. 133-138, 2013.

[14]   M. A. Meitl, Z.-T. Zhu, V. Kumar, K. J. Lee, X. Feng, Y. Y. Huang*, et al.*, "Transfer printing by kinetic control of adhesion to an elastomeric stamp," *Nature Materials,* vol. 5, pp. 33-38, 2005.

[15]   J. Yoon, S.-M. Lee, D. Kang, M. A. Meitl, C. A. Bower, and J. A. Rogers, "Heterogeneously Integrated Optoelectronic Devices Enabled by Micro-Transfer Printing," *Advanced Optical Materials,* vol. 3, pp. 1313-1335, 2015.

[16]   D. Kang, S.-M. Lee, Z. Li, A. Seyedi, J. O'Brien, J. Xiao*, et al.*, "Compliant, Heterogeneously Integrated GaAs Micro-VCSELs towards Wearable and Implantable Integrated Optoelectronics Platforms," *Advanced Optical Materials,* vol. 2, pp. 373-381, 2014.

[17]   E. Bosman, J. Missinne, B. V. Hoe, G. V. Steenberge, S. Kalathimekkad, J. V. Erps*, et al.*, "Ultrathin Optoelectronic Device Packaging in Flexible Carriers," *IEEE Journal of Selected Topics in Quantum Electronics,* vol. 17, pp. 617-628, 2011.

[18]   Y. Chen, H. Li, and M. Li, "Flexible and tunable silicon photonic circuits on plastic substrates," *Sci Rep,* vol. 2, p. 622, 2012.

[19]   A. Karim, S. Bjorlin, J. Piprek, and J. E. Bowers, "Long-wavelength vertical-cavity lasers and amplifiers," *IEEE Journal of Selected Topics in Quantum Electronics,* vol. 6, pp. 1244-1253, 2000.

[20]   C. J. Chang-Hasnain and W. Yang, "High-contrast gratings for integrated optoelectronics," *Advances in Optics and Photonics,* vol. 4, p. 379, 2012.

[21]   C. F. R. Mateus, M. C. Y. Huang, Y. F. Deng, A. R. Neureuther, and C. J. Chang-Hasnain, "Ultrabroadband mirror using low-index cladded subwavelength grating," *Ieee Photonics Technology Letters,* vol. 16, pp. 518-520, Feb 2004.

[22]   M. C. Y. Huang, Y. Zhou, and C. J. Chang-Hasnain, "A surface-emitting laser incorporating a high-index-contrast subwavelength grating," *Nature Photonics,* vol. 1, pp. 119-122, 2007.

[23]   M. C. Y. Huang, Y. Zhou, and C. J. Chang-Hasnain, "A nanoelectromechanical tunable laser," *Nature Photonics,* vol. 2, pp. 180-184, 2008.

[24]   I. I. S. Chung, J. Mork, P. Gilet, and A. Chelnokov, "Subwavelength Grating-Mirror VCSEL With a Thin Oxide Gap," *IEEE Photonics Technology Letters,* vol. 20, pp. 105-107, 2008.

[25]   C. Chase, Y. Zhou, and C. J. Chang-Hasnain, "Size effect of high contrast gratings in VCSELs," *Opt Express,* vol. 17, pp. 24002-7, Dec 21 2009.

[26]   Y. Rao, "InP-based Long Wavelength VCSEL using High Contrast Grating," Ph.D, EECS, University of California, Berkeley, 2012.

[27]   T. Ansbaek, I.-S. Chung, E. S. Semenova, and K. Yvind, "1060-nm Tunable Monolithic High Index Contrast Subwavelength Grating VCSEL," *IEEE Photonics Technology Letters,* vol. 25, pp. 365-367, 2013.

[28]   Y. Rao, W. Yang, C. Chase, M. C. Huang, D. Worland, S. Khaleghi*, et al.*, "Long-wavelength VCSEL using high-contrast grating," *Selected Topics in Quantum Electronics, IEEE Journal of,* vol. 19, pp. 1701311-1701311, 2013.

[29]   B. W. Yoo, M. Megens, T. Chan, T. Sun, W. Yang, C. J. Chang-Hasnain*, et al.*, "Optical phased array using high contrast gratings for two dimensional beamforming and beamsteering," *Opt Express,* vol. 21, pp. 12238-48, May 20 2013.

[30]   B. W. Yoo, M. Megens, T. Sun, W. Yang, C. J. Chang-Hasnain, D. A. Horsley*, et al.*, "A 32 x 32 optical phased array using polysilicon sub-wavelength high-contrast-grating mirrors," *Opt Express,* vol. 22, pp. 19029-39, Aug 11 2014.

[31]   M. M. Ye Zhou, J. Kern, M. C. Y. Huang, and C. J. Chang-Hasnain, "Surface-normal emission of a high-Q resonator using a subwavelength high-contrast grating," *Optics Expresss,* vol. 16, 2008.

[32]   T.-T. Wu, S.-H. Wu, T.-C. Lu, and S.-C. Wang, "GaN-based high contrast grating surface-emitting lasers," *Applied Physics Letters,* vol. 102, p. 081111, 2013.

[33]   T. Sun, S. Kan, G. Marriott, and C. J. Chang-Hansnain, "High Contrast Grating Resonator for Label-Free Biosensor," p. STu4K.6, 2015.

[34]   F. Lu, F. G. Sedgwick, V. Karagodsky, C. Chase, and C. J. Chang-Hasnain, "Planar high-numerical-aperture low-loss focusing reflectors and lenses using subwavelength high contrast gratings," *Optics Expresss,* vol. 18, 2010.

[35]   D. Fattal, J. Li, Z. Peng, M. Fiorentino, and R. G. Beausoleil, "Flat dielectric grating reflectors with focusing abilities," *Nature Photonics,* vol. 4, pp. 466-470, 2010.

[36]   P. Qiao, L. Zhu, and C. J. Chang-Hansnain, "Design Rule of 2D High Contrast Gratings and Engineering of Orbital Angular Momentum of Light," in *CLEO: Science and Innovations*, 2015, p. SW1I. 5.

[37]   N. Yu and F. Capasso, "Flat optics with designer metasurfaces," *Nat Mater,* vol. 13, pp. 139-50, Feb 2014.

[38]   F. G. S. Vadim Karagodsky, and Connie J. Chang-Hasnain, "Theoretical analysis of subwavelength high contrast grating reflectors," *Optics Expresss,* vol. 18, 2010.

[39]   C. C. Vadim Karagodsky, and Connie J. Chang-Hasnain, "Matrix Fabry Perot resonance mechanism in high-contrast gratings," *Optics Letters,* vol. 36, 2011.

[40]   V. K. a. C. J. Chang-Hasnain, "Physics of near-wavelength high contrast gratings," *Optics Expresss,* vol. 20.

[41]   C. Weisbuch, M. Nishioka, A. Ishikawa, and Y. Arakawa, "Observation of the coupled exciton-photon mode splitting in a semiconductor quantum microcavity," *Phys Rev Lett,* vol. 69, pp. 3314-3317, Dec 7 1992.

[42]   J. P. Reithmaier, G. Sek, A. Loffler, C. Hofmann, S. Kuhn, S. Reitzenstein*, et al.*, "Strong coupling in a single quantum dot-semiconductor microcavity system," *Nature,* vol. 432, pp. 197-200, Nov 11 2004.

[43]   J. D. Joannopoulos, S. G. Johnson, J. N. Winn, and R. D. Meade, *Photonic crystals: molding the flow of light*: Princeton university press, 2011.

[44]   W. Yang, J. Ferrara, K. Grutter, A. Yeh, C. Chase, Y. Yue*, et al.*, "Low loss hollow-core waveguide on a silicon substrate," *Nanophotonics,* vol. 1, 2012.

[45]   Y. Zhou, M. Moewe, J. Kern, M. C. Huang, and C. J. Chang-Hasnain, "A Novel High-Q Resonator Using High Contrast Subwavelength Grating," in *Conference on Lasers and Electro-Optics/Quantum Electronics and Laser Science Conference and Photonic Applications Systems Technologies*, San Jose, California, 2008, p. CThT5.

[46]   K. S. Kunz and R. J. Luebbers, *The finite difference time domain method for electromagnetics*: CRC press, 1993.

[47]   N. Yu, P. Genevet, M. A. Kats, F. Aieta, J. P. Tetienne, F. Capasso*, et al.*, "Light propagation with phase discontinuities: generalized laws of reflection and refraction," *Science,* vol. 334, pp. 333-7, Oct 21 2011.

[48]   E. G. Loewen and E. Popov, *Diffraction gratings and applications*: CRC Press, 1997.

[49]   S. Fan, W. Suh, and J. D. Joannopoulos, "Temporal coupled-mode theory for the Fano resonance in optical resonators," *J. Opt. Soc. Am. A,* vol. 30, 2003.

[50]   H. A. Macleod, *Thin-film optical filters*: CRC Press, 2010.

[51]   M. Kolle, B. Zheng, N. Gibbons, J. J. Baumberg, and U. Steiner, "Stretch-tuneable dielectric mirrors and optical microcavities," *Opt Express,* vol. 18, pp. 4356-64, Mar 1 2010.

[52]   S. Bertani, B. Jacobsson, F. Laurell, V. Pasiskevicius, and M. Stjernstrom, "Stretching-tunable external-cavity laser locked by an elastic silicone grating," *Opt Express,* vol. 14, pp. 11982-6, Dec 11 2006.

[53]   M. Aschwanden and A. Stemmer, "Polymeric, electrically tunable diffraction grating based on artificial muscles," *Opt Lett,* vol. 31, pp. 2610-2, Sep 1 2006.

[54]   K. Suzumori, M. Mihara, and S. Wakimoto, "Beautiful Flexible Microactuator Changing its Structural Color with Variable Pitch Grating," *2011 Ieee International Conference on Robotics and Automation (Icra),* 2011.

[55]   H. Fudouzi and T. Sawada, "Photonic rubber sheets with tunable color by elastic deformation," *Langmuir,* vol. 22, pp. 1365-8, Jan 31 2006.

[56]   Z. H. Fang, C. Punckt, E. Y. Leung, H. C. Schniepp, and I. A. Aksay, "Tuning of structural color using a dielectric actuator and multifunctional compliant electrodes," *Applied Optics,* vol. 49, pp. 6689-6696, Dec 10 2010.

[57]   C. E. Finlayson and J. J. Baumberg, "Polymer opals as novel photonic materials," *Polymer International,* vol. 62, pp. 1403-1407, 2013.

[58]   E. D. Palik, *Handbook of optical constants of solids* vol. 3: Academic press, 1998.

[59]   M. Moharam and T. Gaylord, "Rigorous coupled-wave analysis of planar-grating diffraction," *JOSA,* vol. 71, pp. 811-818, 1981.

[60]   J. S. Toll, "Causality and the Dispersion Relation: Logical Foundations," *Physical Review,* vol. 104, pp. 1760-1770, 12/15/ 1956.

[61]   Z. Wang, "Polydimethylsiloxane mechanical properties measured by macroscopic compression and nanoindentation techniques," 2011.

[62]   A. L. Thangawng, R. S. Ruoff, M. A. Swartz, and M. R. Glucksberg, "An ultra-thin PDMS membrane as a bio/micro-nano interface: fabrication and characterization," *Biomed Microdevices,* vol. 9, pp. 587-95, Aug 2007.

[63]   F.-T. An, K. S. Kim, Y.-L. Hsueh, M. Rogge, W.-T. Shaw, and L. Kazovsky, "Evolution, challenges and enabling technologies for future WDM-based optical access networks," in *2nd Symposium on Photonics, Networking, and Computing, Cary, North Carolina*, 2003, pp. 26-30.

[64]   K. Prince, M. Ma, T. B. Gibbon, and I. Tafur Monroy, "Demonstration of 10.7-Gb/s transmission in 50-km PON with uncooled free-running 1550-nm VCSEL," in *Conference on Lasers and Electro-Optics: Applications*, 2010, p. ATuA2.

[65]   W. H. Hofmann, P. Moser, P. Wolf, A. Mutig, M. Kroh, and D. Bimberg, "44 Gb/s VCSEL for optical interconnects," in *Optical Fiber Communication Conference*, 2011, p. PDPC5.

[66]   D. Vez, S. Eitel, S. G. Hunziker, G. Knight, M. Moser, R. Hoevel*, et al.*, "10 Gbit/s VCSELs for datacom: devices and applications," in *Photonics Fabrication Europe*, 2003, pp. 29-43.

[67]   E. Wong, X. Zhao, C. J. Chang-Hasnain, W. Hofmann, and M. C. Amann, "Optically injection-locked 1.55-m VCSELs as upstream transmitters in WDM-PONs," *Photonics Technology Letters, IEEE,* vol. 18, pp. 2371-2373, 2006.

[68]   D. V. Plant, M. B. Venditti, E. Laprise, J. Faucher, K. Razavi, A. G. Kirk*, et al.*, "256-channel bidirectional optical interconnect using VCSELs and photodiodes on CMOS," *Journal of Lightwave Technology,* vol. 19, p. 1093, 2001.

[69]   T. Sakamoto, H. Tsuda, M. Hikita, T. Kagawa, K. Tateno, and C. Amano, "Optical interconnection using VCSELs and polymeric waveguide circuits," *Journal of lightwave technology,* vol. 18, p. 1487, 2000.

[70]   G. Roelkens, L. Liu, D. Liang, R. Jones, A. Fang, B. Koch*, et al.*, "III-V/silicon photonics for on-chip and intra-chip optical interconnects," *Laser & Photonics Reviews,* vol. 4, pp. 751-779, 2010.

[71]   S.-R. Mun, J.-H. Moon, S.-M. Oh, and C.-H. Lee, "A self wavelength tracking method for a cost effective WDM-PON with tunable lasers," in *Optical Fiber Communication Conference*, 2010, p. OWG7.

[72]   Y. R. Christopher Chase, Werner Hofmann, and Connie J. Chang-Hasnain, "1550 nm high contrast grating VCSEL," *Optics Expresss,* vol. 18, 2010.

[73]   S. Goeman, S. Boons, B. Dhoedt, K. Vandeputte, K. Caekebeke, P. V. Daele*, et al.*, "First Demonstration of Highly Reflective and Highly Polarization Selective Diffraction Gratings (GIRO-Gratings) for Long-Wavelength VCSEL's," *IEEE PHOTONICS TECHNOLOGY LETTERS,* vol. 10, 1998.

[74]   F. Brückner, D. Friedrich, T. Clausnitzer, M. Britzger, O. Burmeister, K. Danzmann*, et al.*, "Realization of a Monolithic High-Reflectivity Cavity Mirror from a Single Silicon Crystal," *Physical Review Letters,* vol. 104, 2010.

[75] C. J. Chang-Hasnain, J. P. Harbison, G. Hasnain, A. C. V. Lehmen, L. T. Florez, and N. G. Stoffel, "Dynamic, Polarization, and Transverse Mode Characteristics of Vertical Cavity Surface Emitting Lasers," *IEEE JOURNAL OF QUANTUM ELECTRONICS,* vol. 27, 1991.

[76] J. H. Marsh, "Quantum well intermixing," *Semiconductor science and technology,* vol. 8, p. 1136, 1993.

[77] M. A. Taubenblatt, "Optical interconnects for high-performance computing," *Journal of Lightwave Technology,* vol. 30, pp. 448-457, 2012.

[78] D. A. B. Miller, "Optical interconnects to silicon," *IEEE Journal of Selected Topics in Quantum Electronics,* vol. 6, pp. 1312-1317, 2000.

[79] D. Liang and J. E. Bowers, "Recent progress in lasers on silicon," *Nature Photonics,* vol. 4, pp. 511-517, 2010.

[80] D. A. Miller, "Optical interconnects to silicon," *Selected Topics in Quantum Electronics, IEEE Journal of,* vol. 6, pp. 1312-1317, 2000.

[81] R. Soref, "The past, present, and future of silicon photonics," *Selected Topics in Quantum Electronics, IEEE Journal of,* vol. 12, pp. 1678-1687, 2006.

[82] V. R. Almeida, R. R. Panepucci, and M. Lipson, "Nanotaper for compact mode conversion," *Optics Letters,* vol. 28, pp. 1302 - 1304, 2003.

[83] G. Roelkens, D. Van Thourhout, and R. Baets, "High efficiency Silicon-on-Insulator grating coupler based on a poly-Silicon overlay," *Optics Express,* vol. 14, p. 11622, 2006.

[84] F. Van Laere, G. Roelkens, M. Ayre, J. Schrauwen, D. Taillaert, D. Van Thourhout*, et al.*, "Compact and Highly Efficient Grating Couplers Between Optical Fiber and Nanophotonic Waveguides," *Lightwave Technology, Journal of,* vol. 25, pp. 151 - 156, 2007.

[85] X. Chen, C. Li, C. K. Y. Fung, S. M. G. Lo, and H. K. Tsang, "Apodized Waveguide Grating Couplers for Efficient Coupling to Optical Fibers," *Photonics Technology Letters, IEEE,* vol. 22, pp. 1156 - 1158, 2010.

[86] F. Van Laere, T. Claes, J. Schrauwen, S. Scheerlinck, W. Bogaerts, D. Taillaert*, et al.*, "Compact Focusing Grating Couplers for Silicon-on-Insulator Integrated Circuits," *Photonics Technology Letters, IEEE,* vol. 19, pp. 1919 - 1921, 2007.

[87] Q. Fang, T.-Y. Liow, J. F. Song, K. W. Ang, M. B. Yu, G. Q. Lo*, et al.*, "WDM multi-channel silicon photonic receiver with 320 Gbps data transmission capability," *Optics express,* vol. 18, pp. 5106-5113, 2010.

[88] P. Dong, S. Liao, D. Feng, H. Liang, D. Zheng, R. Shafiiha*, et al.*, "Low V pp, ultralow-energy, compact, high-speed silicon electro-optic modulator," *Optics Express,* vol. 17, pp. 22484-22490, 2009.